Investigations of Cooperative Interactions in Template Induced Crystallization Processes and Kinetic Studies of Nucleation and Growth by Small-Angle Neutron Scattering

Dissertation
zur
Erlangung des Grades

„ Doktor der Naturwissenschaften ”
am Fachbereich Chemie und Pharmazie
der Johannes Gutenberg – Universität in Mainz

Mathias Balz
geboren in Mainz

Mainz 2004

Die vorliegende Arbeit wurde in der Zeit von Dezember 2000 bis Juni 2004 am Institut für Anorganische und Analytische Chemie der Johannes Gutenberg – Universität in Mainz angefertigt.

Tag der mündlichen Prüfung: 15.07.2004

Table of Contents

1. Introduction

Biomineralization is the process of formation of inorganic solid materials by living organisms. The formation of mineralized skeleton structures by living organisms started about 570 million years ago [1]. Living organisms are able to produce high-quality mineral structures ranging from the Ångstrom to the centimeter level and built at ambient temperature and pressure. Corals, crawfish, mussels and snails create highly complex and extremely stable inorganic materials of partly intriguing shape that show a vast variety of biological functions as well as remarkable, unusual and advantageous mechanical properties. Key components in the process of formation are biological macromolecules, which are intimately associated with the inorganic minerals leading to so-called biocomposites. These macromolecules exert control on nucleation, growth, crystal shape, particle size, polymorphic structure and crystal orientation resulting in physical properties of the biominerals that are very different compared to those of their synthetic counterparts [2]. The fact that the mineralization process involves a cellular process and also that the formation of the organic matrix is genetically controlled, makes it difficult to probe and mimic these complex systems. Therefore it is not surprising that the process of biomineralization so far is not well understood in detail [2]. Nevertheless it is possible to study the biological and chemical aspects by model systems. In particular, the use of the organic components that mediate the growth of the mineral, the nucleation process as well as the structure-property-function relations are of special interest for materials scientists and engineers. Understanding these processes could enable researchers to imitate the often advantageous properties of the biominerals and to develop new ideas for the improved design of synthetic materials.

With the above-named aspects in mind the DFG (Deutsche Forschungsgemeinschaft) has launched a research project [3] which involves scientific research groups from biology, biochemistry, inorganic and analytical chemistry.

More than 60 different biominerals are known. These include both crystalline and amorphous materials. The most widespread examples are iron oxide, silica, calcium phosphate and calcium carbonate [1].

The different types of iron oxides display several varying functions depending on the living organism. For example, there are molluscs called chitons (polyplacophora) [4-6] which involve about 1000 species. One feature is their multi-part shell, another is their impressive mouth, which contains teeth made of magnetite or other crystalline iron oxides. The chitons are found on intertidal rocks or under rocks of reefs. They feed on algae, scraping them off rocks and coral reefs. For this purpose their teeth have to be very tough and hard. The mineralization process of the teeth is very complex and involves other minerals such as calcium phosphate and an organic matrix. The process of fabrication of this high-grade material by a rather primitive mollusc group is not yet understood. Disclosing this secret could enable scientists to mimick these processes and manufacture high-grade synthetic magnetite.

Many different animal species, such as pigeons or specific fish species, use the earth`s magnetic field to orient themselves. In many cases the underlying sensor is not well known, however it is identified in the so-called magnetotactic bacteria [7-9], that are able to orientate along geomagnetic field lines. The magnetic bacteria are to be found at the sediment-water interface both in salt water and fresh water. Their internal compass needle is made of nano-sized magnetite crystalls that are aligned to form a chain. The formation of this magnetic structure, the so called magnetosomes, is achieved by a biomineralization process, which takes place in membrane vesicles. In this process the characteristic size and morphology of the magnetosomes is controlled.

Diatoms [10] are unicellular organisms that are able to create unique and complex structures from amorphous silica. Their shell serves as a protection shield to prevent these organisms from being eaten by small crawfish. The mechanism of formation of this amorphous material is different compared to that of crystalline material. The material is pressed into a “mould”, wherein the condensation of $Si(OH)_4$ takes place.

Also the radiolarians [4] are single-celled organisms that are famous for their ability to build complex and beautiful micro-exoskeletons of silica (Figure 1.1). Some of them have spines to increase their surface area. Thus they have an improved ability to float.

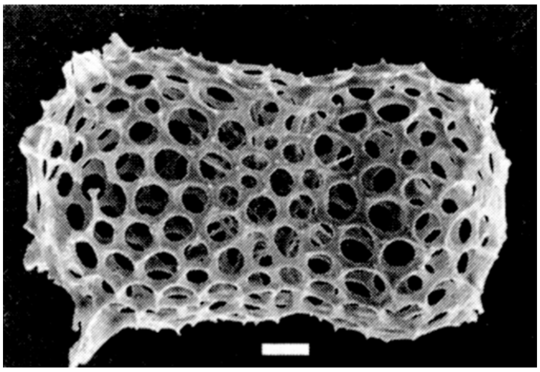

Figure 1.1: Radiolarian skeleton, scale bar: 10 µm.

Among the most important elements for living organisms calcium acquires a special position because it is extremely widespread in biominerals in the form of calcium phosphate in teeth and bones and in form of calcium carbonate such as in shells, coccoliths and exoskeletons [1].

Both, bones and teeth, are biocomposites consisting of the mineral hydroxyapatite and several proteins. In the case of bones these involve crystals of hydroxyapatite which are embedded in a matrix consisting of collagen fibrils and other proteins, whereby, after exceeding the solubility product of calcium phosphate, the collagen fibrils act as a nucleus. The combination of inorganic material associated with the proteins gives to the bones their typical mechanical properties, i. e. increased toughness, compared to the pure inorganic material, combined with elasticity. Bones are so-called “living minerals”, because they are subject to a permanent process of growing and degrading. Responsible for these processes are several different types of cells, which are enclosed in the mineral structure. Among them there are the osteoblasts which are responsible for the formation of bone tissue and the osteoclasts which prevent the continuously ungoing growing process by dissolving bone tissue [4,11,12].

Calcium carbonate has three anhydrous crystalline polymorphs, calcite, aragonite and vaterite. In addition, there is also known an amorphous form of calcium carbonate. The two most thermodynamically stable forms, calcite and aragonite, are widespread as biominerals. They are both found in many different organisms in the form of exo-skeletons [4].

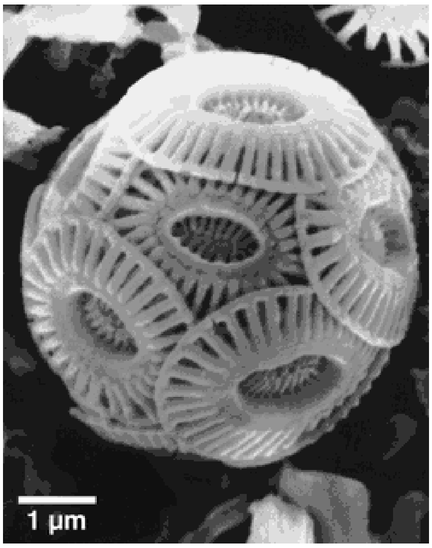

Figure 1.2: Emiliania coccosphere.

The coccoliths [9,13] consisting of calcite can serve as examples. Coccoliths are plates that cover the cell wall of the so-called coccolithophores. These are single-celled algae that are well investigated. The mineralization process in species such as Pleurochrysis carterae and Emiliania huxleyi (Figure 1.2) proceeds intracellularly within a special vesicle with the collaboration of acidic polysaccharides [14]. In Pleurochrysis the so-called coccolithosomes (nanoparticles of calcium-ions and polyanions) are attached to a preformed organic matrix by the coccolith ribbon, that is a narrow band of organic material and acts as nucleation site. A single coccolith has an highly complex structure and the whole mineralized shell consists of several of these elements.

In the majority of cases mollusc shells [15] are made of calcium carbonate. Several shells are built of calcite as well as aragonite, but in all cases the two polymorphs are spatially separated.

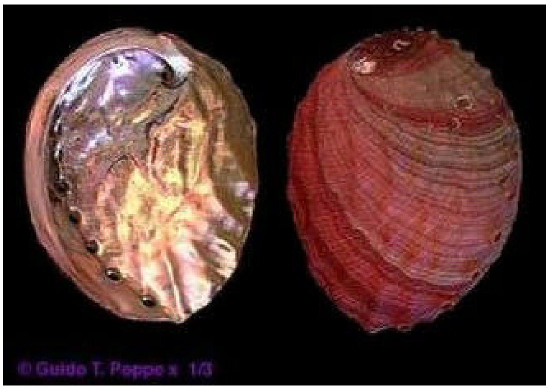

Figure 1.3: Red Abalone (Haliotis rufescens).

The abalone shell (Figure 1.3), Haliotis rufescens [9], is an example. It is a marine gastropod whose inner layer (nacre, mother of pearl) consists of aragonite tablets and whose outer layer (prismatic layer) is composed of calcite crystals. Especially the mother of pearl was and still is subject of detailed investigations. The aragonite tablets are extremely well orientated and the interspaces within this plate-like structure are filled with thin sheets of an organic matrix [16], resulting in a laminate that is built from 98 % calcium carbonate and 2 % organic material. The hierarchical structure as well as the organic material have an important impact on the mechanical properties of the material. The organic matrix inhibits crack propagation resulting in a fracture resistance that is 3000 times higher compared to that of pure aragonite [17].

The sea urchin spines [1,2] display a further example of an increasing toughness of an inorganic mineral brought about by an organic material. Usually calcite is easily cleavable along the {10.4} planes. Even though sea urchin spines are single crystals of calcite they are not cleaved this way. They contain glycoproteins of 0,02% by mass and obviously these intercalated acid macromolecules reinforce the hybrid material against fracture.

The third crystal modification of calcium carbonate, namely vaterite, is quite rarely distributed in biological systems compared to aragonite and calcite. It is to be found in marine organisms called ascidians in the form of spicules that act as a protection against predators [18,19], and in the egg shells of some gastropods [20].

Amorphous calcium carbonate (ACC) is thermodynamically and kinetically highly unstable in its pure form under physiological conditions [21,22]. Nevertheless it is found in a variety of living organisms. Biologically built amorphous calcium carbonate forms can be distinguished in such a way, whether they are stable or transform by and by into one of the crystalline phases. It is known that these two forms are different in structure and composition. As for the unstable ACC, that is acting as a transient precursor, this one is essentially anhydrous. In contrast the stable biogenic amorphous phases contain water and in a lot of cases comprise Mg and/or phosphorous, which are supposed to participate in the stabilization and/or formation process of ACC [23,24]. In addition to the impact of these ions on the stabilization process, one has also to take into account the role of macromolecules [25]. Amorphous calcium carbonate is used as temporary storage of ions, for instance in leaves of various plants [26,27]. The reason for the use of the amorphous material probably is its better solubility compared to that of the crystalline phase which makes it easily available for re-use [1]. In crustaceans amorphous calcium carbonate is used to enhance the stiffness of the exoskeletal cuticle. Also here its high solubility seems to be advantageous, facilitating the dissolution of the mineral during the molting phase [28]. In addition it is supposed to be a transient precursor phase prior to the formation of calcite in sea urchin larval spicules [29,30] or aragonite in marine larval bivalves [31].

The biomacromolecules play a key role in the formation and/or stabilization process of amorphous as well as crystalline biominerals, with the result that the biocomposites have specific and unique properties as already described above in detail.

The macromolecules can be divided into two classes, namely the soluble, hydrophilic “control macromolecules” and the insoluble matrices serving as a substratum for the crystallization process (“framework macromolecules”) [2,32].

The soluble macromolecules are often found rich in carboxylate groups deriving from proteins or polysaccharides for example. They can contain further charged groups, such as phosphate or sulphate [2,32]. All these different groups enable these macromolecules to interact either with the ions in solution and the ions of a crystal plane [33,34,35], respectively or with the solid matrices. In the former case the polymers can adsorb on specific faces of the crystal and thus control the crystallization process, whereby the distance of the charged groups that interact with the faces, is of great importance. The adsorption on a crystal plane results in a retardation of the crystal growth. Furthermore they can bind calcium ions in solution and thus have an influence on the crystallization process. In the latter case is found a cooperation of both classes of polymers. This means that the soluble polymers are being adsorbed onto the insoluble matrices as in mollusc shell nacre [32].

The soluble matrices in living organisms are proteins that are often rich in aspartic and/or glutamic acid [25,33]. Some of them contain higher amounts of polysaccharide. In general they are closely connected to the mineral phase what makes it difficult to extract and characterize them. In many tissues the extraction of these acidic proteins only is possible after the dissolution of the mineral phase [36]. Concerning the quantity the major constituents of the biological material are the framework macromolecules whose composition can vary considerably (e. g. collagen, chitin). They are often less intimately associated with the mineral phase and serve as a three-dimensional scaffold in which the formation of the mineral proceeds, often also under involvement of the hydrophilic macromolecules (“cooperative effect”). In the case of the afore-mentioned mollusc shell nacre the crystallization process proceeds inside of a scaffold. It consists of chitin/silk-fibroinlike proteins which are intimately associated with soluble acid-rich proteins [1,2,37].

The organic matrix governs the progression of the mineralization process, such as the determination of the site of nucleation, growth and morphology of the inorganic material. This means, that the formation of the inorganic precipitate is under full control of the involved soluble and insoluble macromolecules, which finally also determine the physical and mechanical properties of the resulting composite material.

This has lead to an huge interest of researchers to elucidate the phenomenon of biomineralization which is manifested in an immense multitude of publications, especially during the last two decades. These investigations are focused on the structure-function relationship of the materials and on the mode of functioning of the organic matrix. Up to now the process of biomineralization is not well understood in detail. One of the reasons is that the mimicking and understanding of the biomineralization process is complex because it is a cellular process which is under genetic control. Another reason is that the understanding of the biomineralization process at the molecular level is complicated by the fact that there is only little information regarding the three-dimensional structure of the involved proteins [2,4].

Nature is able to produce a lot of materials under physiological conditions with defined and characteristic properties of the hybrid material, such as the combination of inorganic toughness with organic elasticity, the enhancement of the fracture resistance or the reduction of brittleness. For chemists, physicians, physicists, biologists, engineers and material designers much can be learnt from these hybrid materials which could contribute to an improvement of various basic materials.

Nowadays in medical science a fracture is treated by the use of screws or metallic wires or a knee joint is replaced by an synthetic prosthesis. In doing so there always arises the question of the compatibility of this material to prevent side effects such as corrosion or inflammation. For these reasons a great importance is attached to the design and development of biomaterials with specific features. But also the understanding of the process of pathological biomineralization, such as the formation of urinary calcus or arteriosclerosis, is fundamental [12].

In addition to possible applications of biominerals in the field of medical science other applications resulting from the knowledge gained by comprehensive insight into the biomineralization process are conceivable, such as the optimization of existing materials which is often economically much more reasonable instead of searching for completely new products, whose design and development is often combined with high expenses. These applications could include materials used in the field of separation technology, where nanometer-scale pores are needed. In this context especially the afore-mentioned diatoms can serve as a model for the creation of complex and highly structured materials [38,39]. Other potential applications are conceivable in the field of catalysis or the production of ultra-thin layers as protection for soft materials [40]. The study and detailed understanding of the nucleation processes on organic substrates in biological systems could yield many potential applications. By controlled and site-directed nucleation on stereospecific polymer surfaces crystals with well-defined structure, size, orientation and morphology could be generated whose properties could be directed by the design of specific organic substrate surfaces leading to tailor-made products [37].

There is also a growing demand for materials that can be produced at low temperature and ambient pressure by means of environmentally friendly constituents. Biominerals are materials that meet these last-mentioned requirements and therefore it is very interesting to understand the process of biomineralization to be able to mimick it and use these strategies among other things for the production of thermically sensitive products.

To accomplish synthesis of bio-inspired materials it is essential to understand the principles of the biomineralization process. To elucidate the principles of biomineralization, in addition to the clarification of the chemical and structural composition of the hybrid materials, in particular the understanding of the phenomenon at the molecular level is of great importance. To attain this goal appropriate in-vitro models are required to investigate the processes proceeding at the organic-inorganic interface. The attention is especially turned to the investigation of the nucleation process that starts the formation of a solid inorganic phase on an organic substrate.

The nucleation can occur homogeneously or heterogeneously [41]. The free energy for the formation of a cluster consists of two opposite parts, namely the gained energy obtained by the formation of bulk phase and the energy needed to build new surface area. In the case of the homogeneous nucleation the formation of thermodynamically stable nuclei is brought about by the supersaturation of the depositing ions. In contrast heterogeneous nucleation is activated by an interface. As a result of the interaction of the ions at the interface the nucleation energy is lowered by decreasing the surface energy. The growth of the mineral can now occur in terms of “epitaxial lattice match” depending on the pattern of the interface. This is often reflected by a specific orientation and morphology of the crystals, which indicates the impact of an interface (e.g. an organic matrix) on the nucleation and points at the possibility to control the nucleation and growth by a defined structure of a template [42].

On the basis of these facts the modeling of the processes proceeding at an organic-inorganic interface is essential. Up to now several model systems are in use with the objective to gain deeper insight into the afore-mentioned phenomenon. One way comprises the isolation of proteins from biological material to use it afterwards in in vitro-experiments [33,34,43-45]. An alternative strategy is to use synthetic substrates. These include vesicles [46], oil/water emulsions [39], Langmuir monolayers [47,48], polymer dispersions [49,50], dendrimers [51] and self-assembled monolayers [52,53].

Tremel et al. employ self-assembled monolayers on gold surfaces [54] as model systems. By the immersion of the gold substrates into a solution of thiols, a spontaneous self-assembly of the thiols

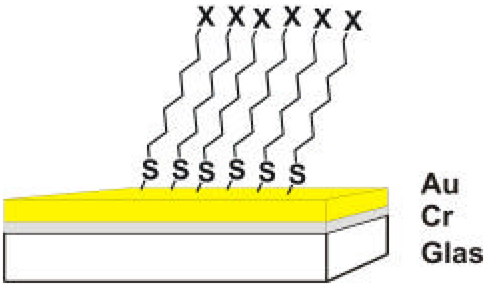

Head-groups:
x : COOH
OH
CH_3
Ar
SH
SO_3Na

Figure 1.4: Schematic illustration of a SAM on a Au surface and possible head-groups of the thiols.

onto the gold surface takes place (Figure 1.4). One advantage of this method is the strong and stable binding of the thiol group onto the gold surface as well as the temperature stability.

The a,? -functionalized mercaptoalkylthiol-mono- layers, which act as templates for the crystallization of the inorganic material, normally are composed of three parts: head group, alkyl-chain and thiol-function. Possible head groups are such as sulfate-, carboxylate-, amino-, alkyl- and hydroxy-groups. The head group is of great importance, because it is located at the monolayer/solution interface. The head group determines the properties of the surface, such as hydrophilicity, and thus has an immense impact on the crystallization products. Moreover the organization of the single molecules on the surface, which also depends on the structure of the gold surface, is a crucial factor affecting the formation of crystals.

The lattice translation of the organic layer is about 5 Å. Consequently crystal structures, which are commensurable to the lattice translation and symmetry of this one, are preferentially built. It is known that crystals can follow the geometry of the underlying nucleating substrate [55,56].

Regarding the characterization of the surfaces, various methods are applied, depending on the fact, whether the surface is to be analyzed before or after the deposition of the inorganic material. These methods include infrared, raman and surface plasmon resonance spectroscopy, as well as atomic force, scanning electron and transmission electron microscopy, measurements with the quartz crystal microbalance and x-ray diffraction.

Other parameters that can be varied to exert an influence on the crystallization process are such as the roughness of the template surface or the temperature, pH-value and concentration of the crystal forming solution.

In addition to the afore-mentioned 2-dimensional surfaces, it is also possible to use gold colloids, protected for example by thiols [57,58] as substrates for the crystallization of inorganic materials, such as calcium carbonate. These colloids can be easily obtained by the reaction of $HAuCl_4$ and $NaBH_4$ in the presence of a protecting agent. The size of these colloids lies in the range of 2-10 nm.

Tremel and co-workers [52,56,59-62] did several investigations on the crystallization process of calcium carbonate to elucidate the effect of chain length and head groups of the thiols onto phase composition, morphology and polymorphy, especially on 2-dimensional SAMs. In doing so it was shown among other things that an epitaxial growth of the crystals against the parameters of the 2-dimensional structure of the underlying template. Moreover it was revealed that the density of crystal nuclei on hydrophobic surfaces is lower compared to that on hydrophilic substrates as well as the impact of the head group on the phase composition of the deposited inorganic material. An increasing crystallization temperature leads to an increase of the aragonite phase on most of the used surfaces.

Polyaromatic amide assembled on flat gold surfaces with film thickness ranging from 5 to 400 nm was used as a nucleation template. It was found that a higher roughness of the polymer surface and a higher temperature during the crystallization process lead to an increased precipitation of aragonite [59].

Using colloids protected by p-sulfanylphenol it was found a complete enclosure of these colloids with calcite resulting in a pearl-like structure [60].

More investigations on colloids protected with tetraethylene glycol revealed that carrying out the crystallization process at pH=8 yielded a mixture of calcite, aragonite and vaterite, whereas at pH=12 spheroidal aggregates of only calcite are found [61].

So far, most investigations were done considering only interactions at the template surface. However this one represents only one part of the matrices that are involved in the process of biomineralization. In more sophisticated model experiments the effect of soluble macromolecules on the mineralization has to be probed. In particular, a possible cooperative effect between a matrix surface and a soluble macromolecule has to be investigated.

A further major aspect which is necessary to elucidate the phenomenon of biomineralization is the stadium of primary nucleation. Thereby it is necessary to analyze the process of nucleation in solution, in the presence of polyelectrolytes as well as on nanoparticles acting as templates. Here the question has to be answered, whether a nanometer-sized precursor prior to the formation of calcium carbonate polymorphs exists. The involvement of so-called “Posner cluster” ($Ca_9(PO_4)_6$) of a size smaller than 1 nm was found in the growth process of hydroxyapatite [63,64]. Discovering related nanometer components in the case of calcium carbonate could bring about fundamental insight for the understanding of nucleation in biological systems.

[1] L. Addadi, S. Weiner, *Angew. Chem.* **1992**, *104*, 159.

[2] S. Weiner, L.Addadi, *J. Mater. Chem.* **1997**, *7*, 689.

[3] For more datails see: http://spp-biomineralisation.de.

[4] S. Mann, *Biomineralization*, Oxford University Press, Oxford, **2001.**

[5] J. L. Kirschvink, D. S. Jones, B. J. McFadden, *Magnetite Biomineralization and Magnetoreception in Organisms*, Plenum, New York, **1985.**

[6] R. B. Frankel, R. P. Blakemore, *Iron Biominerals*, Plenum Press, New York, **1991.**

[7] R. P. Blakemore, *Science* **1975**, *190*, 377.

[8] D. Schüler, *J. Molec. Microbiol. Biotechnol.* **1999**, *1*, 79.

[9] E. Bäuerlein, *Biomineralization*, Wiley-VCH, Weinheim, **2000.**

[10] D. Volkmer, *Chem. unserer Zeit* **1999**, *33*, 6.

[11] P. Karlson, *Biochemie*, Georg Thieme Verlag Stuttgart, New York, **1984.**

[12] S. V. Dorozhkin, M. Epple, *Angew. Chem.* **2002**, *114*, 3260.

[13] N. Watabe, *Calcif. Tissue Res.* **1967**, *1*, 114.

[14] M. E. Marsh, D. K. Chang, G. C. King, *J. Biol. Chem.* **1992**, *267*, 20507.

[15] K. Simkiss, K. M. Wilbur in: *Biomineralization. Cell Biology and Mineral Deposition.*, Academic Press, San Diego, **1989**, 230-260.

[16] Y. Levi-Kalisman, G. Falini, L. Addadi, S. Weiner, *J. Struct. Biol.* **2001**, *135*, 8.

[17] B. L. Smith, T. E. Schäffer, M. Viani, J. B. Thompson, N. A. Frederick, J. Kindt, A. Belcher, G. D. Stucky, D. E. Morse, P. K. Hansma, *Nature* **1999**, *399*, 761.

[18] H. A. Lowenstam, D. P. Abbot, *Science* **1975**, *188*, 363.

[19] J. Aizenberg, G. Lambert, S. Weiner, L. Addadi, *J. Am. Chem. Soc.* **2002**, *124*, 32.

[20] A. Hall, J. D. Taylor, *Mineral Mag.* **1971**, *38*, 521.

[21] L. Brecevic, A. E. Nielsen, *J. Crystal Growth* **1989**, *89*, 504.

[22] N. Koga, Y. Nakagoe, H. Tanaka, *Thermochim. Acta* **1998**, *318*, 239.

[23] L. Addadi, S. Raz, S. Weiner, *Adv. Mater.* **2003**, *15*, 959.

[24] S. Raz, S. Weiner, L. Addadi, *Adv. Mater.* **2000**, *12*, 38.

[25] J. Aizenberg, G. Lambert, L. Addadi, S. Weiner, *Adv. Mater.* **1996**, *8*, 222.

[26] Y. Levi-Kalisman, S. Raz, S. Weiner, L. Addadi, I. Sagi, *Adv. Funct. Mater.* **2002**, *12*, 43.

[27] M. G. Taylor, K. Simkiss, G. N. Greaves, M. Okazaki, S. Mann, *Proc. R. Soc. London, Ser. B* **1993**, *252*, 75.

[28] P. Greenaway, *Biol. Rev.* **1985**, *60*, 425.

[29] E. Beniash, J. Aizenberg, L. Addadi, S. Weiner, *Proc. R. Soc. London Ser. B*, **1997**, *264*, 461.

[30] S. Raz, P. C. Hamilton, F. H. Wilt, S. Weiner, L. Addadi, *Adv. Funct. Mater.* **2003**, *13*, 480.

[31] I. M. Weiss, N. Tuross, L. Addadi, S. Weiner, *J. Exp. Zool.* **2002**, *293*, 478.

[32] T. Kato, A. Sugawara, N. Hosoda, *Adv. Mater.* **2002**, *14*, 869.

[33] S. Albeck, J. Aizenberg, L. Addadi, S. Weiner, *J. Am. Chem. Soc.* **1993**, *115*, 11691.

[34] J. Aizenberg, J. Hanson, T. F. Koetzle, S. Weiner, L. Addadi, *J. Am. Chem. Soc.* **1997**, *119*, 881.

[35] A. Berman, L. Addadi, A. Kvick, L. Leiserowitz, M. Nelson, S. Weiner, *Science* **1990**, *250*, 664.

[36] J. D. Termine, A. B. Belcourt, K. M. Conn, H. K. Kleinman, *J. Biol. Chem.* **1981**, *256*, 10403.

[37] S. Mann, *Nature* **1988**, *332*, 119.

[38] E. G. Vrieling, T. P. M. Beelen, R. A. Van Santen, W. W. C. Gieskes, *J. Biotechnol.* **1999**, *70*, 39.

[39] S. Schacht, Q. Huo, I. G. Voigt-Martin, G. D. Stucky, F. Schüth, *Science* **1996**, *273*, 768.

[40] A. Sellinger, P. M. Weiss, A. Nguyen, Y. Lu, R. A. Assink, W. Gong, C. J. Brinker, *Nature* **1998**, *394*, 256.

[41] I. Weissbuch, M. Lahav, L. Leiserowitz, *Crystal Growth* & *Design* **2003**, *3*, 125.

[42] K. Naka, Y. Chujo, *Chem. Mater.* **2001**, *13*, 3245.

[43] B.-A. Gotliv, L. Addadi, S. Weiner, *ChemBioChem* **2003**, *4*, 522.

[44] A. M. Belcher, X. H. Wu, R. J. Christensen, P. K. Hansma, G. D. Stucky, D. E. Morse, *Nature* **1996**, *381*, 56.

[45] A. Bermann, L. Addadi, S. Weiner, *Nature* **1988**, *331*, 546.

[46] S. Mann, J. P. Hannington, R. J. P. Williams, *Nature* **1986**, *324*, 565.

[47] S. Mann, B. R. Heywood, S. Rajam, J. D. Birchall, *Proc. R. Soc. Lond. A* **1989**, *423*, 457.

[48] D. Jacquemain, S. Grayer Wolf, F. Leveiller, M. Deutsch, K. Kjaer, J. Als-Nielsen, M. Lahav, L. Leiserowitz, *Angew. Chem.* **1992**, *104*, 134.

[49] J. N. Cha, G. D. Stucky, D. E. Morse, T. J. Deming, *Nature* **2000**, *403*, 289.

[50] H. Cölfen, L. Qi, *Chem. Eur. J.* **2001**, *7,* 106.

[51] J. J. J. M. Donners, B. R. Heywood, E. W. Meijer, R. J. M. Nolte, N. A. J. M. Sommerdijk, *Chem. Eur. J.* **2002**, *8*, 2561.

[52] J. Küther, R. Seshadri, G. Nelles, H. J. Butt, W. Knoll, W. Tremel, *Adv. Mater.* **1998**, *10*, 401.

[53] J. Aizenberg, A. J. Black, G. M. Whitesides, *J. Am. Chem. Soc.* **1999**, *121*, 4500.

[54] A. Ulman, *Chem. Rev.* **1996*,*** *96*, 1533.

[55] J. Aizenberg, A. J. Black, G. M. Whitesides, *Nature* **1999**, *398*, 495.

[56] J. Küther, R. Seshadri, W. Knoll, W. Tremel, J*. Mater. Chem.* **1998,** *8*, 641.

[57] M. Brust, M. Walker, D. Bethell, D. J. Schiffrin, R. Whyman, *J. Chem Soc. Chem. Commun.* **1994**, 801.

[58] M. Brust, J. Fink, D. Bethell, D. J. Schiffrin, C. Kiely, *J. Chem. Soc. Chem. Commun.* **1995**, 1955.

[59] M. Bartz, O. Lang, R. Kügler, Z. Ahmad, W. Knoll, W. Tremel, *J. Mater. Chem.*, submitted.

[60] J. Küther, R. Seshadri, W. Tremel, *Angew. Chem. Int. Ed.* **1998**, *37*, 3044.

[61] M. Bartz, J. Küther, G. Nelles, N. Weber, R. Seshadri, W. Tremel, *J. Mater. Chem.* **1999**, *9,* 1121.

[62] G. Nelles, H. Schönherr, M. Jaschke, H. Wolf, M. Schaub, J. Küther, W. Tremel, E. Bamberg, H. Ringsdorf, H.-J. Butt, *Langmuir* **1998**, *14,* 808.

[63] A. S. Posner, F. Betts, *Acc. Chem. Res.* **1975**, *8*, 273.

[64] K. Onuma, A. Ito, *Chem. Mater.* **1998**, *10*, 3346.

2. Investigations of Cooperative Interactions in Template Induced Crystallization Processes

2.1. Crystallization of Vaterite Nanowires by the Cooperative Interaction of Tailor-Made Nucleation Surfaces and Polyelectrolytes

2.1.1. Introduction

Many living organisms are able to control the crystallization of inorganic minerals by means of organic template molecules or biopolymers [1]. It is generally assumed that template molecules guide and control the nucleation process of the inorganic component in an epitaxial manner through the organic-inorganic interface [2,3]. In this model the functional groups of the template – in particular their spatial distribution – play a central role. However, the interface between the inorganic mineral and the organic matrix represents only a partial aspect of the biomineralization phenomenon. In addition to the proteins involved in the nucleation, there are further matrix proteins responsible for the propagation steps and mineral-binding proteins responsible for the modulation of the mineralization process [1,4,5]. Serum proteins control local pH-changes and pH-dependent complexation-/decomplexation-equilibria (e.g. by conformational changes) or have an impact on redox potentials during the transport of oxygen or the regulation of concentrations.

Because the complex interaction of many different factors is difficult to mimic in model experiments, most studies focussed almost exclusively on the nucleating matrix. One strategy is to isolate the matrix proteins which are involved in the nucleating process from biological material and to use them afterwards in in vitro-experiments [6]. An alternative approach is to employ synthetic models of the matrix proteins. In this context Langmuir monolayers [7], protein-covered substrates [8], polymer dispersions [9], oil/water emulsions [10], micellar solutions [11], liquid crystalline systems [12], vesicles [13], latex-spheres [14], self-assembled monolayers (SAM) [15] or colloids and dendrimers [16] were used as templates or substrates for the crystallization of inorganic compounds.

From investigations on marine algae (Pleurochrysis and Emiliana) it is known that acidic low-molecular polyanions are involved in the nucleation of $CaCO_3$ and the growth of $CaCO_3$ coccoliths [5,17]. Calcite nucleation is believed to occur in contact with the so-called coccolith ribbon, a narrow band of organic material. Subsequently, small crystallites appear within the particle clusters. The crystallization is terminated by the dissociation of the coccolithosome particles and the formation of a polyanion coating on the mineral surface [18]. This reaction sequence can be mimicked by a simplified model system. Our model system consists of self-assembled thiol monolayers tethered to gold colloids or to gold-covered glass substrates in the presence of a dissolved polyelectrolyt. Thiols on gold-covered glass substrates are highly organized in two dimensions [15,16,19]. The advantage of this rather simple system is that the crystallization of calcium carbonate (or other inorganic compounds) on organic monolayers [2,15,16] as well as the interaction of the polyelectrolyte with the bivalent cations [21] can be easily monitored and is quite well understood. From in-situ neutron small-angle scattering studies of the crystallization of $CaCO_3$ on templated colloids in the presence of ovalbumin it could be deduced that the mineral formation is a two-step process: in the first step $CaCO_3$ nanoparticles are formed which are transformed subsequently to $CaCO_3$ crystals [22]. In this contribution we present the first results of investigations on a model system, where through the interaction of a dissolved polyelectrolyte (polyacrylic acid, Na-salt) with a self-assembled organic monolayer nanoscopic wire-like bundles of vaterite are formed.

2.1.2. Results and discussion

Our model system consists of gold slides covered with self-assembled thiol monolayers (non-polar: alkylthiols; polar: 1,n-mercaptoalcohol; highly polar: 1,n-mercapto carboxylic acid). The aqueous solutions (pH ≈ 10) contain Ca^{2+} (0,01 m) and polyacrylate with a molecular weight of 30.000 or 240.000 D, respectively. The mineralization of $CaCO_3$ is started by the thermal decomposition of ammonium carbonate and subsequent diffusion of the evolving CO_2 into the solution. After several hours long wires with a diameter of about 250 nm and a length of more than 100 µm are formed (Figure 2.1.1).

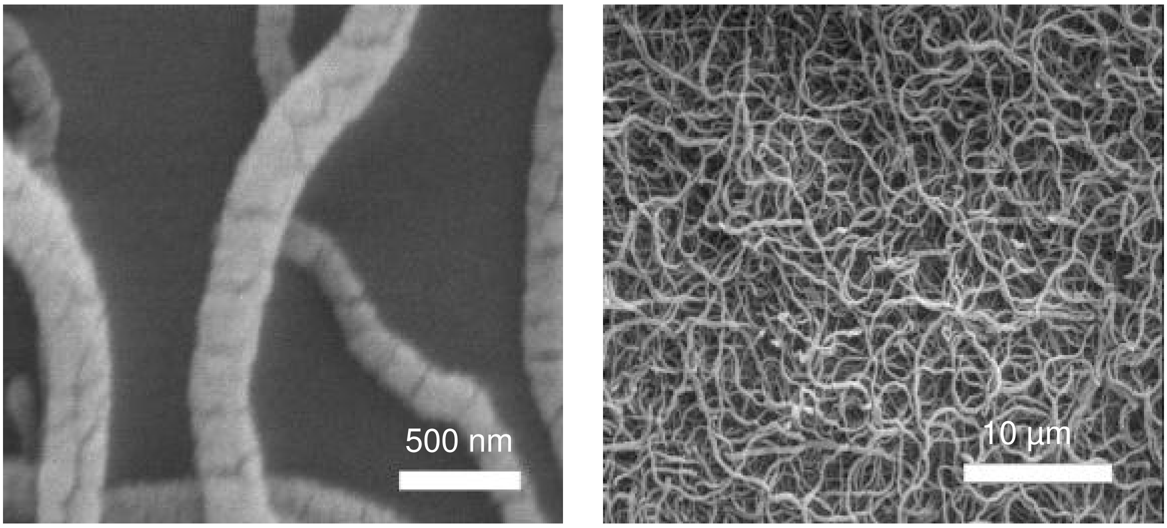

Figure 2.1.1: SE micrographs of $CaCO_3$-aggregates grown on a COOH-terminated gold slide in the presence of polyacrylate.

Using micro-Raman spectroscopy [23] the phase composing the wire could be identified unambiguously as vaterite (hexagonal $CaCO_3$). With the aid of this method it is possible, to distinguish and positionally resolve µm-sized aggregates of the $CaCO_3$ minerals calcite (trigonal), aragonite (rhombic) and vaterite [23]. A typical Raman spectrum of the fiber-aggregates is shown in Figure 2.1.2a. The presence of vaterite was confirmed independently by X-ray diffraction (Figure 2.1.2b). From the X-ray data there was no indication of preferred orientation of the vaterite crystallites. Transmission electron micrographs of the vaterite-wires (Figure 2.1.2c+d) indicate the growth of nanometer sized crystallites around a common backbone.

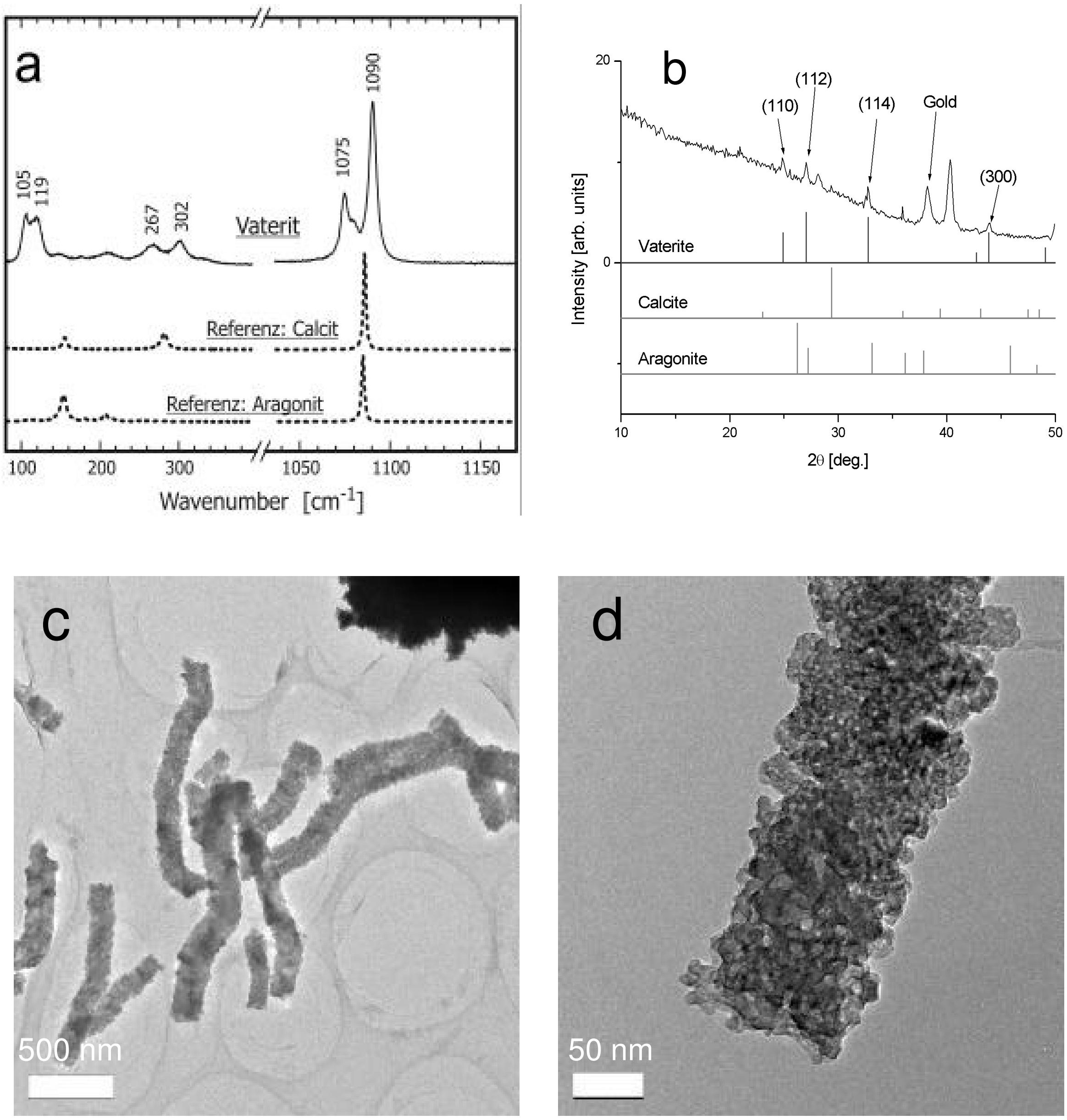

Figure 2.1.2: (a) Raman-spectra, (b) x-ray-spectra, (c) and (d) TEM-graphs of the fiber-like aggregates of Figure 2.1.1.

This interpretation is backed by HR-SEM measurements (Figure 2.1.3). The presence of a polyacrylate backbone is supported by the results of DSC studies of the vaterite nanowires that reveal an organic portion of approximately 1%.

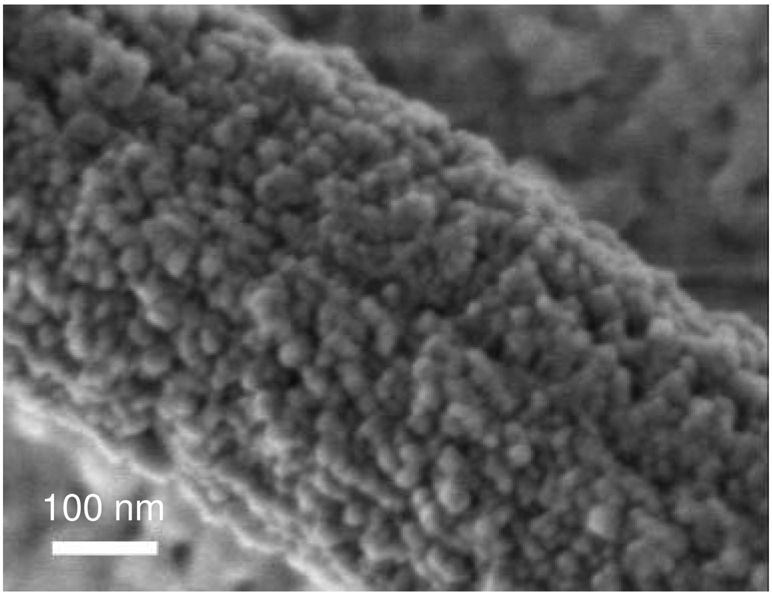

Figure 2.1.3: HR-SEM graph of the fiber-like aggregates of Figure 2.1.1.

The crystal aggregates shown in Figure 2.1.1 exhibit structural organization at several levels: (1) crystallinity in the atomic, (2) an extremely distinct aspect ratio in the mesoscopic and (3) formation of crystallites in the microscopic range. Its striking characteristic is the wire-like morphology. The phase selection may be rationalized quite easily, because it is well-known that the crystallization of calcium carbonate in the presence of glutamate- or aspartate-additives leads to a preferred formation of vaterite as the kinetically stabilized polymorph of $CaCO_3$ [24].

How can we account for the wire-like morphology of the product? The only other known synthetic example was obtained from the crystallization of $CaCO_3$ in oil-water-surfactant-emulsions [10a]. One possible explanation for the formation of wire bundles is based on the unfolded polymer strand as a matrix for the crystallization process. In this case the polyacrylate would act as organic backbone for the vaterite fibers – the carboxylate groups of the polyacrylate chain act as complexating agents for the Ca^{2+} cations which in turn bind carboxylate groups from the solution. As a result, the polymer chain acts as a nucleation center in the {001} plane of vaterite. We assume that the polymer is grafted as a coil of strands to the surface (Figure 2.1.4); the individual strands of the coil interpenetrate and exhibit a spaghetti-type appearance which is reflected in the morphology of the product.

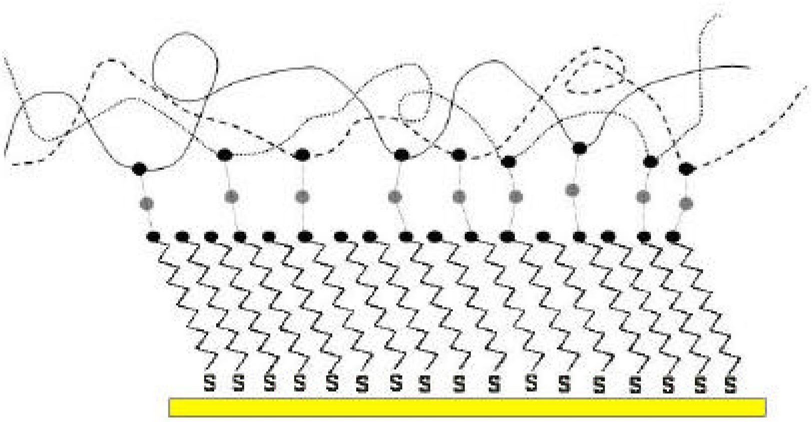

Figure 2.1.4: Polymer strands grafted to a carboxylated surface by the mediation of Ca^{2+}-ions (COOH = black sphere, Ca^{2+} = grey sphere).

The attachment of the polymer strands to the surface is not due to the direct interaction of the carboxylic groups of the polymer and the carboxylic groups of the SAM, but it is mediated by the Ca^{2+}-ions. This is demonstrated by the QCM-results illustrated in Figure 2.1.5.

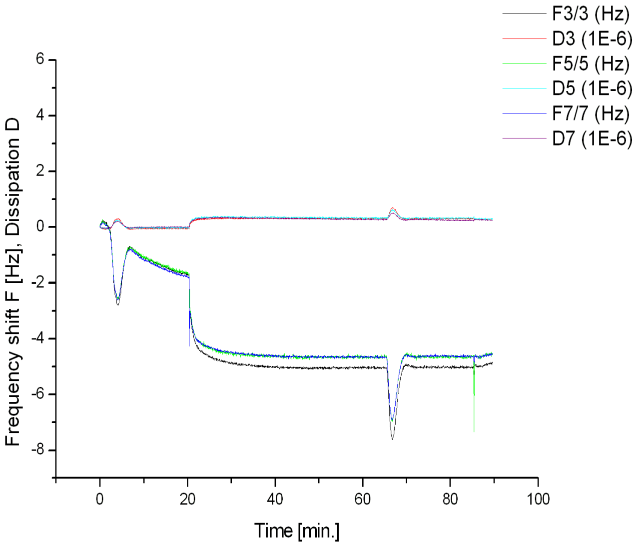

Figure 2.1.5: QCM-measurement of a solution of polyacrylate in water without $CaCl_2$.

It displays the adsorption of polyacrylate onto a carboxylated surface in salt-free water. Replacing salt-free water adjusted to pH=10 after 20 min. with an aqueous salt-free solution composed of water and polyacrylate (pH=10) results in a frequency shift of only 3 Hz corresponding to a marginal mass adsorption of the polyacrylate onto the surface. This frequency shift is very small compared to the change of frequency in a solution containing Ca^{2+}-ions, which will be shown later (see Figure 2.1.6).

This hypothesis is backed partly by experimental results. From light scattering experiments on polymethacrylic acid it is known, that high concentrations of bivalent cations lead to an unfolding of the polymer chain [21], which may be attributed to a complexation of the M^{2+} cations and a concomitant loss of hydrogen bridges within the polymer. Similarly, polymer unfolding may be expected at basic pH values. Applying these ideas to our model system we should expect – in contrast to the experimental results – wire-like polymer/$CaCO_3$-composits irrespective of the underlying thiol monolayer.

A plausible interpretation of the experimental results can be obtained only when an interaction between the polymer and the template surface is included in the explanation. We assume that the polymer can unfold when the Ca^{2+} concentration is large enough. If the polarity of the SAM surface layer is sufficiently high to ensure the attachment and unfolding of the polymer strands by Ca^{2+} complexation, the surface and/or the polymer may serve as a template for the mineralization process. This condition seems to be fulfilled only, if a carboxylate-terminated monolayer is present. This model is corroborated by the results of in-situ surface plasmon resonance spectroscopy (SPRS) and measurements with a quartz balance (QCM) which indicated a significant polymer adsorption only for carboxylate-terminated monolayers. Monitoring the surface growth from solutions containing only Ca^{2+}-ions and polymer by SPRS as a function of time reveals that a surface layer with a thickness of about 20 nm is formed within a few minutes. We ascribe the formation of this surface layer to the attachment of the polymer to the carboxylate-terminated template monolayer. This assumption is confirmed by the results of QCM-measurements on COOH- and CH_3-terminated SAMs. Figure 2.1.6 displays the attachment of the polyacrylate on a COOH-terminated SAM-surface. Replacing an aqueous solution of pH 10 containing Ca^{2+}-ions after about 64 min.

with the same solution, but containing polyacrylate, a strong frequency shift of more than 100 Hz is visible due to the adsorption of polyacrylate onto the surface. Corresponding measurements on a CH_3-terminated SAM-surface resulted in a frequency shift which is smaller by an order of magnitude.

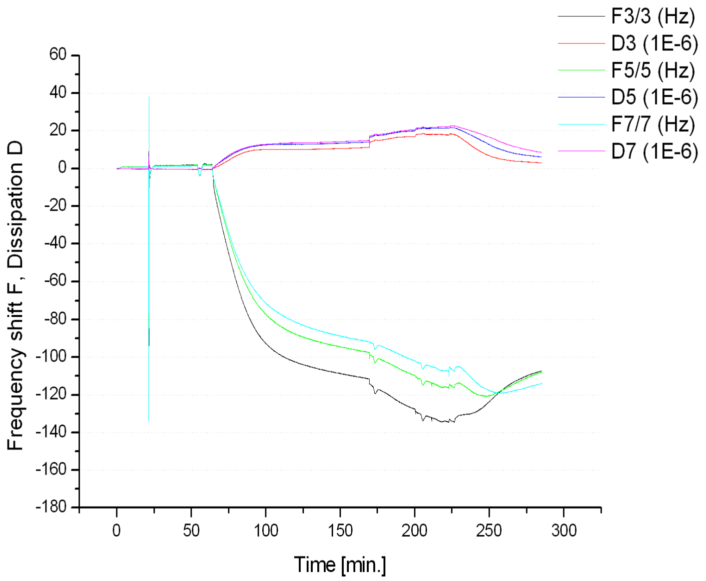

Figure 2.1.6: QCM-measurement of a Ca^{2+}-ions containing solution of polyacrylate on a carboxylated surface.

Attempts to demonstrate the attachment of the polyacrylate to the surface by measuring the refractive index of the polyacrylate containing solution during the adsorption process were unsuccessful because the refractive index of the pure $CaCl_2$ solution does not differ significantly from that of a $CaCl_2$ solution containing polyacrylate due to the small concentration of polyacrylate.

Based our present data, however, we cannot exclude clearly, whether $CaCO_3$ nucleates on the substrate with attached polymer directly or by the aggregation of PAA and $CaCO_3$ particles formed in solution. However it seems likely that nanometer-sized particles pre-formed in solution are being attached to the polymer template. We were able to demonstrate the presence of these particles in a polyacrylate solution by TEM-measurements (Figure 2.1.7). The samples were taken one hour after the start of the mineralization process by allowing carbon dioxide to diffuse into the solution. The sample contained small $CaCO_3$ particles with a size of about 10 nm which were shown to be crystalline by X-ray diffraction.

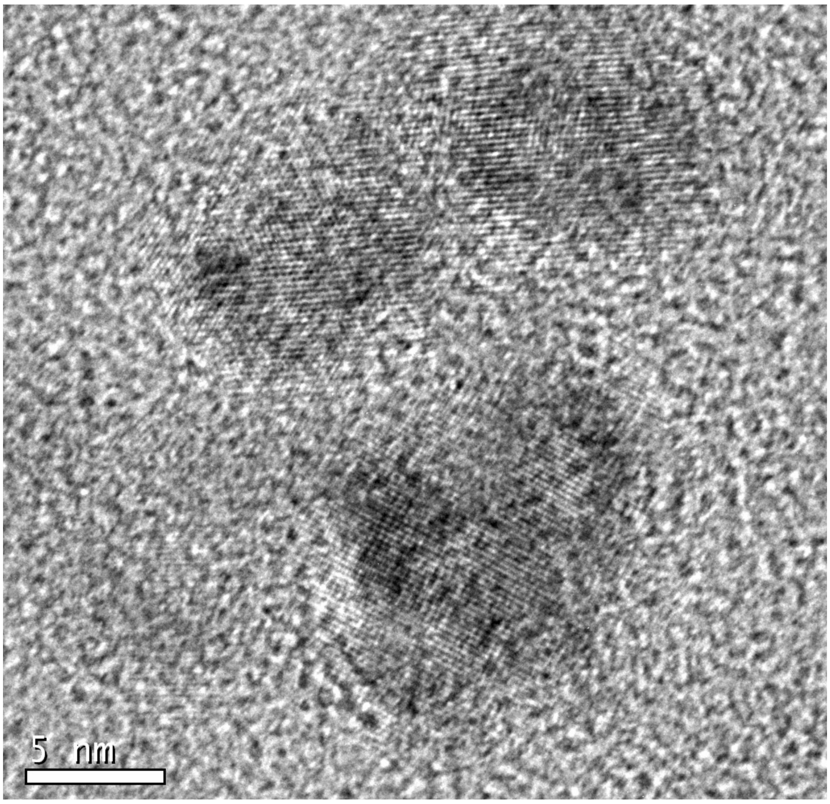

Figure 2.1.7: TEM-graph demonstrating the presence of nanometer-sized $CaCO_3$-particles about one hour after starting the mineralization process.

Samples taken about 20 min. after starting the mineralization process seemed to be amorphous. During the examination of these particles in the TEM we observed the transformation from an amorphous to a crystalline phase within only few minutes (Figure 2.1.8). The transformation process seems to be induced by the high energy electron beam.

Obviously, amorphous particles are present at the start of the mineralization process, but they transform within a short period of time (< 60 min) to crystalline material.

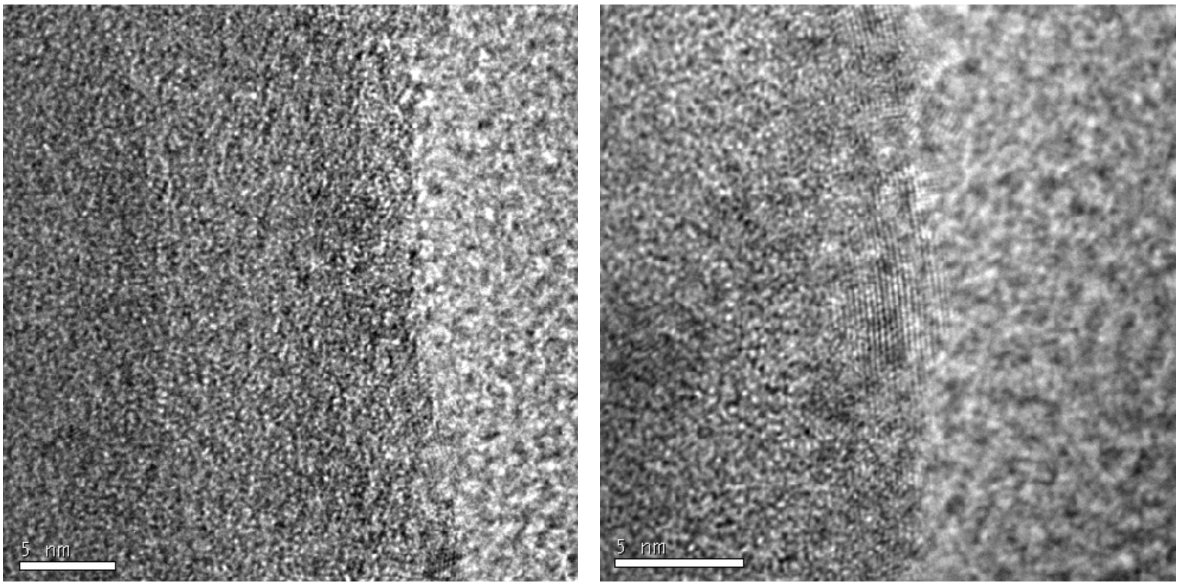

Figure 2.1.8: TEM-graphs demonstrating the presence of an amorphous particle (left) and the transformation of this particle into a crystalline phase (right) caused by the beam energy.

It is well known that ACC rapidly transforms to crystalline phases in the presence of water. Li and Mann could demonstrate that in inverse microemulsions surfactant-vaterite structures with different shapes are formed by a phase transition from stabilized ACC nanoparticles. The addition of water to the ACC nanoparticles caused their self-aggregation and transformation to vaterite [25].

From the molecular weight of the polyacrylic acid we estimate the persistence length of a polymer strand to approx. 150 nm, whereas the length of a vaterite wire appears to be in the micrometer range. This raises the question how the length of the vaterite wires can be explained. As the diameter of a single polymer strand (Ø ˜ 0.5 nm) is small compared to that of a vaterite wire (Ø ˜ 250 nm) as shown in Figure 2.1.1 we must assume that a vaterite wire embeds several hundred partially overlapping polymer strands. A possible explanation is as follows: Ca^{2+} cations with a coordination number 6 should be coordinated by at least three carboxylate groups of one or several polymer strands as illustrated in Figure 2.1.9. As a result, the Ca^{2+} cations may link several polymer strands by complexation and such an aggregate may easily contain many PAA molecules. This would be compatible with the observed length of the vaterite wires and the fact that polycarboxylates with intermediate/high molecular weights are used as water dehardeners due to their crosslinking ability by bivalent Ca^{2+}.

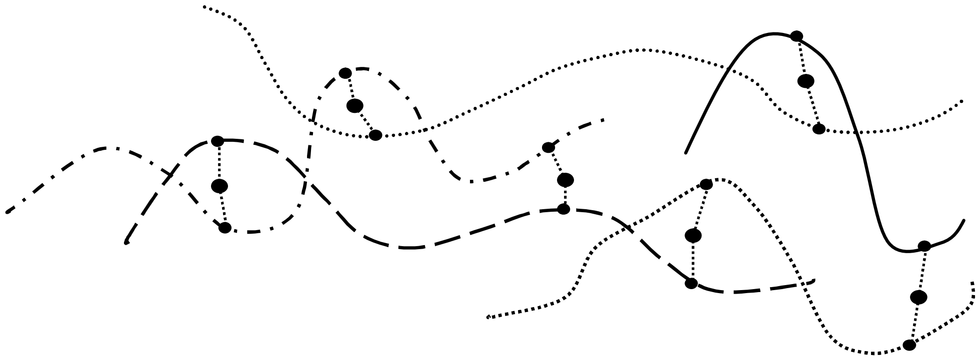

Figure 2.1.9: Schematical linkage of polymer strands by complexation of Ca^{2+}-ions.

For alkyl- or OH-terminated monolayers no surface layer formation (i.e. no binding of the polymer to the surface) was observed. The polymer remains in solution and nucleation and crystal growth of $CaCO_3$ take place on the SAM monolayer. Therefore, in the case of the OH-terminated and alkyl-terminated monolayers no wire-like aggregates, but isolated calcite and vaterite-crystals (Figure 2.1.10a) as well as compact vaterite layers (Fig. 2.2.10b) are formed. Their morphologies differ significantly from those of the products that were obtained in control experiments without polyacrylate [15c], i.e. the polyacrylate has an effect on the morphology of the $CaCO_3$ products as well. We believe that the isolated $CaCO_3$-crystals are coated by the polyacrylate; this can be concluded from the rounded surfaces, i.e. that the effect of the polymer here corresponds to that of an additive. The phase identities of the calcite and vaterite aggregates shown in Fig. 2.1.10a as well as the $CaCO_3$ layers shown in Fig. 2.1.10b could be assigned unambiguously by Raman microscopy. Our results are summarized in Table 2.1.1.

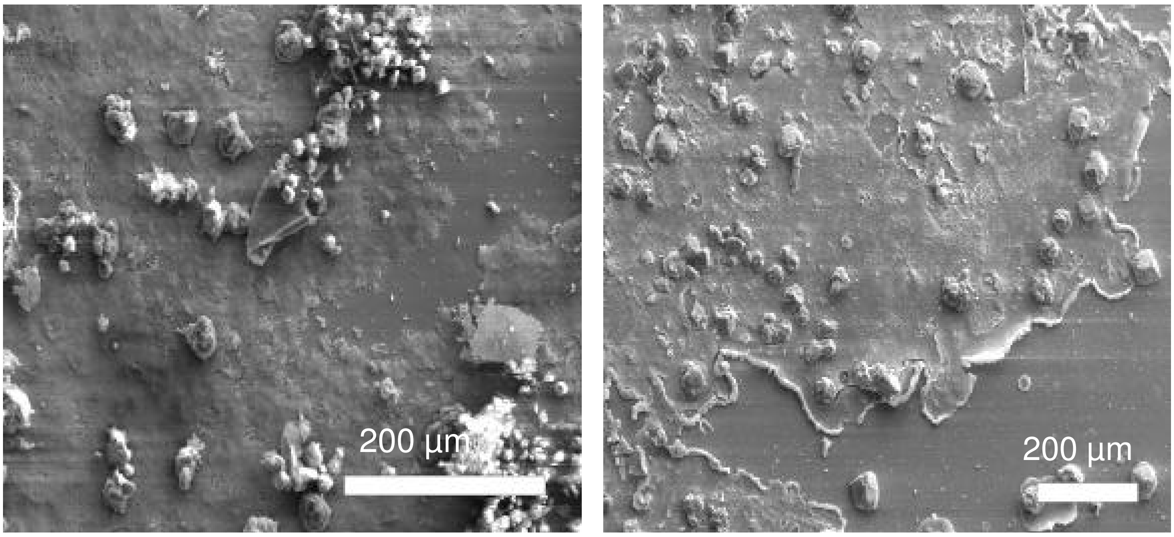

Figure 2.1.10: SE-micrographs of $CaCO_3$ obtained on (a) an OH-terminated and (b) CH_3-terminated monolayer in the presence of polyacrylate.

Table 2.1.1: Crystalline phases found on different terminated SAMs in the presence and absence of polyacrylate.

SAM head group	-COOH	-OH	$-CH_3$
with polyacrylate	vaterite wires	calcite/vaterite crystallites	compact vaterite films
without polyacrylate	aragonite and calcite crystallites	mainly calcite crystallites and smaller amount of vaterite crystallites	predominantly calcite crystallites

A control experiment performed in the presence of polyacrylate but in the absence of any SAM-surfaces did not reveal the formation of vaterite nanowires (Figure 2.1.11). Further control studies on carboxylate terminated SAMs indicated that the wire formation is independent of the polymer moleweight, and a threshold polymer concencentration (> 13 mg/l) is needed for the wire formation. Temperature dependent studies for a typical polymer concentration of 27 mg/l indicate no wire formation at room temperature and below, whereas at 45℃ large amounts of wires could be obtained. Experiments conducted at 70℃ on carboxylate terminated SAMS reduced the wire yield and only isolated vaterite nanowires were formed.

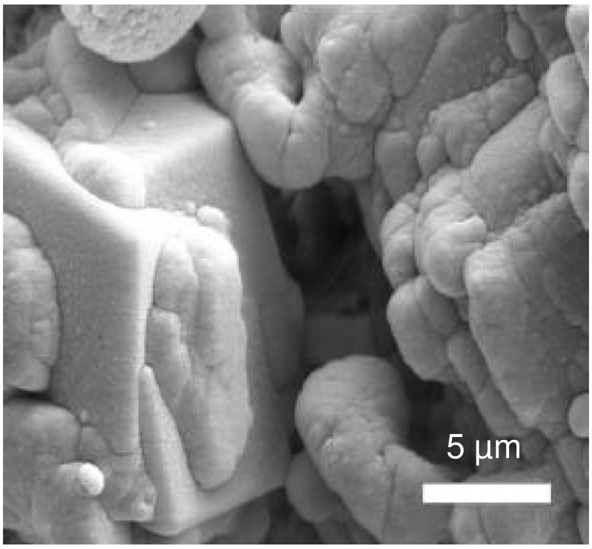

Figure 2.1.11: SE-graph of the morphologies of the products obtained in control experiments with polyacrylate but in the absence of any SAM.

2.1.3. Conclusion

In conclusion, we combined in this work the ideas of template-induced crystallization on SAMs and polymer additives to a new strategy, which includes the interaction of several components, namely (i) a matrix participating in the nucleation process, (ii) a dissolved polyelectrolyte and (iii) the ions in solution. By the combined interaction of these components, ordered mineral composite structures were formed. The model of cooperative formation of the vaterite nanowires represents for the first time an alternative to models of structure formation [10], where (i) two-phase systems (e.g. micro-emulsions or foams) act as a structure-directing interface or (ii) the mineralisation process is caused by the diffusion of a hydrolysable component from a non-aqueous into an aqueous phase [26].

2.1.4. Experimental

Glass slides were cleaned by placing them in a mixture of water, ammonia solution (28-30%) and hydrogen peroxide (5:1:1 by volume). The mixture was heated to 80℃ and held at this temperature for 10 min. After cooling to room temperature they were rinsed with water and blown dry with nitrogen. After transfering them to the vacuum chamber of a coating unit (Balzer Baltec), the slides were evaporated with 3 nm of Cr followed by 50 nm of Au. The slides were then held for about 24 h in an 1 mM solution of the thiol in toluene or ethanol. After extensive rinsing with toluene or ethanol to remove unbound thiols, the surface was blown dry with nitrogen. These slides were put face down in a crystallization flask containing 300 ml of a 10 mM $CaCl_2$-solution. 4 mg of polyacrylate (sodium-salt, MW=30.000) was added and the pH-value adjusted to 10 with an aqueous NaOH-solution. The flask was placed in a desiccator and stored for thermal equilibration for 30 min. in a temperature-controlled oven (T=45°C). Afterwards the crystallization process was started by placing a petri dish with 6 g $(NH_4)_2CO_3$ at the bottom of the desiccator. The crystallization process was stopped after 48 h, the slides were removed and dried.

For SEM the slides on which the crystallization was carried out were cut in small pieces and fastened with conducting clue on aluminium sample holders. Afterwards they were sputtered with gold before inserting them into the SE microscope. The SE micrographs were acquired on a Zeiss DSM 962 at an acceleration voltage of 15 kV.

Raman micro-spectroscopy was performed with a LabRAM HR800 (Jobin Yvon, Horiba). This confocal Raman system is based on a dispersive spectrometer with notch-filter and focus length of 800 mm. It is equipped with an optical microscope Olympus BX41 and Peltier-cooled CCD-detector (Charge-coupled device). The spectra were excited with a 638,17 Å emission of a He-Ne-laser. The lateral resolution was better than 1,5 µm and the volume resolution was ca. 5 μm^3. The precision of the wave number was 0,5 cm^{-1} and the spectral resolution was about 0,7 cm^{-1}.

For the investigation of the samples using HRTEM (TECNAI F30 with FEG), the substance was suspended in methanol and afterwards several drops of this suspension were placed on a copper grid with a holey carbon film.

QCM-D-measurements were performed on a Q-sense D 300 system (Q-sense, Sweden). AT-cut quartz crystals coated with gold films were cleaned prior to use by a treatment with H_2O_2/NH_3/Millipore-water (1:1:5 by volume). They were held for 10 min. at 800C and subsequently rinsed with Millipore-water and isopropanol. After drying with N_2 the crystals were exposed to a diluted thiol-solution, afterwards rinsed with solvent and dried with N_2. After inserting them into the cell the temperature-controlled measurements were started in a pH-adjusted 0,01 M $CaCl_2$-solution. By exchanging this liquid for a corresponding solution containing polyacrylate the adsorption of the polymer onto the thiol-terminated gold surface was monitored by a decrease of the frequency. Furthermore, the energy dissipation D was measured simultaneously. The measurements were performed in a static solution (batch mode).

Wide angle X-ray experiments in reflection geometry were carried out on a Seifert XRD 3003 TT diffractometer using Cu-Ka radiation. The diffractometer was equiped with a Goebel-mirror as a monochromator and collimator a scintillation counter and with a z-translation stage for sample alignment. The sample was placed on the horizontal sample holder and its surface aligned to coincide with the rotational axis of the diffractometer. Diffraction data were collected in a range of 2,5° < ? < 25° in steps of 0,05°.

2.1.5. References

[1] (a) H. A. Lowenstam, S. Weiner (Eds.), *On Biomineralisation* Oxford University Press, New York, **1989**. (b) S. Mann, J. Webb, R.J.P. Williams, *Biomineralization: Chemical and Biochemical Perspectives*, VCH Publishers, New York, **1989**.

[2] L. Addadi, S. Weiner, *Angew. Chem.* **1992**, *104*, 159-176; *Angew. Chem. Int. Ed. Engl.* **1992**, *31*, 153-170. (b) S. Mann, D.D. Archibald, J.M. Didymus, T. Doughlas, B.R. Heywood, F. Meldrum, N.J. Reeves, *Science* **1993**, *261*, 1286-1292.

[3] L. Addadi, S. Weiner, *Proc. Natl. Acad. Sci. U.S.A.* **1985**, *82*, 4110-4114.

[4] A.M. Belcher, E.E. Gooch, in Biomineralization, *From Biology to Biotechnology and Medical Application*, Hrgb.: E. Bäuerlein, Wiley-VCH, Weinheim, **2000**, 221-249.

[5] M.E. Marsh, in Biomineralization, *From Biology to Biotechnology and Medical Application*, Hrgb.: E. Bäuerlein, Wiley-VCH, Weinheim, **2000**, 251-268.

[6] Y. Levi, S. Albeck, A. Brack, S. Weiner, L. Addadi, *Chem. Eur. J.* **1998**, *4*, 389-396.

[7] D. Jaquemain, S.G. Wolf, F. Leveiller, M. Deutsch, K. Kjaer, J. Als-Nielsen, M. Lahav, L. Leiserowitz, *Angew. Chem.* **1992**, 104, 134-158; *Angew. Chem., Int. Ed. Engl.* **1992**, *31*, 130-152.

[8] S. Weiner, L. Addadi, *J. Mater. Chem.* **1997**, 7, 689-702.

[9] (a) J.M. Marentette, J. Norwig, E. Stöckelmann, W.H. Meyer, G. Wegner, *Adv. Mater.* **1997**, *9*, 647-650. (b) M. Templin, A. Frank, A. DuChesne, H. Leist, Y.M. Zhang, R. Ulrich, V. Schadler, U. Wiesner, *Science* **1997**, *278*, 1795-1798. (c) J.N. Cha, G.D. Stucky, D.E. Morse, T.J. Deming, *Nature* **2000**, *403*, 289-292. (d) H. Cölfen, L. Qi, *Chem. Eur. J.* **2001**, 7, 106-116. (e) L. Qi, H. Cölfen, M. Antonietti, M. Li, J.D. Hopwood, A.J. Ashley, S. Mann, *Chem. Eur. J.* **2001**, *7*, 2526-3532.

[10] (a) D. Walsh, S. Mann, *Nature* **1995**, *377*, 320-323. (b) S. Schacht, Q. Huo, I.G. Voigt-Martin, G.D. Stucky, F. Schüth, *Science* **1996**, *273*, 768-771.

[11] D. Walsh and S. Mann, *Adv. Mater.* **1997**, *9*, 658-662.

[12] (a) C.T. Kresge, M.E. Leonowicz, W.J. Roth, J.C. Vartuli, J.S. Beck, *Nature* **1992**, *359*, 710-712. (b) G.S. Attard, J.C. Glyde, C.G. Göltner, *Nature* **1995**, *378*, 366-368.

[13] S.S. Kim, W.Z. Zhang, T.J. Pinnavia, *Science* **1998**, *282*, 1302-1305.

[14] (a) F. Caruso, R.A. Caruso, H. Möhwaldt, *Science* **1998**, *282*, 1111-1114. (b) B.T. Holland, C.F. Blanford, T. Do, A. Stein, *Chem. Mater.* **1999**, *11*, 795-805.

[15] (a) D. D. Archibald, S. B. Quadri, B. P. Gaber, *Langmuir* **1996**, *12*, 538-546. (b) J. Küther, W. Tremel, *J. Chem. Soc. Chem. Commun.* **1997**, 2029-2030. (c) J. Küther, R. Seshadri, W. Knoll, W. Tremel, *J. Mater. Chem.* **1998**, *8*, 641-650. (d) J. Küther, G. Nelles, R. Seshadri, M. Schaub, H.-J.Butt, W. Tremel, *Chem. Eur. J.* **1998**, *4*, 1834-1842. (e) J. Küther, R. Seshadri, G. Nelles, H.-J. Butt, W. Knoll, W. Tremel, *Adv. Mater.* **1998**, *10*, 401-404. (f) J. Aizenberg, A. J. Black, G. M. Whitesides, *J. Am. Chem. Soc.* **1999**, *121*, 4500-4509.

[16] (a) J. Küther, R. Seshadri, W. Tremel, *Angew. Chem.* **1998**, *110*, 3196-3199; *Angew. Chem., Int. Ed. Engl.* **1998**, *37*, 3044-3047. (b) J. Küther, R. Seshadri, G. Nelles, W. Assenmacher, H-J. Butt, W. Mader, W. Tremel, *Chem. Mater.* **1999**, *11*, 1317-1325. (c) M. Bartz, J. Küther, G. Nelles, N. Weber, R. Seshadri, W. Tremel, *J. Mater. Chem.* **1999**, *9*, 1121-1125. (d) J.J.J.M. Donners, B.R. Heywood, E.W. Meijer, R.J.M. Nolte, N.A.J.M. Sommerdijk, *Chem. Eur. J.* **2002**, *8*, 2561-2573.

[17] M.E. Marsh, D.K. Chang, G.C. King, *J. Biol. Chem.* **1992**, *267*, 20507-20512.

[18] M.E. Marsh, *Protoplasma* **1994**, *177*, 102-122.

[19] A. Ulman, *Chem. Rev.* **1996**, *96*, 1533-1554.

[20] S. Mann, *Angew. Chem.* **2000**, *112*, 3532-3548; *Angew. Chem., Int. Ed. Engl.* **2000**, *39*, 3392-3406.

[21] Y. Ikeda, M. Beer, M. Schmidt, K. Huber, *Macromolecules* **1998**, *31*, 728-733.

[22] M. Balz, D.Schwahn, M.Bartz, A.Fomenko, L. Nasdala, W. Hofmeister, W.Tremel, manuscript in preparation.

[23] L. Nasdala, A. Banerjee, T. Häger, W. Hofmeister, *Microscopy and Analysis, Europ. ed.* **2001**, *70*, 7-9.

[24] F. Manoli, E. Dalas, *J. Cryst. Growth* **2001**, *222*, 293-297.

[25] M. Li, S. Mann, *Adv. Funct. Mater.* **2002**, 12, 773-779.

[26] (a) R.J. Davis, Z. Liu, *Chem. Mater.* **1997**, *9*, 2311-2324. (b) C.E. Fowler, D. Khushalani, S. Mann, *J. Chem. Soc., Chem. Commun.* **2001**, 2028-2029. (c) D. Volkmer, S. Tugulu, M. Fricke, T. Nielsen, *Angew. Chem.* **2003**, *115*, 60-64; *Angew. Chem., Int. Ed. Engl.* **2003**, *42*, 58-61.

2.2. Crystallization of Strontianite Nanowires on Self-assembled Monolayers in the Presence of Polyacrylate

2.2.1. Introduction

The design and development of strategies that allow to control the growth of inorganic minerals by chemical means has attracted the attention of researchers from a variety of fields. The ultimate goal is to exert control on the polymorphic structure, size and morphology of inorganic materials during their in-vitro production processes. Nature uses self assembly processes efficiently in the synthesis of biominerals [1] as many living organisms are able to build up complex inorganic structures with hierarchical organization at various levels [2,3]. These self-assembly processes are controlled by specialized macromolecules. It is generally assumed that template molecules guide the nucleation process of the inorganic component in a quasi-epitaxial manner at an organic-inorganic interface [4,5]. The controlled nucleation and growth of inorganic compounds from organic templates has been achieved in a number of systems using Langmuir monolayers [6], protein-covered substrates [7], polymer dispersions [8], oil/water emulsions [9], micellar solutions [10], latex spheres [11], matrix proteins isolated from biological material [12], self-assembled monolayers (SAM) [13], colloids or dendrimers [14]. These studies on templated surfaces suggest that nucleation occurs on surfaces which expose repetitive patterns of anionic groups, which tend to concentrate inorganic cations by complexation followed by creating local supersaturation which in the sequel leads to the nucleation of inorganic mineral at this interface. Another group of proteins is assumed to control the ion concentrations, i.e. mineralization inhibitors and promoters, and a third group of macromolecules is involved in the growth process [15,16].

A modeling of these processes, even at the lowest level, is a difficult task because it involves several reaction steps that require the spatial orientation of macromolecules with respect to an interface as well the uptake or release of ions. One way to accomplish at least one of these steps in an artificial system is to utilize macromolecules that form nanosize structures at an interface that can exert control during the nucleation and growth of an inorganic phase. In biological systems insoluble macromolecules (e.g. collagen, polysaccharides) form a rigid matrix to which soluble macromolecules are being tethered [1].

In this work we have tried to mimic these processes by using a simplified model system. To date, there are only few studies that account for the combination of soluble acidic and insoluble macromolecules [17]. Our model system consists of ω-substituted alkylthiol monolayers fixed on gold surfaces in the presence of a dissolved polyelectrolyte as a template for the nucleation of the inorganic compound (e.g. $CaCO_3$). Thiols on gold-covered glass substrates are highly ordered and organized in two dimensions [13,18]. The advantage of this system is that the formation of self-assembled monolayers (SAM) is well characterized and the crystallization products can be easily monitored.

Here we present first results of investigations on $SrCO_3$ crystallization [13d,19] carried out by the binding of sodium polyacrylate to a SAM mediated by Sr^{2+} cations in aqueous solution. Even though $SrCO_3$ itself is not an important biomineral, the morphology of the crystallization product provides insights into the process of formation and growth depending on the interaction of the SAM and the polymer.

2.2.2. Results and discussion

As a model system we used monolayers of thiols self-assembled on a gold slide. The thiols bear differently functionalized end-groups with non-polar (alkylthiols) and highly polar (1,n-mercapto carboxylic acid) functionalities. The crystallization process is intiated by the thermal decomposition of ammonium carbonate and subsequent diffusion of the evolving CO_2 into an aqueous solution containing Sr^{2+} and polyacrylate (pH 10). The mineralization process is stopped after about 24 hours. SEM images indicate the formation of long wires with a diameter of about 150 nm and a length of sometimes more than 100 µm (Figure 2.2.1).

The crystallization products shown in Figure 2.2.1 display a large aspect ratio and they are composed of nanometer-sized crystallites as demonstrated in Figure 2.2.2a. A striking characteristic is their wire-like morphology. A further feature is that the wires seem to be “twisted” along their axes. AFM studies reveal that the wires are composed of granular particles with diameters of approximately 30 nm.

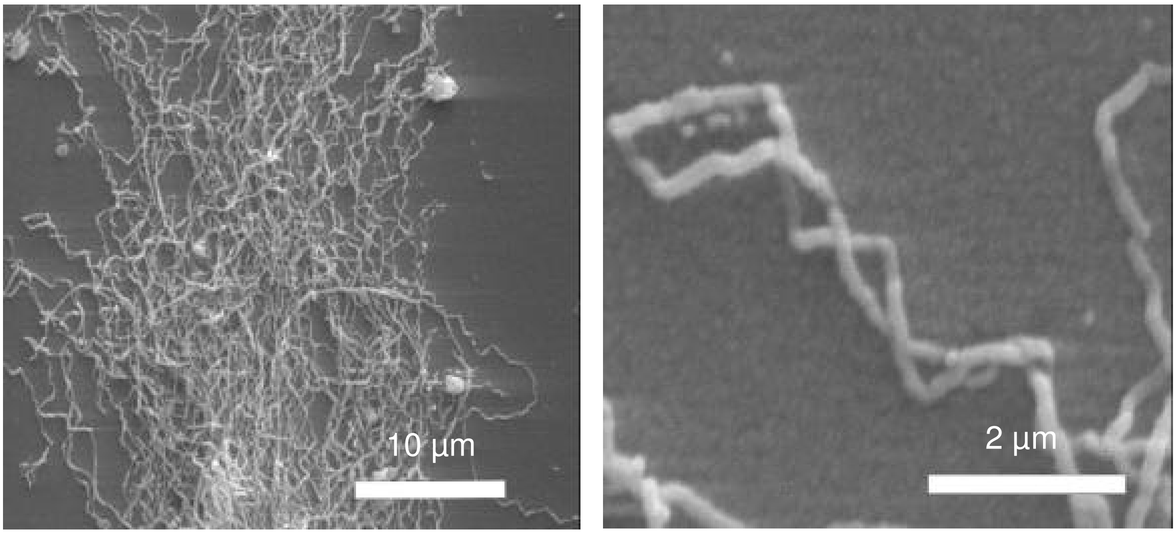

Figure 2.2.1: SE micrographs of $SrCO_3$-aggregates grown on a COOH-terminated gold slide in the presence of polyacrylate.

In contrast to calcium carbonate with the known polymorphs calcite, aragonite and vaterite only one stable polymorph, strontianite – isostructural with aragonite – is known for strontium carbonate. The phase identity strontianite could be proven by Micro-Raman spectroscopy [20]. By applying this method it is possible to distinguish and positionally resolve µm-sized aggregates of different morphology or polymorphic structure [20]. The Raman spectrum of the $SrCO_3$ wires is shown in Figure 2.2.2b.

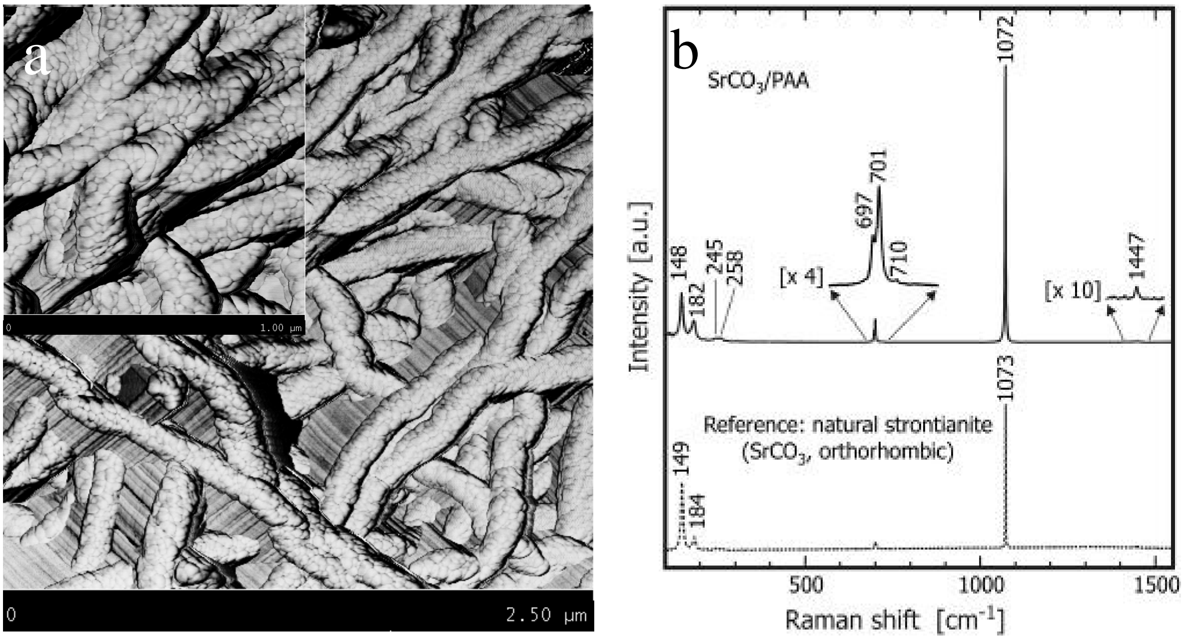

Figure 2.2.2: (a) AFM-graph of $SrCO_3$ wires that have diameters of 150 nm and a length of several micrometers. The $SrCO_3$ nanowires are composed of monodispers particles with diameters of approx. 30 nm. (b) Raman-spectra of the $SrCO_3$ nanowires. The upper traces show the Raman spectrum of the wire-like product, the lower trace shows a comparison with strontianite reference material.

We assume that the wire-like morphology can be ascribed to the adsorption of the unfolded polyacrylate onto the self-assembled monolayer. Subsequently, the adsorbed bundles of the polymer act as an organic template for the formation of strontianite nanowires.

The formation of the $SrCO_3$ nanowires may be rationalized as follows. In basic solutions (pH 10) polyacrylic acid is completely deprotonated. As a consequence, hydrogen bridge bonds are completely broken, the carboxylate groups act as a complexating agent for the Sr^{2+} ions which in turn bind carbonate ions (which are present at basic pH in sufficient amounts) from the solution und the polymer adopts an unfolded structure, i.e. it acts as a nucleation center. Investigations on the complexating ability of strontium carbonate show that the complexating capability of the polyacrylic acid depends on the solution pH [21]. Polyacrylic acid has a pk_S value of approximately 4.8. Therefore, in acidic solution (pH = 4) the polyacrylic acid will be protonated and it forms a coil-type structure, where the hydrogen bonds of the polyacrylic acid are responsible for the coiled state of the polymer. In our experiments carried out at pH = 10 the polyacrylic acid should be dissociated completely, and it forms a highly negatively charged polyanion and adopts a strand-like shape [21]. It is obvious that the dissociated form displays a higher binding ability for the oppositely charged Sr^{2+} counter cations. Further studies on the conformational changes of polyacrylic acid also indicate a dependence of the polymer particle length on the pH value and the concentration [22]. It has been shown that the particle length is higher at pH = 8-10 compared to pH = 4-5, i.e. the polymer coils open up in basic solution, and rod-like filaments are obtained [22]. This study also indicates that the particle length at low concentrations of polyacrylic acid (10 mg/l, corresponding roughly to the concentration used in our experiments) is definitely higher than the particle length at higher concentrations (1000 mg/l). This very high concentration leads to the formation of a more compact structure by recoiling of the polymer chains.

In our experiment performed at pH=10 we expect the unfolding of the polymer coils resulting in the formation of polyacrylate strands. These polymer strands are adsorbed to the self-assembled monolayer, especially if it is contains carboxylic end-groups. Figure 2.2.3 displays the results of QCM-measurements. At the start of the measurements the aqueous solution contains only Sr^{2+} ions, but no polyacrylate. When polyacrylate was added, a strong mass adsorption (high frequency shift) of polyacrylate onto a carboxylated SAM was observed as shown by the QCM data in Figure 2.2.3a. For the CH_3-terminated SAM the frequency shift is dramatically reduced (see Figure 2.2.3b), which is compatible with a negligibly small mass adsorption of polyacrylate. In both cases the solution was adjusted to pH = 10, and the concentration of polyacrylate (sodium salt, molecular weight: 30.000) in the aqueous solution was about 6.7 mg/l.

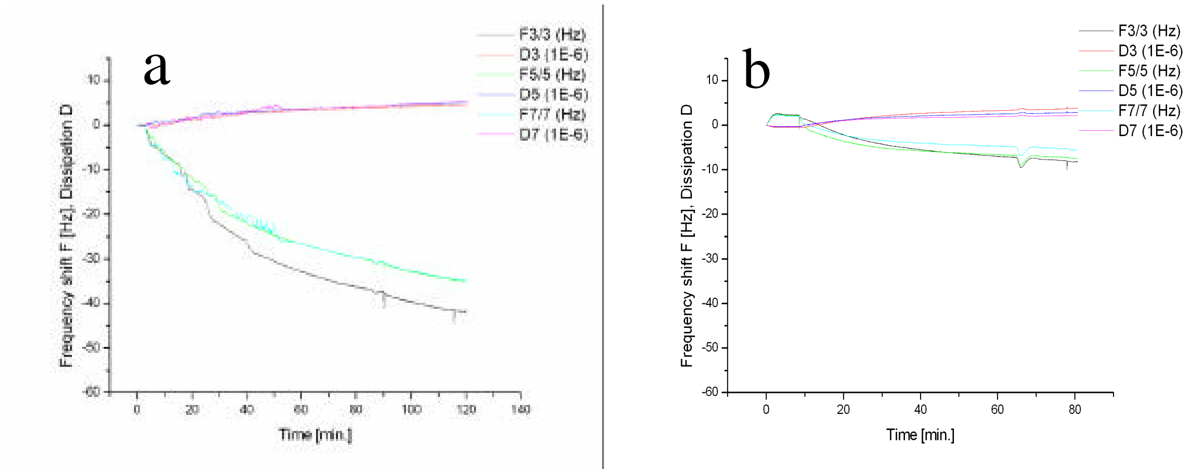

Figure 2.2.3: QCM-measurements of a Sr^{2+} ions containing solution of polyacrylate (c=6.7 mg/l) on a (a) COOH-terminated and (b) a CH$_3$-terminated SAM.

QCM-measurements in a polyacrylate solution without Sr^{2+} ions revealed that there is nearly no adsorption of the polymer onto the surface. This indicates that the adsorption of polyacrylate strands to the COOH-terminated SAM is not due to the direct interaction of the carboxylic groups of the SAM with those of the polymer, but is mediated by the Sr^{2+} ions.

Therefore, the results obtained from the QCM-measurements support our idea that the formation of nanowires must be caused by the formation of polymer bundles on the COOH-terminated SAM. We assume that the adsorbed polyacrylate strands interpenetrate as illustrated in Figure 2.2.4, thereby giving rise to the spaghetti-type morphology of the product. In case of the CH$_3$-terminated SAM nearly no adsorption of the polyacrylate was found for low concentrations (6.7 mg/l) which is reflected in a totally different morphology of the product shown in Figure 2.2.4a and the absence of nanowire-like strontianite. In comparison, Figure 2.2.4b shows the morphology of the product obtained in the absence of polyacrylate on a COOH-terminated surface.

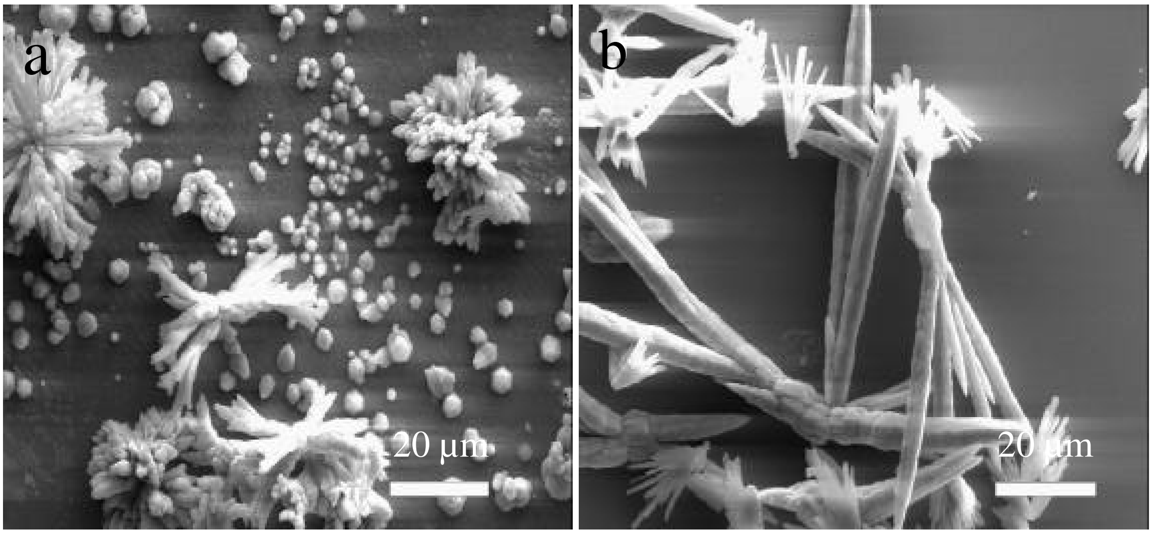

Figure 2.2.4: Crystallization products obtained on a (a) CH_3-terminated surface in the presence of polyacrylate (c = 6.7 mg/l) and (b) on a COOH-functionalized SAM without polyacrylate.

Another clue that the cooperative interaction of the surface and the polyacrylate has a crucial impact on the morphology of the product is provided by the results depicted in Figure 2.2.5, which shows dendritic crystals formed by homogeneous crystallization (which were collected from the bottom of the reaction vessel) in the same experiment that resulted in the heterogeneous formation of nanowires (see Figure 2.2.1) on COOH-terminated SAM in the presence of polyacrylate. The product shown in Figure 2.2.5 was accumulated at the bottom of the crystallization vessel. Obviously nanowire-like crystals are only formed when polyacrylate is adsorbed onto the SAM-surface. We assume that the process of unfolding of the polymer occurs only upon interaction with a highly polar surface. The above results indicate that the adsorption of the polyacrylate onto the SAM is a necessary condition for the formation of products with a nanowire-like morphology.

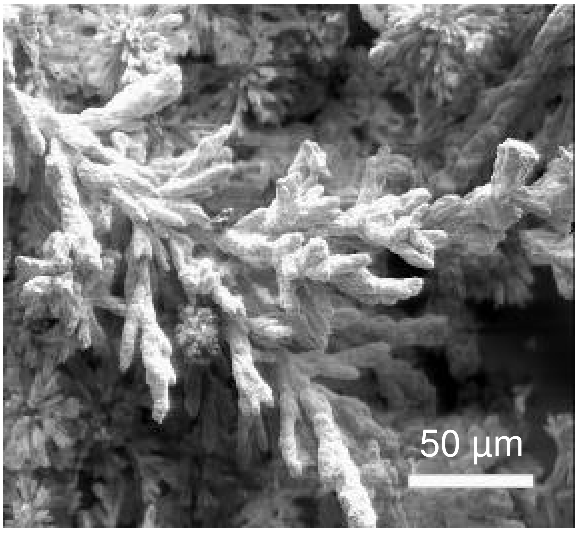

Figure 2.2.5: Dendritic $SrCO_3$ crystals formed by homogeneous nucleation in the presence of polyacrylate. The crystals were collected from the bottom of the crystallization vessel.

In the next step we studied the influence of the polyacrylate concentration on the morphology of the crystallization product. We repeated the experiments described above under the same conditions with respect to the solution pH, crystallization temperature and ion concentrations, but for different concentrations of polyacrylate.

For polyacrylate concentrations at least 4 times higher than those used before (26.7 mg/l) no difference in the morphology of the mineralization product is observed for the COOH-terminated polar surface.

In contrast, the product morphologies are very different for high (> 25 mg/l) and low (< 10 mg/l) polyacrylate concentrations on the CH_3-terminated, unpolar SAMs. Now the products with a nanowire-like morphology were formed for higher (> 25 mg/l) polymer concentrations as well, whereas needle-like aggregates were formed for lower polymer concentrations (Figure 2.2.4a).

Surprisingly, the results of QCM-measurements shown in Figure 2.2.6 for the CH_3-terminated SAM at high polyacrylate concentrations (> 25 mg/l) reveal a significant adsorption of the polymer onto the surface. The magnitude of the adsorption (as indicated by the frequency shift) is observed in the same regime as for the COOH-terminated surface at low polyacrylate concentrations (see Figure 2.2.3a).

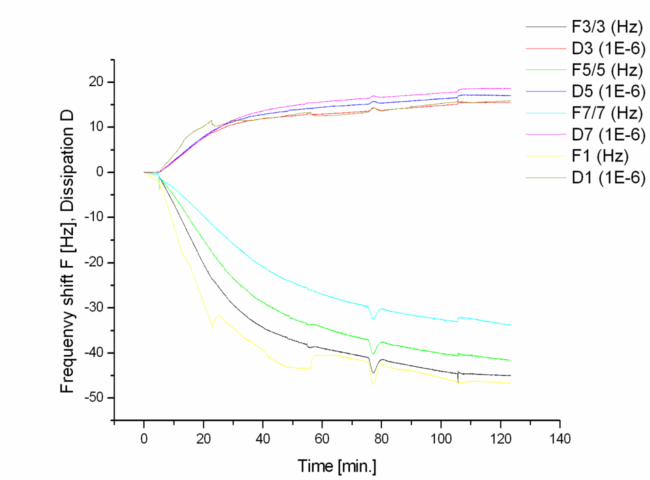

Figure 2.2.6: QCM-measurements of a Sr^{2+} ions containing solution of polyacrylate (c = 26.7 mg/l) on a CH_3-terminated SAM.

A possible explanation is that strontium polyacrylate is known to flocculate for large polymer concentrations. This flocculation by the aggregation of several polymer strands mediated by the Sr^{2+} cations (Figure 2.2.7) leads to a charge compensation of the carboxylate groups and thereby to a reduced polarity - which in turn – facilitates the adsorption of the salt even to unpolar surfaces. The flocculated salt attached to the SAM serves as a template for the formation of strontium carbonate.

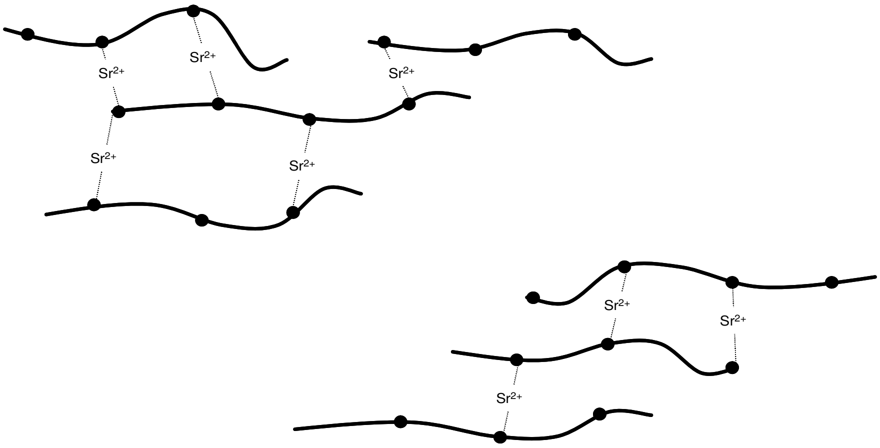

Figure 2.2.7: Formation of aggregates of several PAA strands mediated by Sr^{2+} ions (black spheres = carboxylate groups).

In summary, these results are compatible with a complexation of Sr^{2+} cations and a concomitant aggregation of PAA strands for high PAA concentrations. The formation of $SrCO_3$ wires for small polymer concentrations in the presence of a carboxylate terminated SAM could be explained either by PAA binding to the surface and subsequent $SrCO_3$ crystallization at the PAA template or by the formation of $SrCO_3$/PAA aggregates in solution and subsequent deposition on the SAM.

This model assumes that the presence of the SAM is a necessary condition for the formation of the $SrCO_3$ nanowires. However, we cannot distinguish between the following situation: (i) $SrCO_3$ wires are formed by the nucleation and growth on polyacrylate strands adsorbed to the SAM, and (ii) they are formed by the aggregation of Sr-polyacrylate and primary $SrCO_3$ particles in solution which are subsequently attached to the surface [23]. In order to differentiate between these two mechanisms, samples were taken from the solution 20 min after initializing the mineralization process by the diffusion of carbon dioxide into the solution and investigated by high-resolution transmission electron microscopy (HRTEM). We observed nanometer-sized particles in the solution containing polyacrylate; Figure 2.2.8 shows the image of a well ordered $SrCO_3$ nanocrystal with a diameter of approx. 10 nm and an aspect ratio of 1:5.

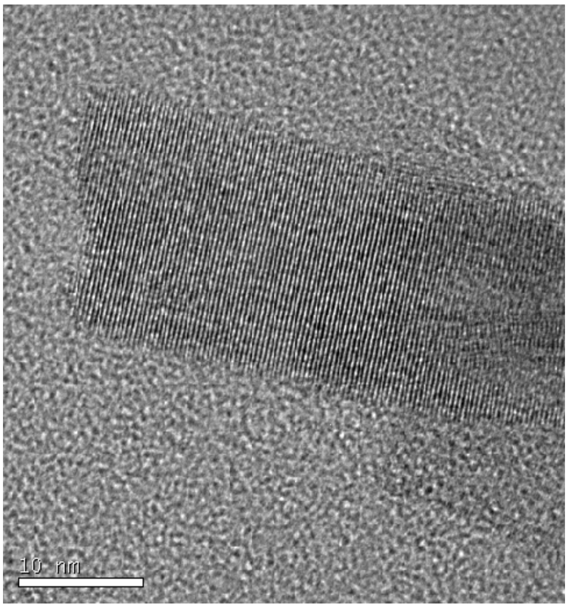

Figure 2.2.8: TEM-graph showing the presence of nanometer-sized $SrCO_3$-particles 20 minutes after starting the mineralization process (scale bar: 10 nm).

Finally, we have to address the question, why the $SrCO_3$ wires have a length of several micrometers, whereas the estimated persistence length of PAA is only approx. 150 nm. As the diameter of a single polymer strand (Ø ˜ 0.5 nm) is small compared to that of a strontianite wire (Ø ˜ 150 nm) as shown in Figure 2.2.1 we must assume that a single wire contains several hundred partially overlapping polymer strands. A possible explanation is as follows: Sr^{2+} cations with a coordination number 8 should be coordinated by at least four carboxylate groups of one or several polymer strands. As a result, the Sr^{2+} cations link several polymer strands by complexation and such an aggregate may easily contain many PAA molecules (Figure 2.2.7). This would be compatible with the observed length of the nanowires.

2.2.3. Conclusion

In conclusion, we were able to demonstrate that $SrCO_3$ nanowires can be synthesized by making use of polymer templates. The template used in this work consists of three components: (i) a self-assembled monolayer, (ii) a dissolved polyelectrolyte and (iii) Sr^{2+} ions in solution. The cooperative interaction of all three components leads to the unusual wire-like morphology of the inorganic mineral $SrCO_3$.

2.2.4. Experimental

Glass slides were cleaned by placing them in a mixture of water, ammonia solution (28-30%) and hydrogen peroxide (5:1:1 by volume). The mixture was heated to 80° C and held at this temperature for 10 min. After cooling to room temperature they were rinsed with water and blown dry with nitrogen. After transferring them to the vacuum chamber of a coating unit (Balzer Baltec), the slides were evaporated with 3 nm of Cr followed by 50 nm of Au. Subsequently, the slides were held for about 24 h in an 1 mM solution of the thiol in toluene or ethanol. After extensive rinsing with toluene or ethanol to remove unbound thiols, the surface was blown dry with nitrogen. These slides were put face down in a crystallization flask containing 300 ml of a 10 mM $SrCl_2$-solution. 2 mg of polyacrylate (sodium-salt, M_W=30.000) was added and the pH-value adjusted to 10 with an aqueous NaOH-solution. The flask was placed in a desiccator and stored for 30 min in order to reach thermal equilibration in a temperature-controlled drying oven (T=45^{O}C). Afterwards the crystallization process was started by placing a petri dish with 6 g $(NH_4)_2CO_3$ at the bottom of the desiccator. The crystallization process was stopped after 24 h, the slides were removed and dried.

For the SEM studies the slides on which the crystallization was carried out were cut in small pieces and fastened with conducting glue on aluminium sample holders. Afterwards they were sputtered with gold before inserting them into the SE microscope. The SE micrographs were acquired on a Zeiss DSM 962 at an acceleration voltage of 15 kV.

Raman micro-spectroscopy was performed with a LabRAM HR800 (Jobin Yvon, Horiba). This confocal Raman system is based on a dispersive spectrometer with notch-filter and focus length of 800 mm. It is equipped with an optical microscope Olympus BX41 and Peltier-cooled CCD-detector (Charge-coupled device). The spectra were excited with a 638,17 Å emission of a He-Ne-laser. The lateral resolution was better than 1,5 µm and the volume resolution was ca. 5 μm^3. The precision of the wave number was 0,5 cm^{-1} and the spectral resolution was about 0,7 cm^{-1}.

For the investigation of the samples using HRTEM (TECNAI F30 with FEG), the substance was suspended in methanol and afterwards several drops of this suspension were placed on a copper grid with a holey carbon film.

AFM height and phase images of the slides were obtained with a Digital Instruments BioScope AFM from Veeco using tapping mode. Imaging was done in air using AFM probes from Nanosensors (type NCH, nominal spring constant 42 N/m, tip radius < 10 nm, resonance frequency 280 kHz).

QCM-D-measurements were performed on a Q-sense D 300 system (Q-sense, Sweden). AT-cut quartz crystals coated with gold films are cleaned prior to use by a treatment with H_2O_2/NH_3/Millipore-water (1:1:5 by volume) by heating up to 80°C for 10min. and subsequent rinsing with Millipore-water and isopropanol. After drying with N_2 the crystals are exposed to a diluted thiol-solution, subsequently rinsed with solvent and dried with N_2. After inserting them into the cell the temperature-controlled measurements are started in a pH-adjusted 0,01 M $SrCl_2$-solution. By exchanging this liquid for a corresponding solution containing polyacrylate the adsorption of the polymer onto the thiol-terminated gold surface is monitored by a decrease of the frequency. Furthermore the energy dissipation D is measured simultaneously. The measurements were performed in a static solution (batch mode).

2.2.5. References

[1] (a) H. A. Lowenstam, S. Weiner (Eds.), On Biomineralisation Oxford University Press, New York, **1989**. (b) S. Mann, J. Webb, R.J.P. Williams, *Biomineralization: Chemical and Biochemical Perspectives*, VCH Publishers, New York, 1989.

[2] S. Mann, *Angew. Chem.* **2000**, *112*, 3532-3548; *Angew. Chem., Int. Ed. Engl.* **2000**, *39*, 3392-3406.

[3] L.A. Estroff, A.D. Hamilton, *Chem. Mater.* **2001**, *13*, 3227-3235.

[4] (a) L. Addadi, S. Weiner, *Angew. Chem.* **1992**, *104*, 159-176; *Angew. Chem. Int. Ed. Engl.* **1992**, 31, 153-170. (b) S. Mann, D.D. Archibald, J.M. Didymus, T. Doughlas, B.R. Heywood, F. Meldrum, N.J. Reeves, *Science* **1993**, *261*, 1286.

[5] L. Addadi, S. Weiner, *Proc. Natl. Acad. Sci. U.S.A.* **1985**, *82*, 4110.

[6] D. Jaquemain, S.G. Wolf, F. Leveiller, M. Deutsch, K. Kjaer, J. Als-Nielsen, M. Lahav, L. Leiserowitz, *Angew. Chem.* **1992**, *104*, 134-158; *Angew. Chem., Int. Ed. Engl.* **1992**, *31*, 130-152.

[7] S. Weiner, L. Addadi, *J. Mater. Chem.* **1997**, *7*, 689-702.

[8] (a) J.M. Marentette, J. Norwig, E. Stöckelmann, W.H. Meyer, G. Wegner, Ad*v. Mater.* **1997**, *9*, 647-650. (b) M. Templin, A. Frank, A. DuChesne, H. Leist, Y.M. Zhang, R. Ulrich, V. Schadler, U. Wiesner, *Science* **1997**, *278*, 1795-1798. (c) J.N. Cha, G.D. Stucky, D.E. Morse, T.J. Deming, *Nature* **2000**, *403*, 289-292. (d) H. Cölfen, L. Qi, *Chem. Eur. J.* **2001**, *7*, 106-116. (e) L. Qi, H. Cölfen, M. Antonietti, M. Li, J.D. Hopwood, A.J. Ashley, S. Mann, *Chem. Eur. J.* **2001**, *7*, 2526-3532.

[9] (a) D. Walsh, S. Mann, *Nature* **1995**, *377*, 320-323. (b) S. Schacht, Q. Huo, I.G. Voigt-Martin, G.D. Stucky, F. Schüth, *Science* **1996**, *273*, 768-771.

[10] D. Walsh and S. Mann, *Adv. Mater.* **1997**, *9*, 658-662.

[11] (a) F. Caruso, R.A. Caruso, H. Möhwaldt, *Science* **1998**, *282*, 1111-1114. (b) B.T. Holland, C.F. Blanford, T. Do, A. Stein, *Chem. Mater.* **1999**, *11*, 795-805.

[12] Y. Levi, S. Albeck, A. Brack, S. Weiner, L. Addadi, *Chem. Eur. J.* **1998**, *4*, 389-396.

[13] (a) D. D. Archibald, S. B. Quadri, B. P. Gaber, *Langmuir* **1996**, *12*, 538-546. (b) J. Küther, W. Tremel, *J. Chem. Soc. Chem. Commun.* **1997**, 2029-2030. (c) J. Küther, R. Seshadri, W. Knoll, W. Tremel, *J. Mater. Chem.* **1998**, *8*, 641-650. (d) J. Küther, G. Nelles, R. Seshadri, M. Schaub, H.-J.Butt, W. Tremel, *Chem. Eur. J.* **1998**, *4*, 1834-1842. (e) J. Küther, R. Seshadri, G. Nelles, H.-J. Butt, W. Knoll, W. Tremel, *Adv. Mater.* **1998**, *10*, 401-404. (f) J. Aizenberg, A. J. Black, G. M. Whitesides, *J. Am. Chem. Soc.* **1999**, *121*, 4500-4509.

[14] (a) J. Küther, R. Seshadri, W. Tremel, *Angew. Chem.* **1998**, *110*, 3196-3199; *Angew. Chem., Int. Ed. Engl.* **1998**, *37*, 3044-3047. (b) J. Küther, R. Seshadri, G. Nelles, W. Assenmacher, H-J. Butt, W. Mader, W. Tremel, *Chem. Mater*. **1999**, *11*, 1317-1325. (c) M. Bartz, J. Küther, G. Nelles, N. Weber, R. Seshadri, W. Tremel, *J. Mater. Chem*. **1999**, *9*, 1121-1125. (d) J.J.J.M. Donners, B.R. Heywood, E.W. Meijer, R.J.M. Nolte, N.A.J.M. Sommerdijk, *Chem. Eur. J.* **2002**, *8*, 2561-2573.

[15] A.M. Belcher, E.E. Gooch, in *Biomineralization, From Biology to Biotechnology and Medical Application*, Hrgb.: E. Bäuerlein, Wiley-VCH, Weinheim, **2000**, 221-249.

[16] M.E. Marsh, in *Biomineralization, From Biology to Biotechnology and Medical Application*, Hrgb.: E. Bäuerlein, Wiley-VCH, Weinheim, **2000**, 251-268.

[17] (a) A. Sugawara, T. Kato, *Chem. Commun.* **2000**, 487. (b) N. Hosoda, T. Kato, *Chem. Mater.* **2001**, *13*, 688.

[18] A. Ulman, *Chem. Rev.* **1996**, *96*, 1533-1554.

[19] J. Küther, M. Bartz, R. Seshadri, G. B. M. Vaughan, W. Tremel, *J. Mater. Chem.* **2001**, *11*, 503-506.

[20] L. Nasdala, A. Banerjee, T. Häger, W. Hofmeister, *Microscopy and Analysis, Europ. ed.* **2001**, *70*, 7-9.

[21] Eui-Deog Hwang, Kwang-Won Lee, Kwang-Ho Choo, Sang-June Choi, Seung-Hyun Kim, Cho-Hee Yoon, Chung-Hak Lee, *Desalination* **2002**, *147*, 289-294.

[22] H. Hoffmann, M. L. T. Liveri, F. P. Cavasino, *J. Chem. Soc., Faraday Trans.* **1997**, *93*, 3161-3165.

[23] H. Cölfen, S. Mann, *Angew. Chem.* **2003**, *115*, 2452-2468.

2.3. Controlled Crystallization of $CaCO_3$ on Hyperbranched Polyglycerol Adsorbed to a SAM

2.3.1. Introduction

Crystallization processes in biological systems are highly complex and provide an intriguing field of activity for scientists deriving from different backgrounds. Living organisms possess the ability to control the precipitation of minerals such as calcium carbonate or calcium phosphate with respect to the nucleation, growth, morphology and polymorphic structure. Gaining deeper insight into the processes proceeding at the molecular level could contribute to a better understanding of the formation of these inorganic materials and is therefore of fundamental importance. The formation process takes place under physiological conditions and results in highly complex architectural structures and specific mechanical properties of the minerals, such as an enhancement of the fracture resistance or the reduction of brittleness, i.e. properties that are very different and often advantageous compared to those of their synthetic counterparts [1,2].

It is known that biological macromolecules play a key role in the mineralization process and are intimately associated with the growing mineral. The nucleation process is believed to be initiated at the organic-inorganic interface, the organic component providing a nucleating matrix for the inorganic part. Active biomacromolecules can be divided into two classes, namely (i) soluble, hydrophilic polymers (mostly proteins/glycoproteins or polysaccharides) and (ii) insoluble matrices such as collagen and chitin serving as a template for the crystallization process [2,3]. The soluble macromolecules are able to interact either with ions in solution and the ions of a crystal plane [4,5] or with solid matrices [3]. Especially the nacreous layer of the abalone shell, *Haliotis Rufescens* [6], was and still is subject of detailed investigation. From this example it is known that hydrophilic, anionically charged, soluble macromolecules adsorb onto a three-dimensional scaffold consisting of insoluble macromolecules and thereby exert a major impact on the nucleation process.

Because of the complex interaction between soluble and insoluble macromolecules it is difficult to mimic biomineralization processes in model experiments. Thus, to date most studies focused almost exclusively on the nucleating matrix, where Langmuir monolayers of various functionality [7], proteins [2], polymer dispersions and synthetic block copolymers [8] micellar solutions [9], self-assembled monolayers (SAMs) [10] or colloids and dendritic macromolecules have been employed as synthetic models of the biomacromolecules [11].

Based on the assumption that a cooperative interaction between an insoluble matrix and macromolecules in solution is a significant step in the mineralization process, the influence of a linear chain polyelectrolyte on the crystallization of calcium carbonate on SAMs was studied [12]. In these experiments hierarchically ordered mineral structures were formed [12]. These findings raised the question concerning the effect of dendritic or hyperbranched polymers on the mineralization process. Hyperbranched polymers, randomly cascade branched polymers, have become an important class of compounds due to the combination of their ease of preparation and their unique properties, but also owing to the recent development of controlled syntheses [13]. Such polymers are nowadays attractive for numerous applications that require high functionality in combination with compact molecular shape.

To date next to nothing is known concerning the influence of functionality and branched polymer architecture on the crystallization of inorganic materials. Several years ago, Westbroeck et al. reported on the formation of calcite in the presence of carboxylated hyperbranched polyphenylene, which represents a rigid organic strucure [14].

Herein we present the first results of a detailed study of the crystallization of calcium carbonate, using the cooperation of dissolved flexible and well-defined hyperbranched polyether polyol, namely hyperbranched polyglycerol (Figure 2.3.1a), with an organic monolayer self-assembled on a flat gold surface (Figure 2.3.1b).

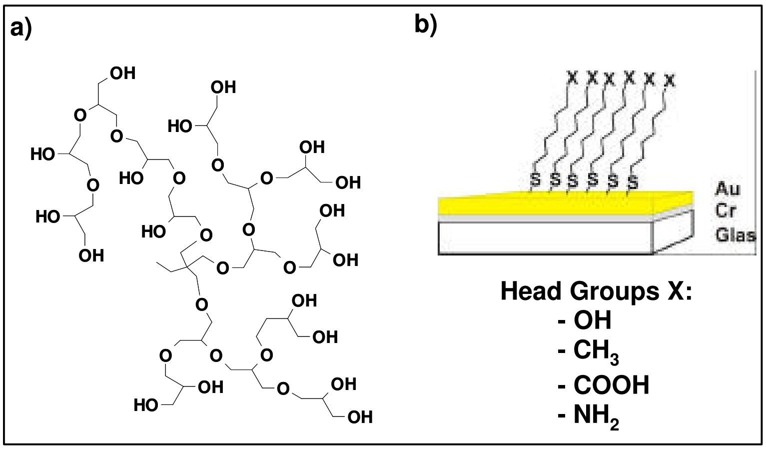

Figure 2.3.1: a) Structure of the soluble matrix consisting of hyperbranched polyglycerol, b) self-assembled monolayer with X as terminating group.

2.3.2. Results and discussion

Figure 2.3.2 shows the $CaCO_3$ crystals formed on a CH_3-terminated (hexadecanethiol covered) SAM). The precipitate on the CH_3 terminated surface is mainly composed of calcite rhombs, as well as florets of vaterite and bundles of aragonite needles, i.e., a mixture of various polymorphs is obtained.

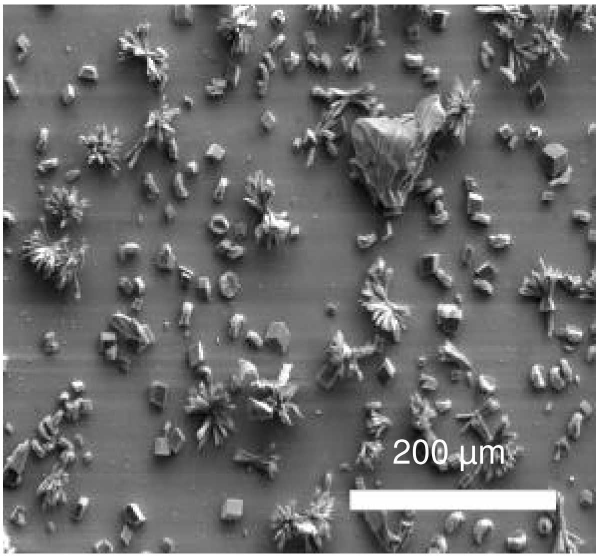

Figure 2.3.2: Scanning electron micrographs of $CaCO_3$ crystals on a CH_3-terminated SAM surface.

Figure 2.3.3a displays the crystallization products on a polar, OH-terminated surface (covered with mercaptoundecanol). On the OH-terminated SAM surface predominantly calcite was obtained. In previous studies it was shown that the selectivity regarding the preferential formation of a certain crystal phase is determined by temperature, chain length and head groups of the ? -functional thiols as well as roughness of the surface [10b-e].

Performing the mineralization process under the same conditions as used for the sample shown in Figure 2.3.2, but adding hyperbranched polyglycerol (c = 0.33 mg/ml, M_n = 5000 g/mol) to the $CaCl_2$ solution prior to the crystallization process resulted in a completely different crystallization product. In this case the precipitate is nearly exclusively aragonite, as it is obvious from the bundles of needle-like crystals and it was evidenced by X-ray diffraction (Figure 2.3.3b).

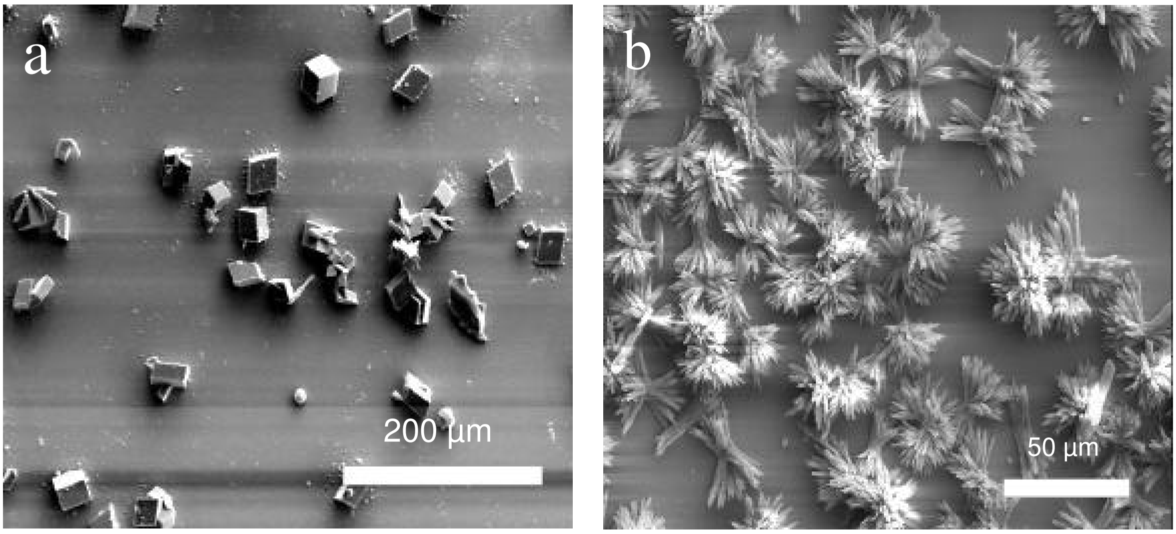

Figure 2.3.3: (a) SE-micrographs of $CaCO_3$ crystals on an OH-terminated SAM surface and (b) of aragonite on a CH_3-terminated SAM with adsorbed *hb*-polyglycerol (M_n = 5000 g/mol).

In order to elucidate the influence of the molecular weight, a series of experiments has been performed using hyperbranched polyglycerols of various molecular weights (500; 2000; 5000; 8000 g/mol). In all cases, the same concentration of *hb*-polyglycerol (0.33 mg/ml) for the four different molecular weights was applied. The highest yield of aragonite was obtained for the molecular weights in the range of 500 to 5000 g/mol. In the case of the *hb*-polyglycerol with a molecular weight of 8000 g/mol no pure aragonite phase was obtained.

The use of various concentrations of *hb*-polyglycerol with a molecular weight of 2.000 g/mol in the mineralization process revealed that a minimum concentration of about 0.17 mg/ml aqueous $CaCl_2$-solution is required to obtain an approximately pure phase of aragonite crystals.

The hyperbranched polyglycerol samples employed exhibit low polydispersity ($M_w/M_n < 1.5$), combining randomly branched structure and high functionality. In a series of measurements that are not detailed here, it has been shown that unmodified polyglycerol possesses an intrinsically amphiphilic structure, showing a critical micelle concentration (cmc) [15]. This is due to the fact that the flexible structure of *hb*-polyglycerol consists of a hydroxyl-rich polar periphery and a rather apolar core, which permits the formation of micellar aggregates in solution as well as the interaction with surfaces

On the basis of the cmc-data, it is reasonable to explain our findings using the following model. In the presence of the hydrophobic SAM surface (CH_3-termination) the hydrophobic part (core region) of polyglycerol adsorbs at the hydrophobic CH_3-terminated surface of the SAM. In contrast, the hydrophilic part of the polyglycerol molecule, i.e., the hydroxyl groups are oriented towards the solution. In this manner, the hydrophobic SAM surface turns hydrophilic because of the OH-groups of polyglycerol. It is important to emphasize that due to the randomly branched polyglycerol topology, the multiple hydroxyl groups will also be present in a random arrangement on the SAM surface. Applying quartz-crystal microbalance (QCM) measurements, it was confirmed that *hb*-polyglycerol is adsorbed onto the SAM-surface. QCM-measurements have been performed for different molecular weights of the hyperbranched polyglycerol. Figure 2.3.4 shows the progression of the resonance frequency F and the energy dissipation D before ($t < 88$ min.) and after ($t > 88$ min.) exchanging an aqueous $CaCl_2$-solution for the corresponding solution, but containing hyperbranched polyglycerol (molecular weight of 5000 g/mol). The decay of the frequency at 88 min. is unambiguously ascribed to the adsorption of *hb*-polyglycerol onto the CH_3-terminated SAM. A mass uptake onto the SAM surface is generally connected with a decreasing frequency. The progression of the energy dissipation D can be attributed to the viscoelastic properties of the film, and it is of minor interest in the present context.

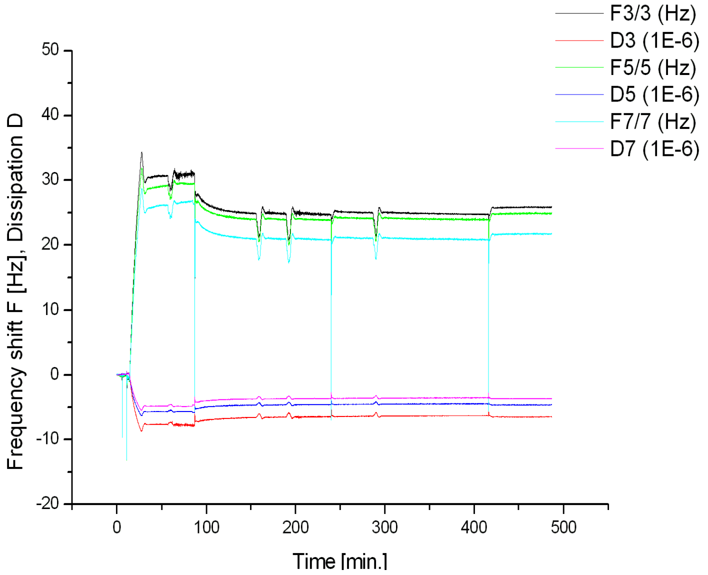

Figure 2.3.4: Progression of the frequency and dissipation before and after the addition of *hb*-polyglycerol (M_n = 5000 g/mol).

Comparative measurements of the contact angle of a CH_3-terminated surface and CH_3-terminated surface with adsorbed *hb*-polyglycerol show a decrease of the contact angle of the latter sample of about 5^0. This translates to increasing hydrophilicity, which can be attributed to the OH-groups of polyglycerol.

Another clue that the specific highly branched structure of the *hb*-polyglycerol is of great importance for the exclusive formation of aragonite is the result of a control crystallization experiment using a soluble linear macromolecule, poly(vinylalcohol) (PVA, M_W 9,000 g/mol). The crystallization products obtained on a CH_3-terminated surface under the same conditions as applied for the crystallization process in the presence of *hb*-polyglycerol are depicted in Figure 2.3.5. These are mainly composed of calcite rhombs and a small amount of aragonite and vaterite.

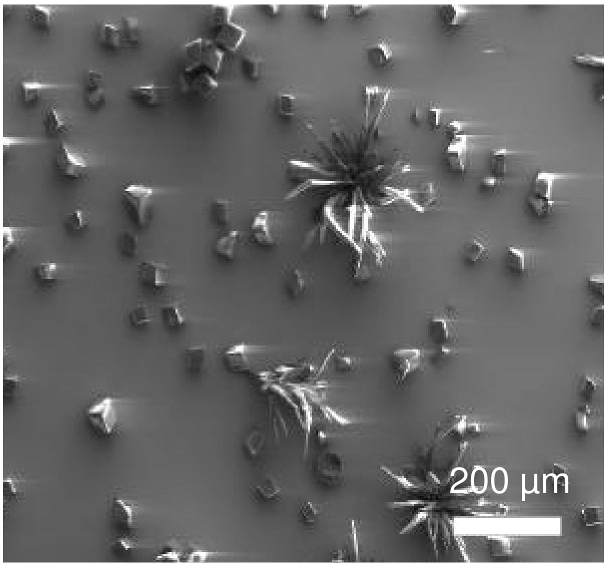

Figure 2.3.5: Crystallization products on a CH_3-terminated SAM in the presence of PVA (M_n = 9000g/mol).

It is an intriguing result that aragonite is formed on a CH_3-terminated SAM after hydrophilic modification due to the OH-groups of *hb*-polyglycerol, but no aragonite is precipitated on an OH-terminated SAM (Figure 2.3.3a). Several previous studies have shown that the phase selection of aragonite does not solely depend on the functionality of the surface, but also strongly depends on the surface roughness [10c,d]: aragonite formation is favored on poorly crystallized surfaces with a high roughness. In contrast, highly ordered surfaces with hexagonal symmetry appear to promote the nucleation of calcite and to inhibit the crystallization of aragonite. The CH_3-terminated SAM represents a crystalline surface, whereas the polar surface obtained after adsorption of *hb*-polyglycerol is rough and poorly organized, the surface roughness being comparable to that of surface with gold colloids tethered to it [10e]. The loss of order can be ascribed to the randomly branched, flexible and amorphous structure of hyperbranched polyglycerols.

Having considered the nucleation on the Pgly-surface, it is an intriguing issue, whether concurrent homogeneous crystallization in solution also leads to the formation of aragonite. However, the surface clearly has a crucial impact on the polymorphic structure, as demonstrated by the results shown in Figure 2.3.6**.** Whereas calcite crystals are formed exclusively by homogeneous nucleation in solution, the heterogeneous reaction on CH_3-terminated SAM in the presence of *hb*-polyglycerol in the same experiment leads to the exclusive formation of aragonite (see Figure 2.3.3b). The product shown in Figure 2.3.6 was obtained from the bottom of the crystallization vessel

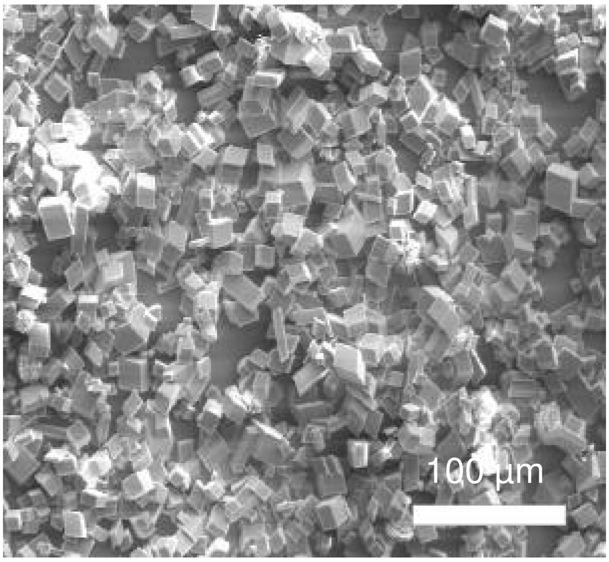

Figure 2.3.6: Crystals obtained from the bottom of a crystallization vessel containing *hb*-polyglycerol (M_n = 5000 g/mol).

From these results it appears that there is an intricate interplay between the polarity of the surface and the hyperbranched additive. This is further confirmed by experiments based on COOH terminated SAMs in the presence of *hb*-polyglycerol (Figure 2.3.7). Again, QCM-measurements evidence that *hb*-polyglycerol is adsorbed onto the surface. We assume that in this case the hydrophilic part of the *hb*-polyglycerol is adsorbed to the hydrophilic COOH-functionality and hence the hydrophobic part is oriented towards the solution, i.e., the composite surface becomes hydrophobic. The predominant crystalline phase in this experiment is calcite, and only a small amount of aragonite is precipitated. Earlier studies on SAMs have shown that calcite formation with lower nucleation densities is preferred [10c]. Our present results confirm the proposed molecular mechanism based on the surface roughness and functionality.

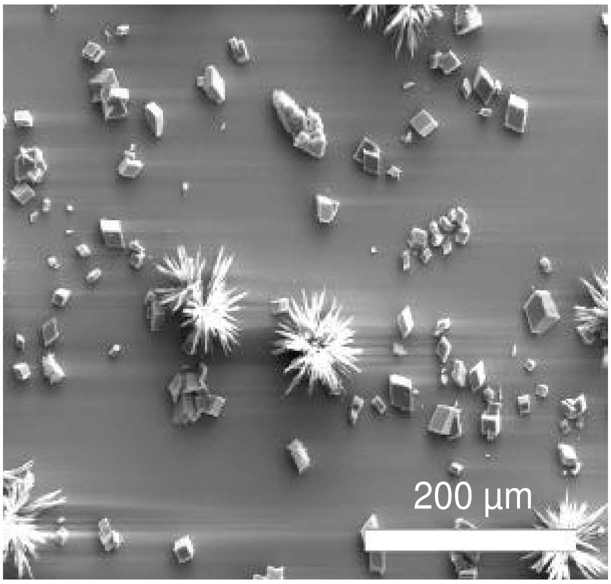

Figure 2.3.7: Crystals formed on a COOH-terminated SAM with adsorbed hb- polyglycerol (M_n = 5000 g/mol).

2.3.3. Conclusion

The mineralization of calcium carbonate in the presence of *hb*-polyglycerol of different molecular weights (from 500 to 8000 g/mol) adsorbed onto a CH_3-terminated SAM leads to the formation of hydrophilic, OH terminated surfaces with a high surface roughness. As a result, the crystallization of aragonite is highly preferred. The adsorption of the *hb*-polyglycerol to the surface was monitored and confirmed by QCM-measurements. These results are in good agreement with those of previous studies concerning the conditions for the controlled crystallization of calcium carbonate. Reference experiments in the presence of poly(vinylalcohol) instead of *hb*-polyglycerol and without *hb*-polyglycerol indicate the effect of the dendritic structure of the *hb*-polyglycerol for the surface properties (roughness) which lead to the controlled crystallization of aragonite.

Due to their convenient availability (vs. tedious multistep syntheses of dendrimers), the good solubility in aqueous solutions, the flexible structure and high functionality, *hb*-polyglycerols represent appropriate model systems (in combination with SAMs) to study biomineralization processes. Detailed studies on carboxylated *hb*-polyglycerols as well as other amphiphilic hyperbranched structures are in progress.

2.3.4. Experimental

Hyperbranched polyglycerols (*hb*-polyglycerol) of different molecular weights have been prepared according to previously published procedures [16]. Poly(vinylalcohol) was purchased from Aldrich. Suprapur and 1-hexadecanethiol (p.a.) were purchased from Merck and used as received. Mercaptoundecanol and ?-mercaptoundecanoic acid were prepared and purified according to literature methods [17]. All experiments were performed with deionized water (Millipore).

Glass slides were cleaned by placing them in a mixture of water, ammonia solution (28-30%) and hydrogen peroxide (5:1:1 by volume). The mixture was heated to 80°C and held at this temperature for 10 min. After cooling to room temperature the slides were rinsed with water and blown dry with nitrogen. After transfer to the vacuum chamber of a coating unit (Balzer Baltec), the slides were coated with 3 nm of Cr, followed by 50 nm of Au. The slides were then held in a 1 mM solution of the thiol in toluene or ethanol for about 24 h. After extensive rinsing with toluene or ethanol to remove unbound thiols, the surface was blown dry with nitrogen. These slides were placed face-down in a crystallization flask, containing 300 ml of a 10 mM $CaCl_2$-solution. 100 mg of *hb*-polyglycerol or poly(vinylalcohol), respectively, was added and the pH-value adjusted to 10 with an aqueous NaOH-solution. The flask was placed in a desiccator and stored for thermal equilibration for 45 min. in a temperature-controlled oven (45^{O}C). Subsequently, the crystallization process was started by placing a petri-dish with 7 g $(NH_4)_2CO_3$ at the bottom of the desiccator. The crystallization process was stopped after 24 h. The slides were removed and dried.

For SEM the slides on which the crystallization was carried out were cut in small pieces and fastened with conducting glue on aluminium sample holders. After sputtering with gold they were inserted into the SE microscope. The measurements were performed on a Zeiss DSM 962 at an acceleration voltage of 15 kV.

QCM-D-measurements were performed on a Q-sense D 300 system (Q-sense, Sweden). AT-cut quartz crystals coated with gold films are cleaned prior to use by a treatment with H_2O_2/NH_3/Millipore-water (1:1:5 by volume, 10min. 80°C) and subsequent rinsing with Millipore-water and isopropanol. After drying with N_2, the crystals were exposed to a diluted thiol-solution, subsequently rinsed with solvent and dried with N_2. After inserting them into the cell the temperature-controlled measurements were started in a pH-adjusted 0,01 M $CaCl_2$-solution. By exchanging this liquid for a corresponding solution containing *hb*-polyglycerol the adsorption of the polymer onto the thiol-terminated gold surface is monitored by a decrease of the frequency. Furthermore the energy dissipation D is measured simultaneously. The measurements were performed in a static solution (batch mode).

2.3.5. References

[1] (a) H. A. Lowenstam, S. Weiner (Eds.), On Biomineralisation Oxford University Press, New York, **1989**. (b) S. Mann, J. Webb, R.J.P. Williams, *Biomineralization: Chemical and Biochemical Perspectives*, VCH Publishers, New York, **1989**.

[2] S. Weiner, L.Addadi, *J. Mater. Chem.* **1997**, *7*, 689-702.

[3] T. Kato, A. Sugawara, N. Hosoda, *Adv. Mater.* **2002**, *14*, 869.

[4] S. Albeck, J. Aizenberg, L. Addadi, S. Weiner, *J. Am. Chem. Soc.* **1993**, *115*, 11691.

[5] J. Aizenberg, J. Hanson, T. F. Koetzle, S. Weiner, L. Addadi, *J. Am. Chem. Soc.* **1997**, *119*, 881.

[6] E. Bäuerlein, *Biomineralization*, Wiley-VCH, Weinheim, **2000.**

[7] D. Jaquemain, S.G. Wolf, F. Leveiller, M. Deutsch, K. Kjaer, J. Als-Nielsen, M. Lahav, L. Leiserowitz, *Angew. Chem*. **1992**, *104*, 134-158; *Angew. Chem., Int. Ed. Engl.* **1992**, *31*, 130-152.

[8] (a) J.M. Marentette, J. Norwig, E. Stöckelmann, W.H. Meyer, G. Wegner, *Adv. Mater.* **1997**, *9*, 647-650. (b) M. Templin, A. Frank, A. DuChesne, H. Leist, Y.M. Zhang, R. Ulrich, V. Schadler, U. Wiesner, *Science* **1997**, *278*, 1795-1798. (c) J.N. Cha, G.D. Stucky, D.E. Morse, T.J. Deming, *Nature* **2000**, *403*, 289-292. (d) H. Cölfen, L. Qi, *Chem. Eur. J.* **2001**, *7*, 106-116. (e) L. Qi, H. Cölfen, M. Antonietti, M. Li, J.D. Hopwood, A.J. Ashley, S. Mann, *Chem. Eur. J.* **2001**, *7*, 3526-3532.

[9] D. Walsh and S. Mann, *Adv. Mater.* **1997**, *9*, 658-662.

[10] (a) D. D. Archibald, S. B. Quadri, B. P. Gaber, *Langmuir* **1996**, *12*, 538-546. (b) J. Küther, W. Tremel, *J. Chem. Soc. Chem. Commun.* **1997**, 2029-2030. (c) J. Küther, R. Seshadri, W. Knoll, W. Tremel, *J. Mater. Chem.* **1998**, *8*, 641-650. (d) J. Küther, R. Seshadri, G. Nelles, H.-J. Butt, W. Knoll, W. Tremel, *Adv. Mater.* **1998**, *10*, 401-404. (e) J. Küther, G. Nelles, R. Seshadri, M. Schaub, H.-J.Butt, W. Tremel, *Chem. Eur. J.* **1998**, *4*, 1834-1842. (f) J. Küther, R. Seshadri, G. Nelles, H.-J. Butt, W. Knoll, W. Tremel, *Adv. Mater.* **1998**, *10*, 401-404. (g) J. Aizenberg, A. J. Black, G. M. Whitesides, *J. Am. Chem. Soc.* **1999**, *121*, 4500-4509.

[11] (a) J. Küther, R. Seshadri, W. Tremel, *Angew. Chem.* **1998**, *110*, 3196-3199; *Angew. Chem., Int. Ed. Engl.* **1998**, *37*, 3044-3047. (b) J. Küther, R. Seshadri, G. Nelles, W. Assenmacher, H-J. Butt, W. Mader, W. Tremel, *Chem. Mater.* **1999**, *11*, 1317-1325. (c) M. Bartz, J. Küther, G. Nelles, N. Weber, R. Seshadri, W. Tremel, *J. Mater. Chem.* **1999**, *9*, 1121-1125. (d) J.J.M. Donners, B.R. Heywood, E.W. Meijer, R.J.M. Nolte, N.A.J.M. Sommerdijk, *Chem. Eur. J.* **2002**, *8*, 2561-2573. (e) K. Naka, Y. Tanaka, Y. Chujo, Y. Ito, *Chem. Commun.* **1999**, 1931.

[12] M.Balz, H. A. Therese, J. Li, J. S. Gutmann, M. Kappl, L. Nasdala, W. Hofmeister H.-J. Butt, W. Tremel, *Adv. Mater.* **2003**, submitted.

[13] (a) M. Jikei, M.-a. Kakimoto, *Prog. Polym. Sci.* **2001**, *26*, 1233. (b) C. Gao, D. Yan, *Prog. Polym. Sci.* **2004**, *29*, 183.

[14] J.M. Didymus, P. Oliver, S. Mann, A.L. Devries, P.V. Hauschka, P. Westbroeck, *J. Chem. Soc. Faraday Trans.* **1993**, *89*, 2891.

[15] V. Istratov, H. Kautz, Y.-K. Kim, R. Schubert, H. Frey, *Tetrahedron* **2003**, *59*, 4017.

[16] A. Sunder, R. Hanselmann, H. Frey, R. Mülhaupt, *Macromolecules* **1999**, *32*, 4240. (b) A. Sunder, R. Mülhaupt, R. Haag, H. Frey, *Adv. Mater.* **2000**, *12*, 235.

[17] H. Wolf, Ph.D. thesis, University of Mainz, **1995.**

2.4. Crystallization of Vaterite Hemispheres on Carboxymethyl Cellulose Adsorbed to a SAM

2.4.1. Introduction

Living systems are able to exert a considerable control onto the crystallization process of inorganic minerals such as calcium carbonate or calcium phosphate. This control leads to a certain polymorphic structure, size and morphology as well as a specific function of the inorganic mineral. The formation of these inorganic minerals is closely connected to biomacromolecules such as proteins and polysaccharides. The process of formation takes place at an organic-inorganic interface [1,2,3]. The mimicking of these biomineralization processes has been accomplished in the past years using Langmuir monolayers [4], protein-coated substrates [5], polymers and polymer dispersions [6], micellar media [7], biomacromolecules such as chitin and cellulose [8], and self-assembled monolayers (SAMs) [9] as substrates or templates for the crystallization of inorganic minerals.

Our previous work was focused on the crystallization of calcium carbonate on SAMs composed of alkylthiols on a gold substrate. The impact of different chain lengths and head-groups of the alkylthiol onto the polymorphic structure of the growing calcium carbonate phase was investigated [9b-e].

In this work we want to include so a soluble macromolecule in the models of mineralization. By the combination of a self-assembled monolayer and a soluble biomolecule we try to approach to natural systems that are composed of a solid matrix and macromolecules such as glycoproteins.

To study heterogeneous nucleation at an organic-inorganic boundary we use a model system that consists of non-polar (-CH_3) and highly polar (-COOH) functionalized thiols that self-assemble on a gold surface forming a highly ordered monolayer [10] and a dissolved macromolecule, namely carboxymethyl cellulose (sodium salt). The crystallization process is induced by the diffusion of carbon dioxide into an aqueous solution of calcium chloride containing the carboxymethyl cellulose (M_W = 250.000 g/mol).

Cellulose is insoluble in water. The formation of carboxymethyl cellulose (sodium salt) is achieved by the etherification of OH-groups of the cellulose macromolecule. The introduction of carboxylated groups leads to a good solubility in water.

2.4.2. Results and discussion

Figure 2.4.1 shows the calcium carbonate crystals formed on a COOH-terminated SAM surface in the presence of carboxymethyl cellulose. The precipitate is mainly composed of hemispherically shaped crystals. Their sizes are in the range of about 20 to 50 µm.

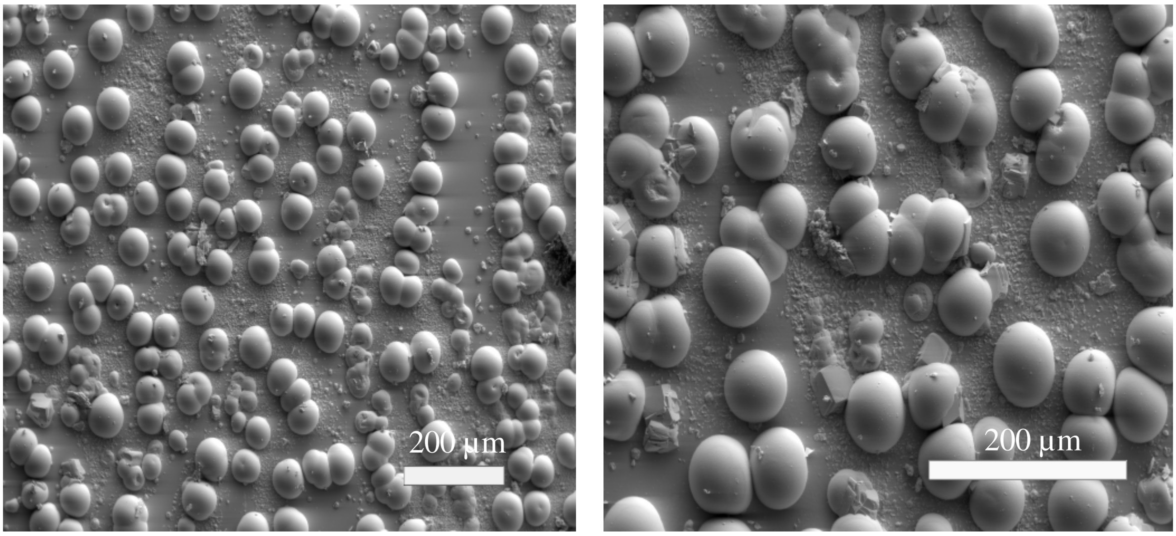

Figure 2.4.1: Calcium carbonate crystals formed on a COOH-terminated SAM in the presence of carboxymethyl cellulose.

To identify the phase of the crystals obtained in Figure 2.4.1, micro-Raman spectroscopy [11] was used and the polymorphic structure could be identified unambiguously as vaterite (hexagonal $CaCO_3$). By micro-Raman spectroscopy it is possible, to distinguish and positionally resolve µm-sized aggregates of the $CaCO_3$ minerals calcite (trigonal), aragonite (rhombic) and vaterite. A typical Raman spectrum of the hemispherical crystals is depicted in Figure 2.4.2. Furthermore, the presence of vaterite was confirmed independently by X-ray diffraction.

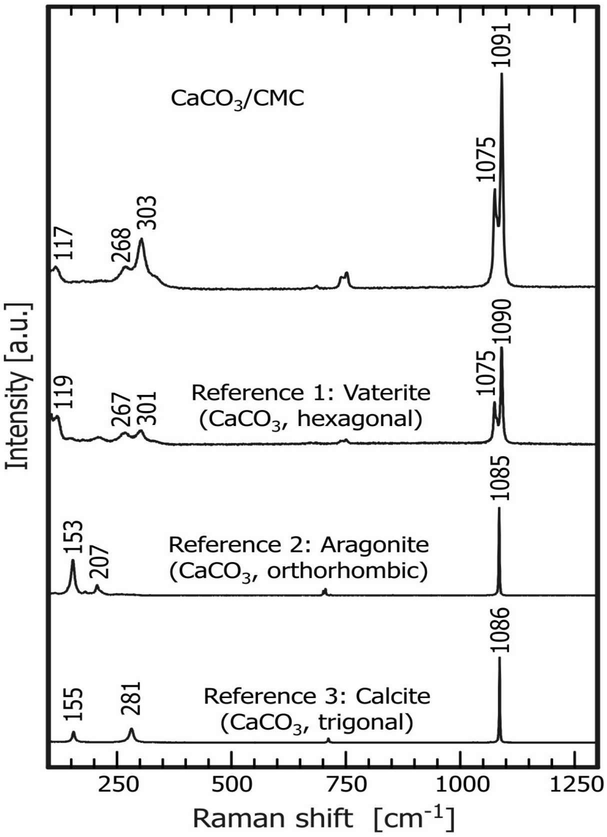

Figure 2.4.2: Micro-Raman-spectra of the hemispherical crystals of Figure 2.4.1.

The preferred precipitation of hemispherical crystals is obtained only under certain conditions including the termination of the thiol that forms the self-assembled monolayer (COOH-termination), pH-adjustment of the aqueous solution containing the Ca^{2+} ions and the carboxymethyl cellulose, and a crystallization temperature of 12^{O} or 25 ^{O}C, respectively.

The importance of a COOH-terminated SAM surface for the controlled precipitation of the hemispherically shaped vaterite crystals of Figure 2.4.1 becomes evident by the crystallization products depicted in Figure 2.4.3. In this case we employed a patterned surface for the crystallization of calcium carbonate in the presence of carboxymethyl cellulose. The patterning was obtained using the PDMS (polydimethylsiloxane) stamp technique [12] combined with the self assembly method. By using this technique the COOH-terminated thiol could be stamped onto the gold surface. Afterwards the CH_3-functionalized thiol was spontaneously assembled from a toluene solution.

Performing the mineralization process in this way, hemispherical vaterite crystals are obtained in the area that is covered with the COOH-terminated SAM, whereas calcite crystals are deposited onto the CH_3-terminated SAM surface. This finding indicates that the phase of the mineralization product does not only depends on the presence of the macromolecule but also on the functionality of the SAM.

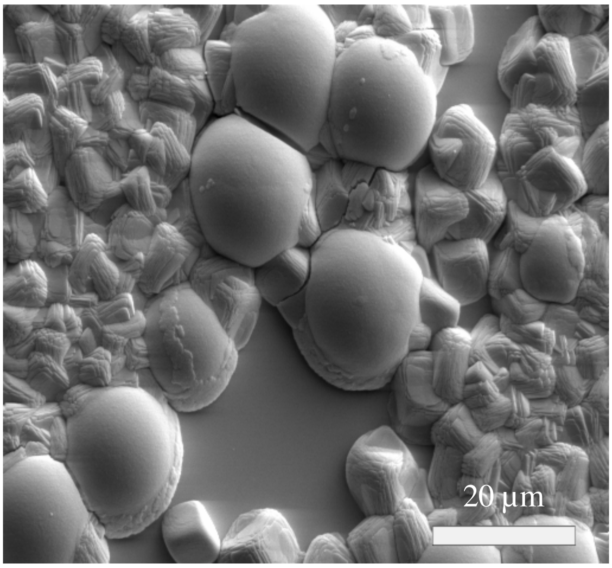

Figure 2.4.3: Vaterite and calcite crystals on a COOH/CH_3 stamped surface.

Mineralization experiments performed under the same conditions as used for the sample of Figure 2.4.1, but in the absence of carboxymethyl cellulose resulted in completely different crystallization products that are predominantly composed of calcite.

To find a plausible interpretation of the experimental results one has to account for the interaction between the polymer and the SAM surface. For this, measurements with a quartz crystal microbalance (QCM) were performed. Replacing an aqueous solution of pH 10 containing Ca^{2+}-ions after a few minutes with the same solution, but containing carboxymethyl cellulose resulted in a strong frequency shift of more than 20 Hz for the COOH-terminated SAM surface (Figure 2.4.4a) that can be ascribed to a significant adsorption of carboxymethyl cellulose onto the highly polar COOH-terminated SAM.

In contrast, corresponding measurements performed on a CH_3-terminated SAM surface resulted in a frequency shift of only 1 Hz. This indicates that nearly no attachment of the polymer was obtained on the non-polar surface (Figure 2.4.4b).

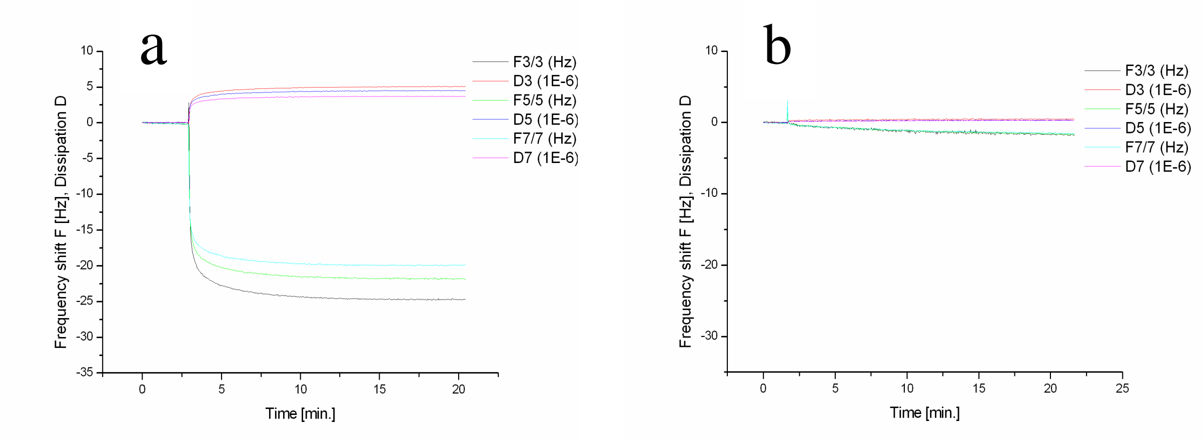

Figure 2.4.4: QCM-measurement of a solution containing carboxymethyl cellulose indicating (a) the adsorption of the polymer onto a COOH terminated SAM and (b) the absence of adsorption on a CH_3-functionalized surface.

We assume that the carboxymethyl cellulose is adsorbed to the polar surface due to its carboxylate groups. From previous studies on the interaction of a SAM surface and carboxylate groups bearing polymers such as polyacrylate we know that the attachment of the polyacrylate onto the SAM only takes place if a carboxylate terminated monolayer is present. However nearly no adsorption of the polyacrylate is observed onto a CH_3-functionalized SAM [13]. Furthermore it was found that the attachment between the carboxylate groups of the SAM surface and those of the polymer was mediated by the Ca^{2+} ions in solution [13].

Another clue that the COOH-terminated SAM surface in cooperation with the carboxymethyl cellulose determines the polymorphic structure and morphology of the crystallization product is provided by the results depicted in Figure 2.4.5 which shows spherical crystals formed by homogeneous crystallization in the experiment that resulted in the heterogeneous formation of vaterite on the COOH-terminated SAM in the presence of carboxymethyl cellulose (see Figure 2.4.1). The crystals shown in Figure 2.4.5 were accumulated at the bottom of the crystallization vessel. The diameter of these spheres lies in the range of about 1 to 10 µm.

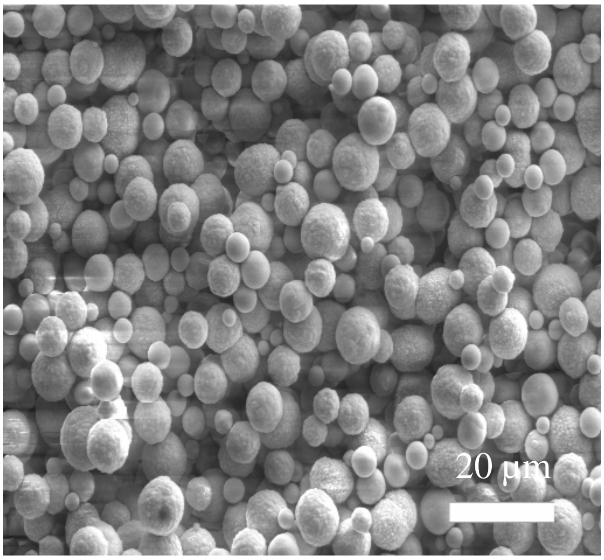

Figure 2.4.5: Crystals obtained from the bottom of a crystallization vessel containing carboxymethyl cellulose.

The vaterite hemispheres of Figure 2.4.1 are obtained at concentrations of the carboxymethyl cellulose ranging from 0,033 to 0,17 mg/ml. For crystallization temperatures of about 25^0C the lower concentration is sufficient, whereas for crystallization temperatures of about 12^0C higher concentrations are necessary to obtain the vaterite hemispheres on the COOH-terminated SAM surface. Under the afore-mentioned conditions calcite is the predominant phase on the CH_3-terminated surface.

2.4.3. Conclusion

In this study it was shown that the soluble carboxymethyl cellulose is adsorbed onto a COOH-functionalized self-assembled monolayer. The crystallization process of calcium carbonate on the organic-inorganic interface results in the precipitation of hemispherically shaped vaterite which represents a rather uncommon morphology of vaterite. Totally different crystallization products are obtained on CH_3-terminated SAMs in the presence of carboxymethyl cellulose and on COOH-functionalized SAMs in the absence of the macromolecule. These results clearly indicate the impact of the interacting SAM surface and soluble polymer, i.e. the organic-inorganic boundary onto the polymorphic structure of the crystallization products.

2.4.4. Experimental

Glass slides were cleaned by placing them in a mixture of water, ammonia solution (28-30%) and hydrogen peroxide (5:1:1 by volume). The mixture was heated to 80°C and held at this temperature for 10 min. After cooling to room temperature the slides were rinsed with water and blown dry with nitrogen. After transfer to the vacuum chamber of a coating unit (Balzer Baltec), the slides were coated with 3 nm of Cr, followed by 50 nm of Au. The slides were then held in a 1 mM solution of the thiol in toluene or ethanol for about 24 h. After extensive rinsing with toluene or ethanol to remove unbound thiols, the surface was blown dry with nitrogen. These slides were placed face-down in a crystallization flask, containing 300 ml of a 10 mM $CaCl_2$-solution. 10 mg (50 mg) of carboxymethyl cellulose, sodium salt (M_W ca. 250.000 g/mol, purchased from Aldrich) was added. After stirring to completely dissolve the polymer the pH-value was adjusted to 10 with an aqueous NaOH-solution. The flask was placed in a desiccator. Subsequently, the crystallization process was started by placing a petri-dish with 7 g $(NH_4)_2CO_3$ at the bottom of the desiccator. The crystallization process was performed at about 25°C (or at 12°C for the higher polymer concentration) and stopped after 5 days. The slides were removed and dried.

For SEM the slides on which the crystallization was carried out were cut in small pieces and fastened with conducting glue on aluminium sample holders. After sputtering with gold they were inserted into the SE microscope. The measurements were performed on a Zeiss DSM 962 at an acceleration voltage of 15 kV.

QCM-D-measurements were performed on a Q-sense D 300 system (Q-sense, Sweden). AT-cut quartz crystals coated with gold films are cleaned prior to use by a treatment with H_2O_2/NH_3/Millipore-water (1:1:5 by volume, 10min. 80°C) and subsequent rinsing with Millipore-water and isopropanol. After drying with N_2, the crystals were exposed to a diluted thiol-solution, subsequently rinsed with solvent and dried with N_2. After inserting them into the cell the temperature-controlled measurements were started in a pH-adjusted 0,01 M $CaCl_2$-solution. By exchanging this liquid for a corresponding solution containing carboxymethyl cellulose the adsorption of the polymer onto the thiol-terminated gold surface is monitored by a decrease of the frequency. Furthermore the energy dissipation D is measured simultaneously. The measurements were performed in a static solution (batch mode).

Raman micro-spectroscopy was performed with a LabRAM HR800 (Jobin Yvon, Horiba). This confocal Raman system is based on a dispersive spectrometer with notch-filter and focus length of 800 mm. It is equipped with an optical microscope Olympus BX41 and Peltier-cooled CCD-detector (Charge-coupled device). The spectra were excited with a 638,17 Å emission of a He-Ne-laser. The lateral resolution was better than 1,5 µm and the volume resolution was ca. 5 $µm^3$. The precision of the wave number was 0,5 cm^{-1} and the spectral resolution was about 0,7 cm^{-1}.

2.4.5. References

[1] (a) H. A. Lowenstam, S. Weiner (Eds.), *On Biomineralisation* Oxford University Press, New York, **1989**. (b) S. Mann, J. Webb, R.J.P. Williams, *Biomineralization: Chemical and Biochemical Perspectives*, VCH Publishers, New York, **1989**.

[2] (a) L. Addadi, S. Weiner, *Angew. Chem.* **1992**, *104*, 159-176; *Angew. Chem. Intl. Edn. Engl.* **1992**, *31*, 153-170. (b) S. Mann, D.D. Archibald, J.M. Didymus, T. Doughlas, B.R. Heywood, F. Meldrum, N.J. Reeves, *Science* **1993**, *261*, 1286-1292.

[3] L. Addadi, S. Weiner, *Proc. Natl. Acad. Sci. U.S.A.* **1985**, *82*, 4110-4114.

[4] (a) D. Jaquemain, S.G. Wolf, F. Leveiller, M. Deutsch, K. Kjaer, J. Als-Nielsen, M. Lahav, L. Leiserowitz, *Angew. Chem.* **1992**, *104*, 134-158; *Angew. Chem., Int. Ed. Engl.* **1992**, *31*, 130-152. (b) S. Rajam, B. R. Heywood, J. B. A. Walker, S. Mann, *J. Chem. Soc. Faraday Trans.* **1991**, *87*, 727. (c) B. R. Heywood, S. Mann, *Adv. Mater.* **1994***, 6*, 9.

[5] S. Weiner, L. Addadi, *J. Mater. Chem.* **1997**, *7*, 689-702. L. Addadi, S. Weiner, *Angew. Chem. Int. Ed. Engl.* **1992**, *31*, 153.

[6] (a) J.M. Marentette, J. Norwig, E. Stöckelmann, W.H. Meyer, G. Wegner, *Adv. Mater.* **1997**, *9*, 647-650. (b) M. Templin, A. Frank, A. DuChesne, H. Leist, Y.M. Zhang, R. Ulrich, V. Schadler, U. Wiesner, *Science* **1997**, *278*, 1795-1798. (c) J.N. Cha, G.D. Stucky, D.E. Morse, T.J. Deming, *Nature* **2000**, *403*, 289-292. (d) H. Cölfen, L. Qi, *Chem. Eur. J.* **2001**, *7,* 106-116. (e) L. Qi, H. Cölfen, M. Antonietti, M. Li, J.D. Hopwood, A.J. Ashley, S. Mann, *Chem. Eur. J.* **2001**, *7*, 2526-3532. (f) P. A. Bianconi, J. Lin, A. R. Strzelecki, *Nature* **1991,** *349*, 315.

[7] D. Walsh and S. Mann, *Adv. Mater.* **1997**, *9*, 658-662.

[8] (a) T. Kato, *Adv. Mater.* **2000**, *12*, 1543-1547. (b) N. Hosoda, T. Kato, *Chem. Mater.* **2001**, *13*, 688-693.

[9] (a) D. D. Archibald, S. B. Quadri, B. P. Gaber, *Langmuir* **1996**, *12*, 538-546. (b) J. Küther, W. Tremel, *J. Chem. Soc. Chem. Commun.* **1997**, 2029-2030. (c) J. Küther, R. Seshadri, W. Knoll, W. Tremel, *J. Mater. Chem.* **1998**, *8*, 641-650. (d) J. Küther, G. Nelles, R. Seshadri, M.

Schaub, H.-J.Butt, W. Tremel, *Chem. Eur. J.* **1998**, *4*, 1834-1842. (e) J. Küther, R. Seshadri, G. Nelles, H.-J. Butt, W. Knoll, W. Tremel, *Adv. Mater.* **1998**, *10*, 401-404. (f) J. Aizenberg, A. J. Black, G. M. Whitesides, *J. Am. Chem. Soc.* **1999**, *121*, 4500-4509.

[10] A. Ulman, *Chem. Rev.* **1996**, *96*, 1533-1554.

[11] L. Nasdala, A. Banerjee, T. Häger, W. Hofmeister, *Microscopy and Analysis, Europ. ed.* **2001**, *70*, 7-9.

[12] (a) W. T. S. Huck, A. D. Stroock, G. M. Whitesides, *Angew. Chem. Int. Ed. Engl.* **2000**, 39, 1058. (b) G. M. Whitesides, *Sci. Am.* **1995,** *273*, 146.

[13] M. Balz, Helen A. Therese, Jixue Li, J. S. Gutmann, M. Kappl, L. Nasdala, W. Hofmeister, H.-J. Butt, W. Tremel, *Adv. Mater.* **2004**, submitted.

3. Kinetic Studies on Nucleation by SANS

3.1. In-Situ Investigation of $CaCO_3$ Nucleation and Growth in the Presence of the Egg-white Protein Ovalbumin by Small-Angle Neutron Scattering

3.1.1. Introduction

Living organisms are capable of developing inorganic minerals and biocomposites with complex architectures to fulfill important biological functions, such as skeletal support or protection of soft tissues [1-4]. The inorganic materials are formed under physiological conditions with well defined properties, such as the combination of inorganic toughness with organic elasticity or the reduction of brittleness compared to their synthetic counterparts [5]. The inorganic mineral phase of such materials is formed over an insoluble organic matrix or mold, and the mineral phase is intimately associated with organic macromolecules, such as proteins, glycoproteins, polysaccharides, or proteoglycans. The biomacromolecules are highly acidic in nature and have been postulated to control nucleation, growth, crystal size, and the shape of the mineral phases [6,7,8].

Avian eggshells belong to the fast forming hard acellular composites in nature [9] whose calcified layer consists of ≈ 95% mineral and ≈ 5% organic phase. The mineral phase is basically calcite, the most stable polymorph of calcium carbonate, and it acts as a mechanical support and allows the diffusion of gases, water and ions. It is therefore essential for the survival of the embryo. The organic phase (proteins and proteoglycans) of the eggshell matrix is believed to be responsible for the nucleation and directed growth of the calcified layer. So far, several matrix proteins have been purified and characterized [10-20]. These proteins can be divided into three groups: noncallageneous bone proteins (osteopontin), eggshell specific proteins (ovocleidins and ovocallyxins), and egg white proteins (ovalbumin, ovotransferrin, and lysozyme).

Although their presence within the mineral layer has been demonstrated by immunohistochemistry [11,12,16], the role of these proteins in calcium carbonate mineralization is not well understood. The soluble macromolecules can interact either with the ions in solution, the ions of a crystal plane inhibiting the crystal growth in a certain direction or with an insoluble matrix. Egg white lysozyme and ovotransferrine have been shown to influence the morphology of the calcite crystals [21]. Usually the organic material is though to act as a template providing the structural information for the inorganic material that starts nucleating on the organic matrix. However, dermatan sulfate or hyaluronic acid were identified as parts of the chicken eggshell matrix [22-24], and it could be shown that the presence of purified dermatane sulfate proteoglycans obtained from the eggshell reduced the size of calcite crystals. The eggshell formation proceeds in the uterine fluid, a medium that comprises the inorganic material and the organic matrix. Investigations on the egg shell formation support the assumption that ovalbumin which is especially found in the initial phase of the uterine fluid, is involved in the nucleation process of shell calcification [25].

In spite of intense research on the ultra structure, composition and presence of organic macromolecules in the eggshell matrix, our information on the molecular mechanism of eggshell mineralization is still limited. We believe that the understanding of the role of the proteins involved in the eggshell formation will lead to a better understanding of the complex process of biomineralization.

Calcium carbonate is extremely widespread in biominerals. The polymorphs calcite, vaterite, and aragonite are not only found in avian eggshells but also in shells of mollusks and skeletons of echinoderms. In addition, it was found from investigations on sea urchin larval spicules that in the early stages of spicule growth amorphous $CaCO_3$ is present as a transient precursor. The amorphous phase transforms by-and-by into calcite, the stable crystalline phase [26,27]. Another example for the transformation of amorphous calcium carbonate (ACC) into a crystalline phase was observed in larval shells of marine bivalves. It was shown that the mineral deposited in the initial steps of the biomineralization was exceedingly amorphous and transformed subsequently in part into aragonite [28]. It is assumed that the transformation of ACC into a crystalline phase is much more widespread in biology than it is known to date, but because of its solubility and the difficulty of its detection might be often overlooked, especially when intimately associated with a crystalline phase.

In this contribution we present the results of time-resolved *in-situ* studies starting with the early stages of crystallization of calcium carbonate in the absence and in the presence of the egg-white protein ovalbumin by means of small-angle neutron scattering (SANS). We will first describe the underlying scattering laws and then present experimental data which we will then interpret and discuss in context with underlying theoretical considerations in literature. It might be mentioned that this paper represents the first detailed study of mineralization in the presence of a protein using the technique of small-angle neutron scattering.

3.1.2. Theoretical background of small-angle neutron scattering

In this part we introduce the scattering laws and scattering contrast conditions which are necessary to analyze the present scattering results of protein and mineralization. A characteristic property of the present measurements is the observation of µm large minerals and small protein particles.

Scattering laws. In scattering experiments the intensity of neutrons and other probes is measured as a function of the wave function Q being proportional to the scattering angle δ and inversely proportional to the wavelength λ according to $Q=(2\pi/\lambda)\sin\delta$. The typical range of pin-hole SANS experiments is between $10^{-3} < Q$ [$Å^{-1}$] < 0.2, which means that particles of sizes between 1000 and 10 Å can be fully analyzed with this technique. The scattering law of a single type of particle is given by the macroscopic cross-section (in [cm^{-1}] units)

$$\frac{d\Sigma}{d\Omega}(Q) = \frac{d\Sigma}{d\Omega}(0) \cdot P(Q) \tag{1}$$

with the extrapolated scattering at Q=0

$$\frac{d\Sigma}{d\Omega}(0) = \Phi V \Delta\rho^2 \tag{2}$$

delivering the volume fraction Φ, molar volume V of the particle, and scattering contrast $\Delta\rho^2$ of the particle. The scattering contrast will be discussed quantitatively later. In Equation (1) interference effects between the particles are neglected which is well fulfilled in diluted solutions as in our case. The form factor P(Q) describes the size and shape of the particle and can be evaluated for relatively simple forms as spheres etc.. In the limits of small and large Q with respect to the inverse size of the particle more general approximate forms of P(Q) are known. In the small Q limit Guinier's approximation

$$P(Q) = \exp(-R_g^2 Q^2 / 3) \tag{3}$$

is valid from which the radius of gyration R_g is derived. In the large Q limit ($Q>1/R_g$) one often observes a power law according to

$$P(Q) = P_\alpha \cdot Q^{-\alpha} \tag{4}$$

The exponent α can be equal to 4, 3, 2, and 1 for compact 3d-particles, porous 3d-particles, plates, and rods, respectively. The amplitudes P_α for $\alpha=1$ and 2 are given as

$$P_1 = \Phi(1-\Phi)\pi F_{rod} \exp(-Q^2 a^2 / 4)\Delta\rho^2 ; \quad P_2 = \Phi(1-\Phi) 2\pi d_{eff} \exp(-Q^2 d_{eff}^2 / 12)\Delta\rho^2 \tag{5}$$

In case of $\alpha=1$ and 2 one measures the perpendicular area $F_{rod}=\pi a^2$ of the rod and thickness d_{eff} of the plates, respectively. The exponent $\alpha=4$ represents Porod's law and

$$P_4 = 2\pi\, \Phi(S/V)\Delta\rho^2 \tag{6}$$

measures the total surface S of the particles.

The approximate laws at low and large Q are combined into Beaucage's form

$$\frac{d\Sigma}{d\Omega}(Q) = \frac{d\Sigma}{d\Omega}(0)\exp(-u^2/3) + P_\alpha\left[\left(\mathrm{erf}\left(u/\sqrt{6}\right)\right)^3 / Q\right]^\alpha \tag{7}$$

with $u=R_g$ Q. The erf(u) "takes care" of the validity of the underlying approximations in their Q ranges.

In the present situation, as we will see later, we observe a superposition of scattering from the order of µm and 30 Å sized mineral and protein particles, respectively. We therefore will discuss scattering described by the form

$$\frac{d\Sigma}{d\Omega}(Q) = P_4^M\, Q^{-4} + \left\{ \left.\frac{d\Sigma}{d\Omega}\right|_{Pr}(0)\exp(-u^2/3) + P_4^{Pr}\left[\left(\mathrm{erf}\left(u/\sqrt{6}\right)\right)^3 / Q\right]^4 \right\} \tag{8}$$

the first and second term from the mineral and protein, respectively.

Contrast variation in order to characterize the mineral particles. A basic and necessary property for successful application of scattering technique is related to the scattering contrast of the selected probe. In neutron scattering the contrast according to Equations (1) to (6) is described by $\Delta\rho^2$ as it is proportional to the scattered intensity according to

$$\frac{d\Sigma}{d\Omega}(Q) \propto \Delta\rho^2 \qquad (9)$$

The symbol $\Delta\rho = (\rho-\rho_S)$ describes the difference of the coherent scattering length density ρ of the particle as the mineral or protein and the solvent ρ_S. The coherent scattering length density for a given particle or a molecule is evaluated according to $\rho = \sum b_i / \Omega$ from the coherent scattering length b_i of the elements i and the volume of the atomic Ω complex. Here we only mention that hydrogen and deuterium have the very different coherent scattering lengths of $b_H = -3.7423\ 10^{-13}$ cm and $b_D = 6.674\ 10^{-13}$ cm.

Figure 3.1.1 summarizes the scattering length densities of solvent and particles relevant for this study; ρ is depicted versus the composition of D_2O in the D_2O/H_2O mixture.

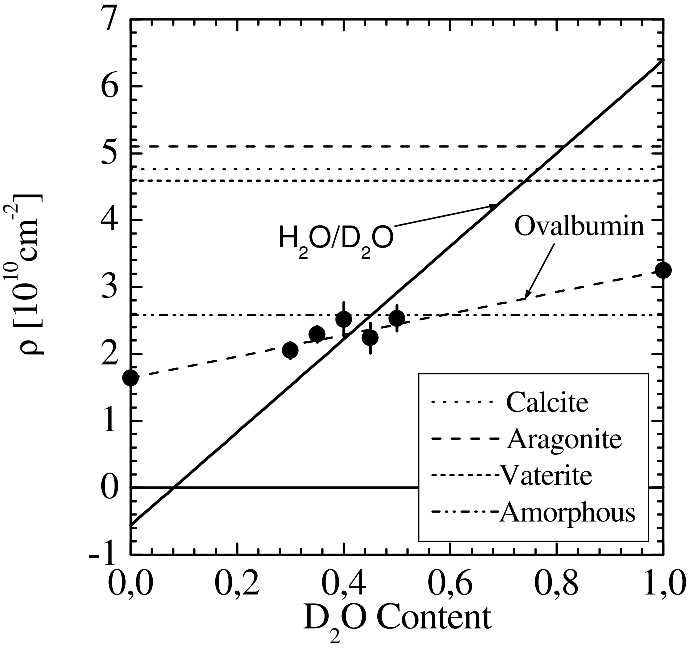

Figure 3.1.1: Scattering length density of the $CaCO_3$ polymorphs, the protein ovalbumin, and the aqueous D_2O/H_2O solution.

For the aqueous solvent and ovalbumin a linear increase from -0.561 to 6.39 (solid line) and 1.64 to 3.25 (dashed line) in units of 10^{10} cm^{-2} is evaluated, respectively. Quite characteristically, proteins in general show very similar scattering length densities; at about 40% D_2O content they are equal to that of water (e.g. they are in matched condition visible by the intersection of the two straight lines), and its change with D_2O is ascribed to the ability of proteins to partially exchange H for D at the outer surface, e.g. hydrophilic part of the protein. The constant values of ρ for the three crystalline polymorphs of calcium carbonate, namely, calcite, aragonite, and vaterite as well as for the amorphous form were evaluated from the chemical structure and mass density given in literature and are summarized in Table 3.1.1 [29]. The scattering length densities of the crystalline forms of $CaCO_3$ are close to each other, especially that of calcite and vaterite; the last two mentioned crystalline polymorphs are matched at 74% D_2O, aragonite at 84% D_2O content. The strong difference of scattering length density of the amorphous phase and crystalline polymorphs has to be mentioned; it is very near the coherent scattering length density ρ of the protein and offers the possibility to differentiate between amorphous and crystalline phases.

Table 3.1.1: Characteristics of the calcium carbonate crystalline polymorphs.

	D [g/cm^3]	Ω [10^{-23}cm^3]	ρ [10^{10}cm^{-2}]	Φ [D_2O]
Calcite	2.75 (2.71*)	6.044 (6.133)	4.76 (4.69)	0.764 (0.754)
Aragonite	2.95	5.634	5.10	0.813
Vaterite	2.65	6.272	4.49	0.739
Amorphous	1.49	11.15	2.58	0.451

3.1.3. Experimental section

In this section we will give a short description of the experimental conditions with respect to the sample characteristics as well as to the SANS experiments.

Sample preparation and characteristics. Ammonium carbonate (p.a.), sodium hydroxide (pellets, p.a.) and ovalbumin (> 85% on dry substance) were purchased from Acros, while calcium chloride tetra hydrate (99,995%, suprapur) was purchased from Merck. D_2O was purchased from Chemotrade and had a purity of 99.8%. All experiments were performed in deionized water (Millipore).

Neutron scattering experiments. The neutron experiments were performed at the KWS1 diffractometer being in the external neutron guide laboratory at the FRJ-2 research reactor of the Helmholtz research center Jülich. The experiments were performed with neutrons of wave length of 7 Å with a 20% half width of maximum and sample-to-detector distances from 20 to 2 m in order to overlap the whole possible Q interval. The data obtained from the sample were corrected for background scattering, sensitivity of the individual detector channels, and finally evaluated in absolute scale from calibration with a secondary standard. The scattering from pure solvent was measured and considered. The transmission describing the decrease of non-scattered neutrons by the sample was automatically measured for all spectra and could therefore be considered properly. The mineralization process was initiated and performed in a special containment of stainless steel with two sapphire windows being transparent for neutrons and with a temperature control between minus 20 to plus 100℃. This cell was placed in the neutron beam for in-situ SANS experiments. The experiments were usually performed for a time period of about 12 hours at two fixed settings of detector-to-sample distances of 20m and 4m with accumulation times of 15 and 30 min for the first 15 and the following measurements, respectively.

The process of mineralization of $CaCO_3$ was performed with the gas diffusion technique which was started by the diffusion of carbon dioxide into a 0.1 M aqueous $CaCl_2$-solution according to the chemical reaction

$$(NH_4)_2 CO_3 + CaCl_2 \rightarrow CaCO_3 + 2(NH_4)Cl \qquad (10)$$

All mineralization experiments were performed at a temperature of 30^0C and pH=10 which was chosen in order to maintain a sufficient concentration of carbonate ions during the whole mineralization process.

3.1.4. Experimental results

In this section we will present the SANS results we found for the protein in different conditions and will then discuss nucleation and growth of $CaCO_3$ mineralization without and with ovalbumin.

Protein ovalbumin. In a first step we performed SANS measurements on aqueous solutions of ovalbumin in order to characterize this protein. The results are depicted in Figures 3.1.2 and 3.1.3.

Figure 3.1.2a shows the scattering from three concentrations, namely, 2.5, 5, and 7.5 mg/ml ovalbumin in H_2O. The data were fitted by Guinier's law ((Equations (2) and (3)) as depicted by the solid lines. The two parameters R_g and the extrapolated forward scattering $d\Sigma/d\Omega(0)$ are plotted versus ovalbumin concentration in Figure 3.1.2b. An average R_g of (30±0.5)Å and a linear dependent $d\Sigma/d\Omega(0)$ with Φ is found in consistence with Equation (2); the slope gives $V\Delta\rho^2/(N_A d)$ = (20±0.7)ml²/g which is equivalent to $M\Delta\rho^2/(N_A d^2)$ with the mass density d, the molar volume V and molar mass M of the protein. These numbers are known from literature [30] and are summarized in Table 3.1.2; they lead to evaluate the coherent scattering length density of ρ=1.64 10^{10} cm^{-2} for ovalbumin in H_2O.

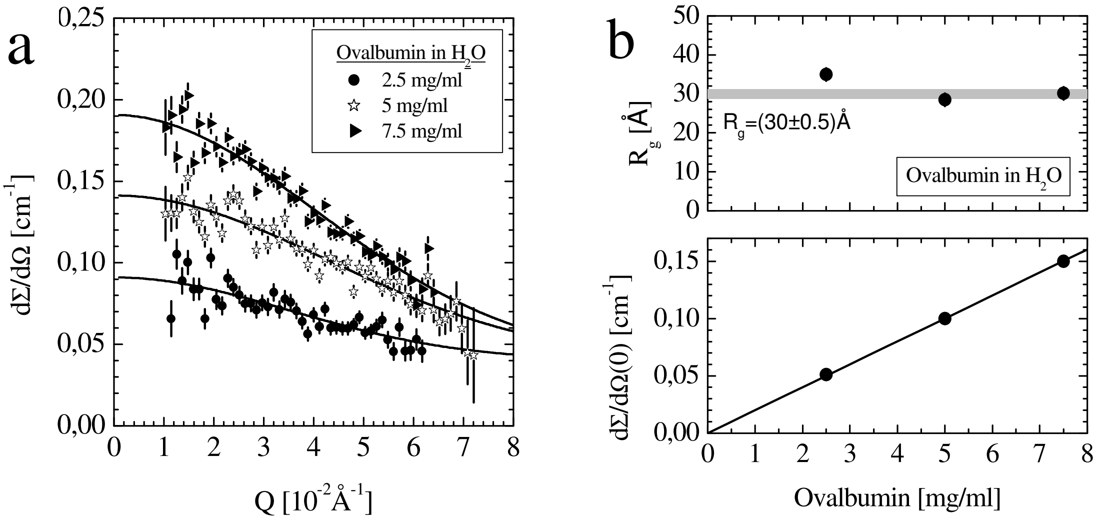

Figure 3.1.2: (a) Scattering from three concentrations of the protein ovalbumin in H_2O. (b) Radius of gyration R_g and extrapolated scattering at Q=0, $d\Sigma/d\Omega(0)$, versus protein concentration.

Table 3.1.2: Characteristics of the egg-protein ovalbumin.

Ovalbumin	
M_{Prot} [g/mol]	44600
V_{Prot} [cm^3/mol]	33300
d_{Prot} [g/cm^3] [x]	1.34
Number of Aminoacids	385
R_g [Å]	32.7±0.4
α	$-(2.7\pm0.6)10^{-4}$
ρ_{Prot} [$10^{10}cm^{-2}$]	$1.64+1.61\Phi_{D2O}$
ρ_{Water} [$10^{10}cm^{-2}$]	$-0.561+6.95\Phi_{D2O}$
Φ_{D2O} [match]	0.41

In a next step we performed contrast variation experiments on aqueous solutions of ovalbumin at a fixed concentration of 7.5 mg/ml. These results are represented in Figure 3.1.3a and b. The square root of scattered intensity versus D_2O concentration in Figure 3.1.3a is well fitted by a straight line according to $\sqrt{d\Sigma/d\Omega(0)} = \sqrt{\mathrm{cM}/(\mathrm{N_A d^2})}\ \Delta\rho$ (c concentration of ovalbumin in g/ml) leading to a linear change of $\Delta\rho = (\rho_{Ovalbu\min} - \rho_{Water})$. At 41.8% D_2O content the line intercepts zero indicating matching of the protein with water as expected from other SANS experiments on other proteins [31]. The parameters in Table 3.1.2 together with the ρ_{Water} give the scattering length density of ovalbumin versus D_2O content as depicted in Figure 3.1.1. One observes a change of protein scattering length density with D_2O caused by the H/D exchange at the outer surface of the protein. Proteins show quite generally a similar scattering length density [31].

Figure 3.1.3b depicts the square of R_g versus the inverse $\Delta\rho=(\rho-\rho_S)$, which is the so-called Stuhrmann plot. The square of R_g shows a negative slope of $\alpha=(2.7\pm0.4)10^{-4}$ and a $R_g=(32.7\pm0.6)$ Å at the intercept at $1/\Delta\rho=0$. The finite slope α is understood from an inhomogeneous mass distribution inside the protein; a negative α is a result from a larger scattering length density or a more concentrated mass in the center of the protein. The interpolated R_g = (32.7±0.6)Å at 1/Δρ=0 means the protein measured in the limit of infinite scattering contrast and, therefore, no sensitivity to the internal structure of the protein [31]. Usually a slightly positive slope is found!

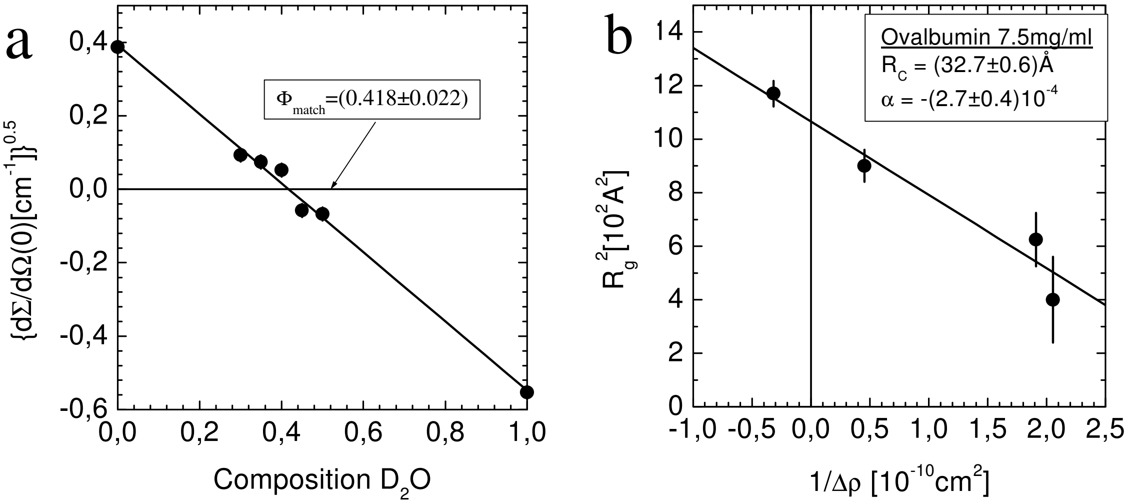

Figure 3.1.3: (a) $\sqrt{d\Sigma/d\Omega(0)}$ versus D_2O content; at Φ=0.42 the protein is machted. (b) The "Stuhrmann" plot gives the protein radius of gyration R_c of an homogeneous particle at infinite scattering contrast, e.g. at 1/Δρ=0. A negative α indicates a larger scattering length density or mass density at the centre of ovalbumin.

Ovalbumin in the presence of $CaCl_2$. Just before starting the process of mineralization with gas diffusion technique the protein and 0.1 M $CaCl_2$ aqueous solution were freshly prepared. First we wanted to prove the influence of $CaCl_2$ on the protein. The corresponding SANS data is shown in Figures 3.1.4 and 3.1.5. These measurements were performed waiting for about 13 h after the preparation of the sample. Compared to the native protein a characteristically different scattering is observed; in D_2O (Figure 3.1.4a) a strongly increased radius of gyration of nearly 600 Å and a roughly 50 time larger scattering at Q=0 is observed, and at intermediate and large Q a Q^{-2}- and Q^{-1}-power law become visible, respectively. This Q dependence has the characteristic behavior of the scattering law of a Gaussian linear chain with relatively large segments; for Gaussian chains a Q^{-2} power law is characteristic for Q larger than 1/R_g [32,33]. As the intensity at Q=0 is determined according to Equation (2) by the product of the protein volume fraction and molar volume the increase of intensity can only be caused by the aggregation of about 50 proteins forming a linear chain. At large Q the Q^{-1} power law indicates rod-like particles as will be discussed now in more quantitative detail.

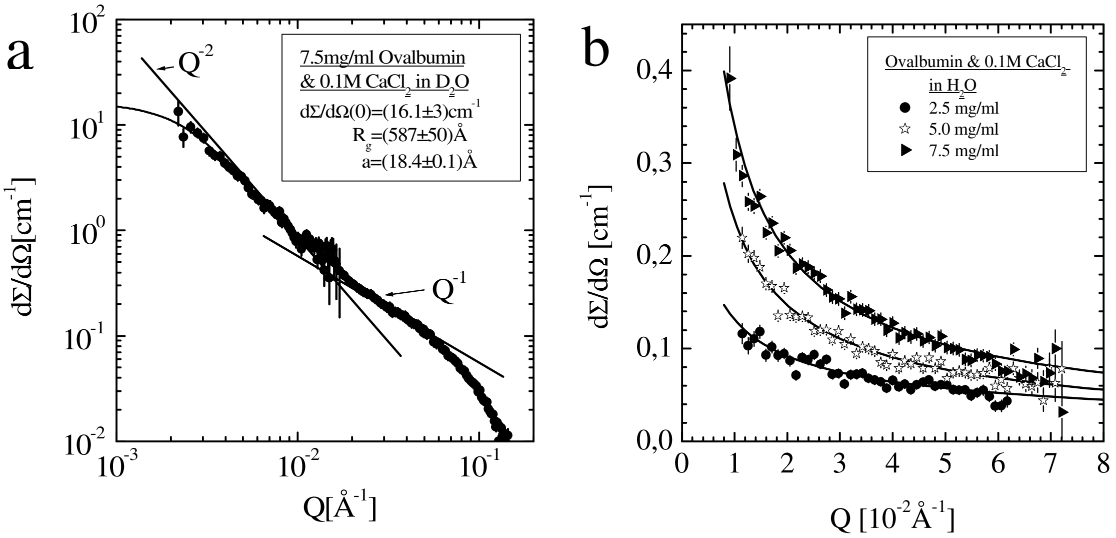

Figure 3.1.4: (a) Denaturated ovalbumin in D_2O solvent. As $d\Sigma / d\Omega(0) = 0.31\ \mathrm{cm^{-1}}$ for the native protein, the increase of $d\Sigma / d\Omega(0)$ is caused by the aggregation of about 50 proteins to an object which behaves as a Gaussian linear chain as seen by the Q^{-2} power law. The segments give rise to a Q^{-1} behavior of rods of nearly 40 Å diameter. (b) denaturated ovalbumin in 0.1 M $CaCl_2$ aqueous H_2O solution.

In Figure 3.1.4b three concentrations of the protein in H_2O are shown for larger Q, all curves are fitted with a Q^{-1} power law. The amplitude P_1 has been plotted in Figure 3.1.5; we get values which are strictly proportional to Φ (P_1=0 at Φ=0) with the slopes $\partial_C P_1 = \pi F \Delta\rho^2 / d =$ 0.73 and 0.42 in units of $cm^{-1}Å^{-1}/(g/ml)$ for D_2O and H_2O, respectively (Equation (5)). From both $\partial_C P_1$ a perpendicular area of the rods of 338 Å^2, e.g. the area occupied by the protein, is calculated if $\rho = 10^9 \mathrm{cm}^{-2}$ is added to the scattering contrast ρ_P of ovalbumin and which means a 6% larger scattering length density in H_2O. Such an increase of the protein scattering length density can be caused if about 120 Ca^{2+} ions are distributed within the protein as evaluated from the coherent scattering length $b_c(Ca)=4.7\cdot10^{-13}cm$ and the relationship $V_{Prot}\,\rho\,/\,b_c(Ca)$ (for V_{Prot} see Table 3.1.2).

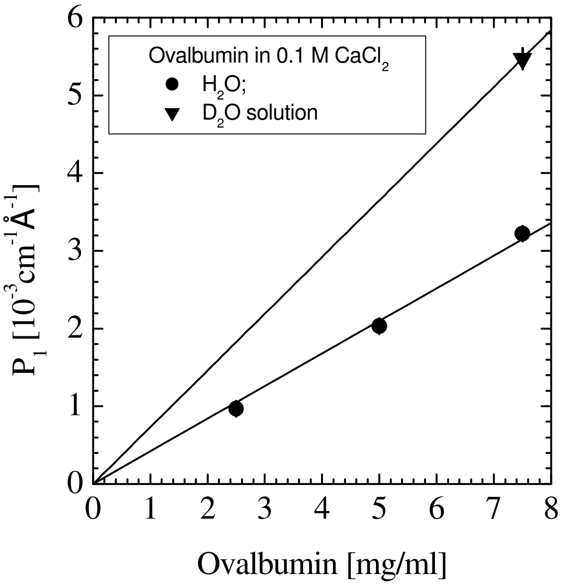

Figure 3.1.5: The amplitude P_1 is proportional to the ovalbumin concentration.

At Q values above 0.05 $Å^{-1}$ the finite width of the rods becomes visible from the scattering in the D_2O solvent; the deviation from Q^{-1} is described by Guinier's law for rods according to $P_1 \propto \exp(-Q^2a^2/4)$ (see Eq.(5)) which delivers a radius of the rods of slightly less than a = 19 Å. This gives an area of 1130 $Å^2$ and means, if compared with the area from P_1, that only 30% of the area is occupied by the protein.

Homogeneous nucleation and growth of calcium carbonate. The scattering patterns deriving from homogeneous crystallization of $CaCO_3$, i. e. in the absence of any additives, are presented in Figure 3.1.6 and 3.1.7.

The macroscopic cross-section versus scattering vector Q in Figure 3.1.6a-f shows the characteristic stages of nucleation and growth. During the first two hours Q^{-4} and Q^{-2} power law scattering is observed at low and large Q regimes, respectively. After more than two hours globular particles become visible.

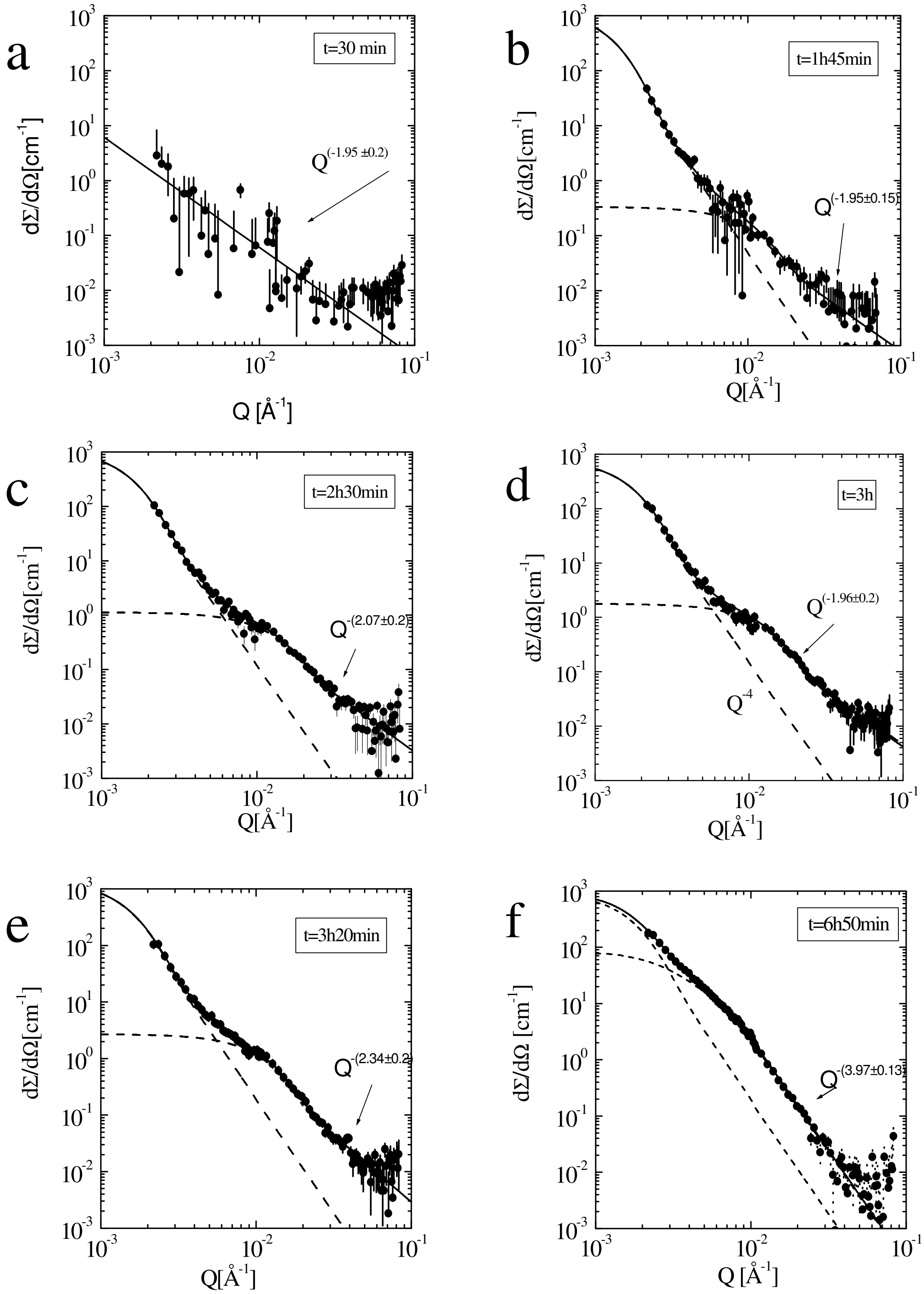

Figure 3.1.6: Scattering patterns observed during the mineralization of $CaCO_3$ in pure 0.1 M $CaCl_2$. A bimodal size distribution from very large and small minerals becomes visible. The large and small ones represent heterogeneous and homogeneous nucleation and growth, respectively. The parameters from the small particles are summarized in Figure 3.1.7 b-d.

In Figure 3.1.7 a-d the parameters analyzed are depicted. In a) the Porod constant from large particles is plotted versus time; the continuously increase of surface area visible from these particles probably stems from a heterogeneous mineralization process. On the other hand, the smaller visible particles must represent a homogeneous nucleation and growth mineralization process. During the first two hours only a slight increase of intensity is visible due to the nucleation of small particles of nearly platelet shape. The shape of plates is identified from the Q^{-2} power law behavior visible for the first two hours at large Q in Figure 3.1.6 a-c. After two hours particles with a R_g of 60 Å are formed which then continuously grow to sizes of 360 Å after 12 hours as depicted in Figure 3.1.7c. In parallel an increase of $d\Sigma / d\Omega(0)$ is observed as plotted in Figure 3.1.7b. In Figure 3.1.7d the exponent of the scattering at large Q from the smaller mineral particles is depicted; a fractal exponent less than four is observed during the time until about 6 hours when the Q^{-4} power law indicated the formation of compact mineral particles. The exponent less than four represents a mass fractal, e.g. an open structure which continuously becomes more compact as seen by the increase of the exponent.

The process of homogeneous nucleation starts just after the mineralization process has been initiated by the diffusion of carbon dioxide into the aqueous solution; the mineral nucleates into thin plates with a thickness less than 30 Å as concluded from the Q^{-2} power law behavior of the scattering patterns (Equation (5)). The period of nucleation takes about two hours and is followed by a growth process as seen from a transition to a mass fractal power law behavior and the observation of particles whose radius of gyration continuously increases from about 50 to 350 Å. These particles becomes continuously more compact as derived from the increase of the fractal dimensionality and after about six hours they become compact with a sharp interface as is demanded from Porod’s law (Equation (6)).

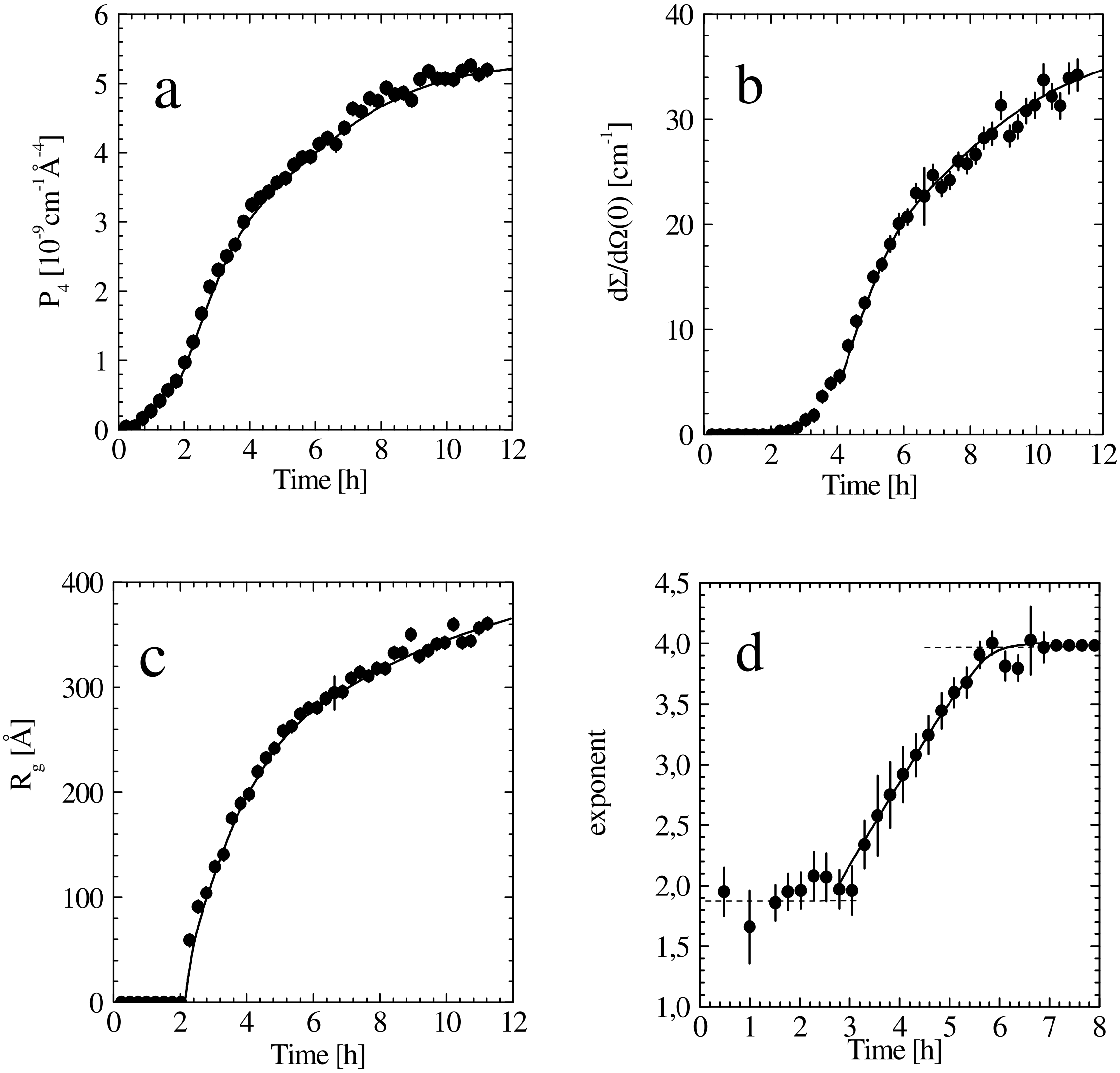

Figure 3.1.7: Parameters of scattering from Figure 3.1.6. (a) Porod constant versus time of µm large particles. As depicted in (b) and (c) $d\Sigma / d\Omega(0)$ and R_g from the small particles increases steadily for times later than 2 hours. Between 3 and 6 hours a fractal dimensionality indicates a relatively open structure of the minerals. (d) power law exponent from large Q, i.e. from small particles. During the first 2.5 hours plate shape(Q^{-2}) particles are observed and no size could be determined.

Nucleation and growth of $CaCO_3$ in the presence of ovalbumin. Performing the mineralization process in the presence of ovalbumin a different scattering behavior is observed. For all experiments the ovalbumin was dissolved in a 0.1 M aqueous $CaCl_2$-solution and the mineralization process was always performed in freshly prepared samples. Figure 3.1.8 shows the scattering patterns before (open triangles) and 13 hours (full dots) after starting the mineralization process.

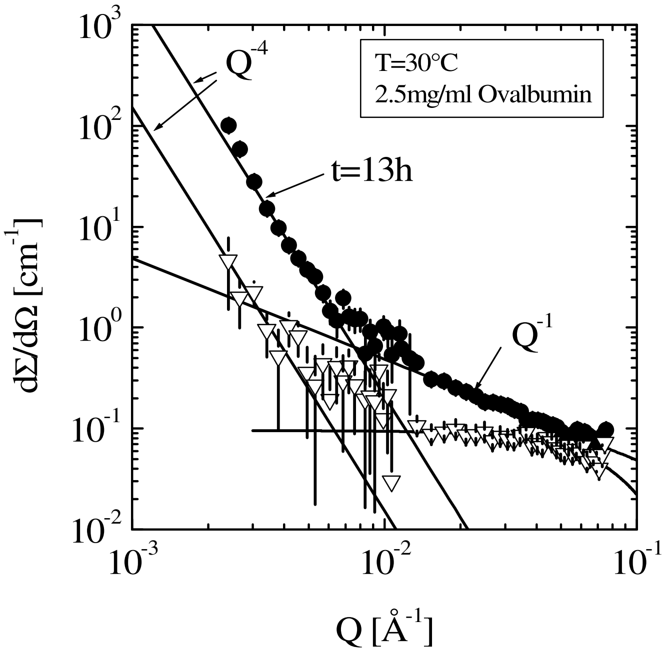

Figure 3.1.8: Scattering pattern before and after 13 h of mineralization in the presence of ovalbumin. The scattering from the mineral and protein can be distinguished clearly.

The scattering signal at large Q can be mainly attributed to ovalbumin, whereas the signal at small Q can be ascribed to the formed mineral phase. The size of the inorganic particles must be at least in the µm-range as only Porod`s Q^{-4} power law according to the basic equations (4) and (6) is obeyed. Because the SANS instrument is limited for Q smaller than 10^{-3} $Å^{-1}$, particles larger than about 10^3 Å can be determined only incompletely; the sole information about these mineral particles is the Porod constant P_4, which is proportional to the total outer mineral surface (Equation (6)). The evolution of P_4 has been plotted versus time in Figure 3.1.9 a-c for samples with 0.5, 2.5, and 7.5 mg/ml ovalbumin. For all concentrations the evolution of the mineral surface shows a characteristic shape. After about 1.5 hours P_4 strongly increases, between 2.5 and 3 hours a first pronounced maximum and between 6 and 8 hours a broader and less pronounced maximum become visible, and after about 20 hours P_4 obviously approaches a stationary state. This process is influenced by the amount of the protein; the first peak is small for the 0.5 mg/ml sample while more pronounced for the other two samples with larger amounts of ovalbumin. On the other hand, the second peak is stronger for the lower protein solution; obviously, there exists an inverse relationship between the strength of first and second peak. Generally, the time-resolved progression of P_4 appears to be composed of three individual processes; a quite phenomenological separation leads to three processes described by a Gaussian type behavior, a lognormal, and a tanh(t) type function, respectively.

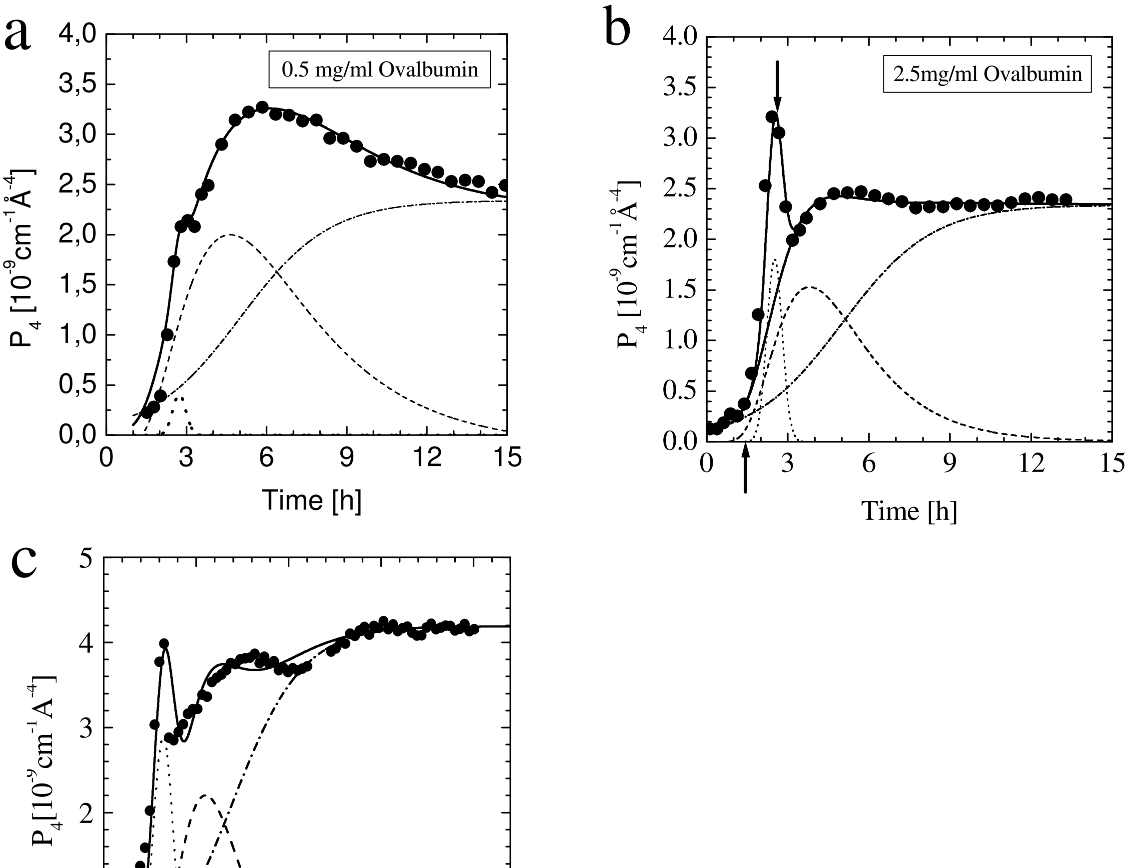

Figure 3.1.9: Progression of P_4 with time during mineralization in four 0.1 M $CaCl_2$ aqueous H_2O solutions (pH10). The process was always started with freshly prepared samples. Three processes become visible as indicated by the dashed lines.

Process 1 in particular always starts after about 1.5 hours and involves a strong increase of the mineral surface area which passes after about 3 hours through a maximum and sharply decreases afterwards, which might be interpreted as coming from dissolution of this mineral phase. There seems to be a strong correlation between process 1 and the protein as will be discussed later.

3.1.5. Interpretation of the SANS results

In the presence of ovalbumin we observe the formation of large mineral particles in the µm range just after the start of the mineralization process. With P_4 we measure the total surface of the mineral. In parallel we can follow the behavior of the protein from scattering at large Q. Both "particles" become visible because of their large difference in size. We also find different stages of the mineralization process. The aim of the next sections will be to acquire a better understanding of the mineralization processes shown in Figure 3.1.9 by additional SANS experiments applying contrast variation of the D_2O/H_2O aqueous solution.

Identification of the minerals by contrast variation. The impact of ovalbumin on the crystallization process of calcium carbonate is monitored by contrast variation of the aqueous solution as depicted in Figure 3.1.1. In Figure 3.1.10a the Porod constant P_4 is depicted versus time and shows the mineralization for the first 10 hours in the presence of 7.5 mg/ml ovalbumin for five different D_2O/H_2O mixtures. The solvent with 40% D_2O content is especially suited to nearly match the protein and amorphous $CaCO_3$ polymorph while the 74% D_2O solvent rather well matches the crystalline $CaCO_3$ polymorph. So, it is not surprising that P_4 shows characteristic differences with respect to the D_2O content; it is largest for H_2O and smallest for 74% D_2O solvent. In Figure 3.1.10b the square root of P_4 is plotted versus the D_2O content for different times of characteristic stages of mineralization. The points for each stage follow fairly well straight lines according to their proportionality with $\Delta\rho = |\rho_{Min.} - \rho_{Water}|$ assuming the same morphological structure of the mineral. At the intercept of $\sqrt{P_4} = 0$ the matching condition for the structure at that stage is achieved. After 2.5 and 3 hours mineralization when the first process is dominating we find the matching at 54 and 64% D_2O content which is near the theoretical condition for amorphous $CaCO_3$ of 45.1% D_2O content. Only one hour later after 4 hours mineralization we find matching at 79% which afterwards increases only slightly to 84% after 10 hours indicating the formation of crystalline $CaCO_3$, fitting best with aragonite (see Table 3.1.1). The principle result of this plot is a clear identification of the first mineralization process as an amorphous phase which starts to build up after about 1.5 hours gets its maximum volume fraction between 2.5 and 3 hours and is dissolved after about 4 to 5 hours.

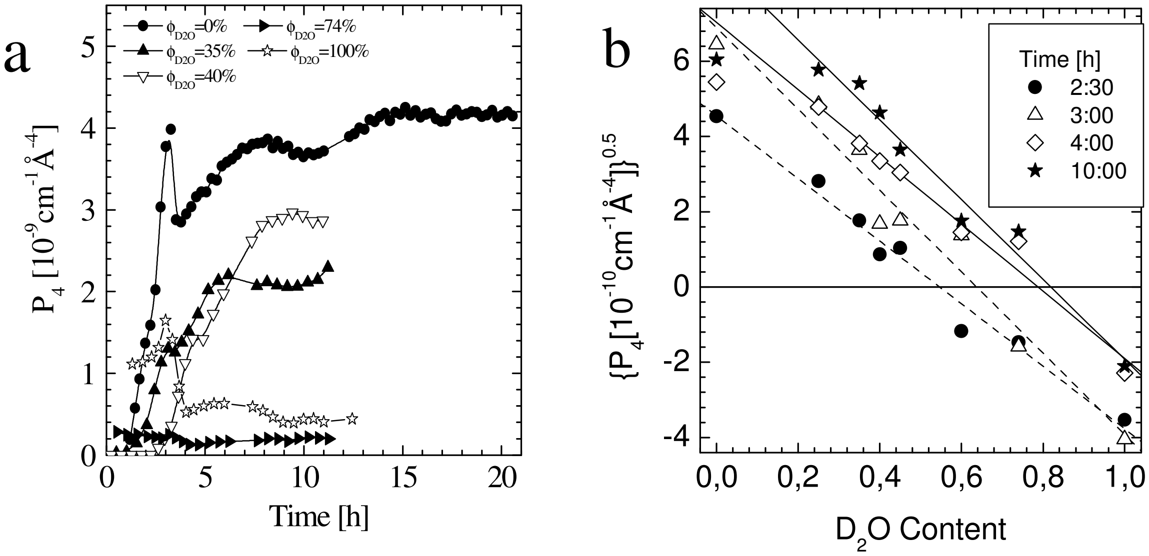

Figure 3.1.10: (a) Progression of P_4 with time during mineralization in the presence of 7.5 mg/ml ovalbumin in different H_2O/D_2O solvents as indicated. (b) Square root of P_4 versus D_2O content for the given times. The identification of the amorphous polymorph is clearly visible which has been dissolved after 4 hours.

Figure 3.1.11 shows a further aspect of mineralization. The integral over $d\Sigma/d\Omega(Q)$ from 2.2 10^{-3} to 0.17 $Å^{-1}$ has been depicted versus time for aqueous solutions of 0%, 74%, 82% and 100% D_2O contents. In all solutions the amorphous phase is visible between 2 and 4 hours. Apart from that, a strong increase is observed for H_2O, an overall slight decrease for D_2O, a deep minimum for the 74% D_2O solvent after 4 hours, and the minimum intensity for the 82% sample after 10 hours mineralization time. This behavior is understood if one looks at the coherent scattering length density depicted in Figure 3.1.1. The strong increase of intensity in the H_2O solvent is understood (i) from the formation of the mineral phases and (ii) from an increase of the scattering contrast caused by the transition from an amorphous to a crystalline phase. In the D_2O solution an overall decrease of intensity is visible which means a continuously decreasing scattering contrast according to $\Delta\rho = \left| \rho_{Min.} - \rho_{D_2O} \right|$ which is stronger than the gain of scattering from the formation of the mineral phase. The 74% D_2O sample shows a pronounced minimum at 4 hours mineralization time which means that the vaterite polymorph (see Table 3.1.1) is the dominating phase at this stage of mineralization. The subsequent increase of intensity is explained by a transition to the aragonite polymorph which would be matched in 84% D_2O aqueous solution. This is consistent with the results from the 82% solution; at times larger than 5 hours it shows the lowest intensity. In any case, the mineral phases show a continuously increase of scattering length density during mineralization as clearly derived from the negative slope of intensity in the D_2O solvent, which even compensates the gain of intensity from the formation of the mineral phases. These results give a basis of interpretation that $CaCO_3$ follow a sequence of polymorphs from amorphous, to vaterite, and finally to aragonite. A transformation to calcite as the most stable polymorph might occur at times later than the experimental time and would clearly become visible as its scattering contrast is very near to that of vaterite (Table 3.1.1).

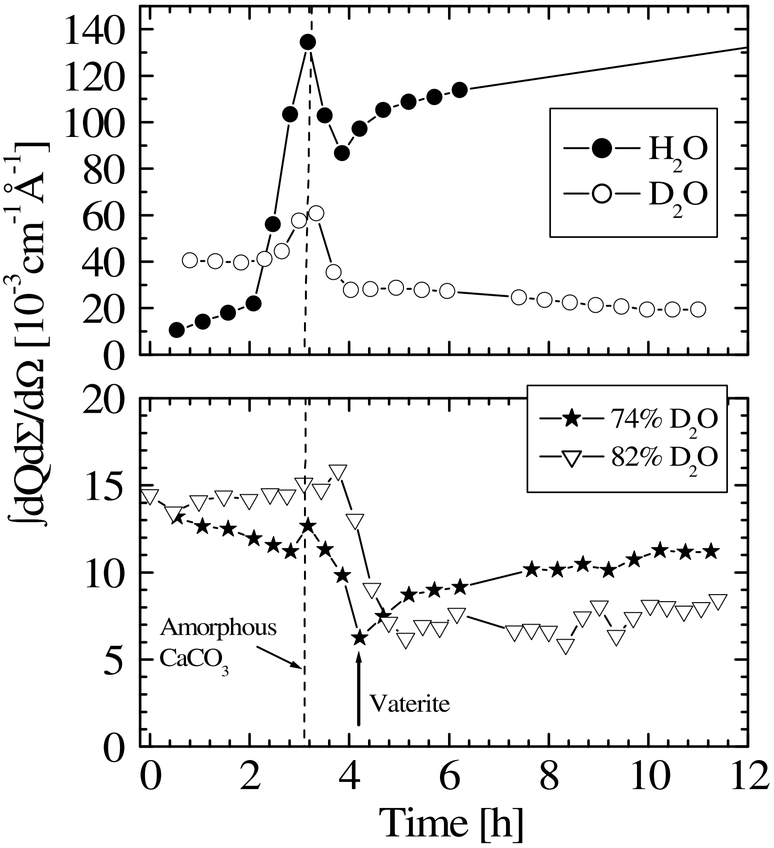

Figure 3.1.11: Integrated scattered intensity within the integration limits of 0.0022 to 017 Å^{-1}. The peak from the amorphous polymorph becomes visible around three hours and at four hours the minimum for the 74% D_2O solution identifies the vaterite polymorph. Aragonite seems to be the stable phase in this study which was stopped after 12 hours.

Mineralization in nearly matched condition for protein and amorphous $CaCO_3$. Figure 3.1.12 shows the scattering pattern after 4, 7, and 10.5 h mineralization at the contrast condition of 40% D_2O when only the crystalline calcium carbonate phase contributes to scattering. Here, a bimodal size distribution of large and small particles becomes visible. The fit parameters of the large particles, namely R_g, dΣ/dΩ(0), and P_4, show a continuously increase for times later than 4 hours (not depicted). The smaller particles are depicted in Figure 3.1.13. Their size increases between 4 and 6 hours from 60 to 140 Å and then stays constant. The extrapolated scattering at Q=0 dΣ/dΩ(0) increases and reaches its largest value at around 8 hours and then decreases which mean a dissolution of these particles as the R_g is constant. The Porod's constant decreases and approaches a constant value above 8 hours.

The identification of these particles is not so clear. This scattering could come from free particles in the solution which then would represent minerals of crystalline morphology which superimpose incoherently (e.g. their intensity is added) to the scattering. If this scenario is correct we are reminded to homogeneous nucleation and growth of $CaCO_3$ as presented in Figure 3.1.6 and 3.1.7 b-e representing mineralization without additives. However, the homogeneous formation of $CaCO_3$ without additives shows characteristic differences as a fractal dimension for times shorter than 6 hours and particle sizes larger by a factor of two. Another possible interpretation is to consider this scattering from inside the large mineral particles where part of the $CaCO_3$ is replaced by the protein. As in the presence of Ca^{2+} ions the proteins form large complexes during denaturation (see Figures 3.1.4 and 3.1.5), the size of 140 Å might be plausible. On the other hand a coarsening mechanism seems to be quite unrealistic for such proteins integrated within the mineral. A clear decision could be made from SANS contrast variation measurements but which is not so trivial from intensity reasons [34]. So, it appears plausible for us that the formation of these small particles represents a homogeneous nucleation and growth process of crystalline $CaCO_3$. This process occurs between 4 and 10 hours which is the same period of time when the "second" process of mineralization as derived from P_4 in Figure 3.1.9 is visible. So, we may speculate that the second process as represented in Figure 3.1.9 is related to a homogeneous process of mineralization.

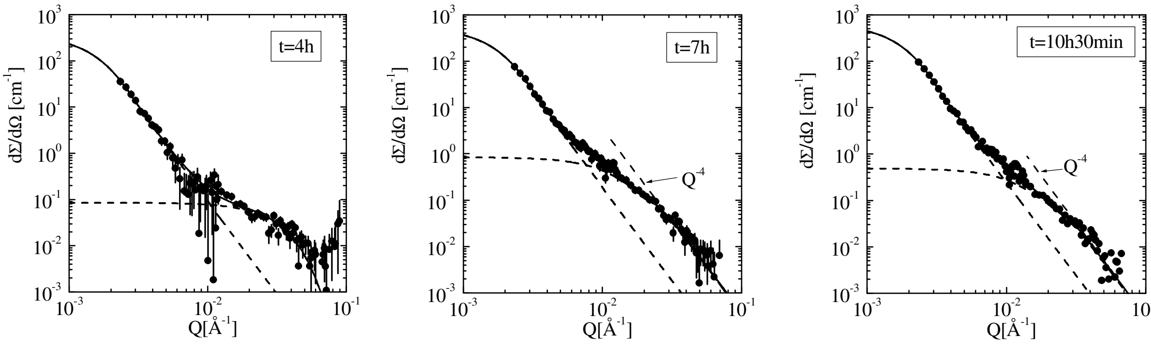

Figure 3.1.12: Scattering curves from mineralization in the 40% D_2O solution. In this solution only the crystalline polymorphs are visible. Besides the large particles also small particles appear.

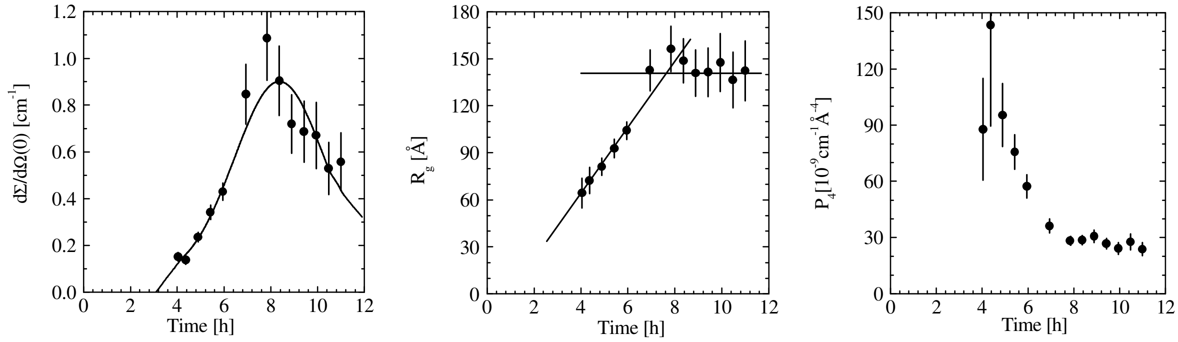

Figure 3.1.13: Parameters from small particles from scattering as depicted in Figure 3.1.12. This scattering reminds us to mineralization in solvent without any additives.

Behavior of the protein during mineralization of calcium carbonate. The behavior of the protein during mineralization can be studied because its scattering is well separated from the scattering of the minerals as demonstrated in Figure 3.1.8. Scattering from the protein in 2.5 mg/ml aqueous H_2O solution is depicted in Figure 3.1.14 which was measured during the mineralization shown in Figure 3.1.8 and 3.1.9b.

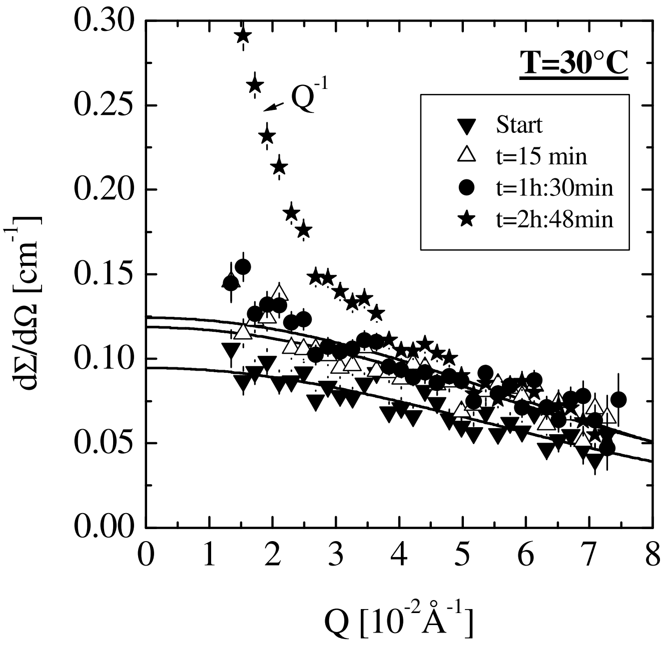

Figure 3.1.14: Time evolution of protein scattering during mineralization. A gradual transition from native to denaturated state is observed.

For the first 1.5 hours the scattering of the protein is described by Guinier's law indicating a compact native state. After this time a gradual transition to a Q^{-1} power law is observed which is finished after nearly 3h; denaturation of the protein occurs within these time limits. The strong increase of intensity at low Q indicates that the process of denaturation is accompanied by a complexion of several proteins; in Figures 3.1.4 and 3.1.5 we found a complexation of about 50 proteins. The time interval of denaturation is indicated by two arrows in Figure 3.1.9b; within this time interval the formation of the amorphous polymorph (first process) proceeds and holds. The amorphous phase dissolves when all proteins become denaturated.

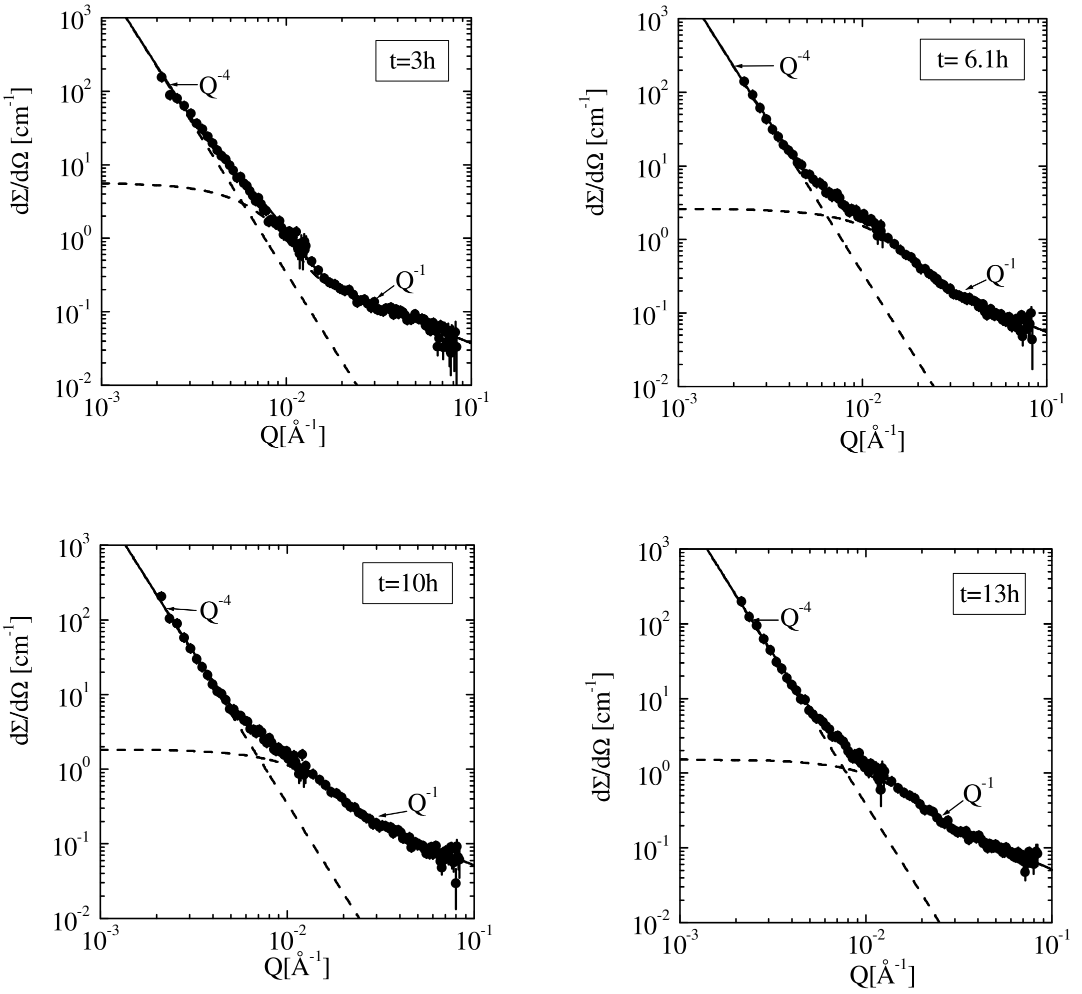

Figure 3.1.15: Time-resolved scattering from the progression of 7.5 mg/ml ovalbumin in H_2O during mineralization.

Another example is given in Figure 3.1.15 a-d showing the scattering at various stages of mineralization in the presence of 7.5 mg/ml protein in H_2O. The Porod scattering law at small Q (Equations (4) and (6)) and the scattering from the protein at large Q with its Q^{-1} power law due to rod-like scattering is clearly visible. P_4 from the minerals versus time with its characteristic shape is depicted in Figure 3.1.16a (H_2O contrast). The other fit parameters are summarized in Figure 3.1.16 b-d. The amplitude P_1 in (b) continuously increases and approaches a constant value shortly after 4 hours. Within this time period a strong scattering of the smaller particles, depicted as $d\Sigma/d\Omega(0)$ in (c), is found whose largest value occurs slightly later than two hours and is strongly reduced after 4 hours. A second but smaller and broader maximum is observed after seven hours. In parallel to the evolution of $d\Sigma/d\Omega(0)$ the radius of gyration R_g shows the same shape, a maximum length of about 300 Å at 2 hours, which after about 4.5 hours has been decreased to constant value of about 130 Å. This observation again supports an influencing effect of the protein onto the mineralization of the amorphous phase; the first 4 hours of mineralization are accompanied by strong changes of the protein conformation. During the presence of the amorphous $CaCO_3$ phase which occurs for the first 4 hours of mineralization, $d\Sigma/d\Omega(0)$ and R_g seems to reflect the process of protein denaturation accompanied by complexation; it becomes largest after 2 hours and then steeply decreases to a minimum value after four hours. $d\Sigma/d\Omega(0)$ of the native ovalbumin monomer gives a value of 0.15 cm^{-1} (Figure 3.1.2b); this means that protein complexes of about 50-60 protein monomers have been formed after 2 hours which is about the start of amorphous phase formation. After 4 hours the protein complexes have been decayed when the amorphous phase is dissolved.

The scattering for times later than 4 hours including the second broad peak we interpret as result from homogeneous nucleation and growth of crystalline minerals. We came to this conclusion from comparing these data with the data in Figure 3.1.13; the time evolution and particle size is the same while $d\Sigma/d\Omega(0)$ in H_2O has to be divided by 3.9 (assuming aragonite particles) in order to get the corresponding number in 40% D_2O solution; the ratio of both peaks is of about 3 and therefore in good consistence with the interpretation of homogeneous mineralization.

The two examples of this section of direct comparison of time evolution of the mineral particles and the process of complexation during denaturation of the protein give a strong support of the influence of the protein ovalbumin on the $CaCO_3$ mineralization especially on its amorphous phase formation.

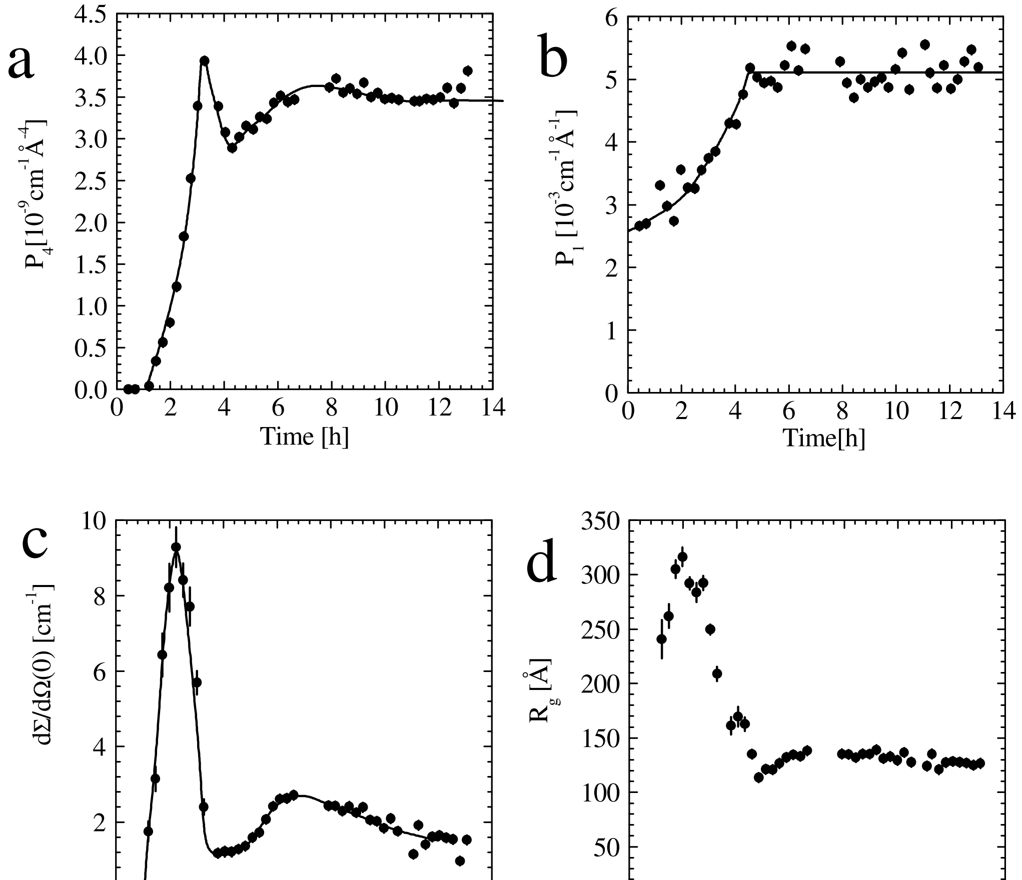

Figure 3.1.16: Parameters of mineral and protein during mineralization as depicted in Figure 3.1.15. (a) P_4 is the same as in Figure 3.1.9d. (b) P_1 amplitude show stable values above 4 hours. In (c) and (d) the process of complexation and decomplexation of the protein is clearly visible which proceeds in parallel to the amorphous polymorph. At later times $d\Sigma / d\Omega(0)$ and R_g are interpreted due to homogeneous nucleation and growth.

3.1.6. Discussion

The increase of CO_2 concentration in an aqueous 0.1 M $CaCl_2$ solution by thermal decompositon of ammonium carbonate and its diffusion into the solvent triggers a mineralization process which involves the Ca^{2+} loaded ovalbumin. We assume that the observed unfolding and cross linking of about 50 proteins to a single complex can be ascribed to a complexation of Ca^{2+}-ions by the carboxylate groups in the interior of the ovalbumin molecule. This complexation leads to a loss of hydrogen bonds and a simultaneous "loading" of the protein with Ca^{2+}-ions. As a consequence, the denaturated ovalbumin represents an enlarged complex of about 50 unfolded polypeptide chains of conformation which is similar to a linear Gaussian polymer chain with relative large statistical segments (Figure 3.1.4a). This protein structure represents an accumulation of Ca^{2+} ions which may act as a nucleation center when the CO_3^{2-} concentration passes a threshold value. The extension of the enhanced Ca^{2+}-ion accumulation is determined by the size of the protein complex which is in the range of about 1000 Å as determined from the radius of gyration R_g and might be the reason for the order of μm mineral size right from the beginning. The particle size of the three processes of mineralization could not be determined with SANS as the smallest Q is about 10^{-3} Å^{-1}. So, "only" their total surface via Porod's constant P_4 could be determined and followed in-situ as depicted in Figure 3.1.9. Its first maximum is associated with the formation of amorphous $CaCO_3$ particles as could be directly derived from contrast variation SANS experiments. After four hours the particles representing the second and third process are of crystalline structure (Figure 3.1.10b). Process 2 seems to be related to a homogeneous nucleation process as within this time interval an independent formation of smaller crystalline particles is observed (Figure 3.1.13 and 3.1.16), and the second maximum of the progression of P_4 might be attributed to a coarsening of this mineralized particles; the process of coarsening leads to a decrease of the surface area and consequently to a lowered Porod constant P_4.

The mineral particles of the final stage were identified as aragonite. The results in Figure 3.1.11 show varying polymorph phases during the time evolution of mineralization; starting with the amorphous phase a transition to vaterite appears after 4 hours as visible in Figure 3.1.11 by the steep minimum of the 74% D_2O

solvent and the subsequent increase of scattering while the 82% D_2O solvent shows a relative flat minimum after 5 hours in consistence with an aragonite phase. The stable calcite phase would show a minimum at 76% D_2O solvent which is very near the vaterite phase of 74%D_2O solvent (Table 3.1.1).

This observation is in consistence with the kinetic picture of mineralization as discussed by S. Mann [3].

With respect to the influence of ovalbumin on the process of mineralization we can conclude that the protein is involved in the formation of the amorphous phase; the mineralization destroys the complexation as is clearly seen in Figure 3.1.16c and d. About a possible further influence of the protein onto the crystalline polymorph phases we have no information from our SANS experiment.

The mineralization of $CaCO_3$ in the presence of the protein ovalbumin has to be compared with homogeneous nucleation discussed in Figures 3.1.6 and 3.1.7. Here we observe the process of nucleation and growth. During the first 2 hours the nucleation of two-dimensional particles is observed which start to grow from about 50 to 350 Å particles after 12 hours, between 3 and 6 hours as fractal objects of increasing compactness as the fractal dimensionality is increasing from two (two-dimensional particles) to four (compact particles) (Figures 3.1.6 and 3.1.7). Such homogeneous nucleation of compact particles (no fractal dimensionality) is also observed for the process in the presence of ovalbumin. In this respect, it has to be mentioned that in the case of calcium phosphate the formation of a precursor, i.e. nucleus prior to the formation of hydroxyapatite has been postulated. Here, phosphate clusters known as “Posner clusters” with a size of about 10 Å represent the growth unit and it is assumed that the arrangement of these nanometer-sized units results by selective hexagonal packing in the growth of hydroxyapatite [35,36].

3.1.7. Summary and conclusions

In this work we presented the results of time-resolved investigations of the crystallization of calcium carbonate using the technique of small-angle neutron scattering (SANS). We followed the mineralization in-situ from the very early stages to the late ones. The mineralization process was studied both in the absence and in the presence of the egg-white protein ovalbumin. It was found that the crystallization process without ovalbumin shows immediately from the beginning µm large crystals probably from heterogeneous nucleation at the glass surface of the cuevette. In parallel the formation of small particles is observed from homogeneous nucleation. This process shows three stages that involves as nuclei the formation of thin $CaCO_3$-plates with a thickness less than 30 Å prior of their assembly (growth) to form 3-dimensional particles from 50 to 350 Å, first between 2 and 6 hours of mass-fractal structure with continuously increasing compactness. In the presence of the hen-egg protein ovalbumin the nucleation and growth process of calcium carbonate involves the formation of different polymorph structures; in a first process an amorphous calcium carbonate phase is formed which proceeds in parallel with denaturation and complexation of the ovalbumin and separates into smaller units when the amorphous phase is dissolving. During the formation and dissolution of the amorphous phase crystalline phases are formed which pass through the vaterite polymorph and become at the end after about 12 h that of aragonite. A transition to the most stable polymorph calcite was not observed, but would be clearly visible as calcite has a similar contrast as vaterite (Table 3.1.1). The identification of the various polymorph phases was possible by using contrast variation techniques which is very straightforward in neutrons scattering by performing the mineralization in D_2O/H_2O aqueous solution of varying composition.

The insight of $CaCO_3$ mineralization by SANS given here for the first time is of great importance for a better understanding of the nucleation and growth process in biological systems. As well as the matter of fact that homogeneous crystallization of calcium carbonate has not been investigated in such detail inspired us to try to shed light on the very early stages of the crystallization process of calcium carbonate and help to find out whether the formation of a precursor is universally valid. The general presence of such nanometer-sized precursors could contribute to a better understanding of the nucleation process and provide new aspects concerning the interaction of biological structures (e.g. proteins) with the emerging mineral surface.

3.1.8. References

[1] H.A. Lowenstam, *Science* **1981**, *211*, 1126-1131.

[2] L. Addadi, S. Weiner, *Angew. Chem., Int. Ed. Engl* **1992**, *31*, 153-169.

[3] S. Mann, *Biomineralization*, Oxford University Press, Oxford **2000.**

[4] E. Bäuerlein, *Biomineralization*, Wiley-VCH, Weinheim, **2000.**

[5] Y. Levi-Kalisman, G. Falini, L. Addadi, S. Weiner, *J. Struct. Biol.* **2001**, *135*, 8.

[6] A.H. Heuer, D.J. Fink, V.J. Laraia, J.L. Arias, P.D. Calvert, K. Kendall, G.L. Messing, J. Blackwell, P.C. Riecke, D.H. Thompson, A.P. Wheeler, A. Veis, A.I. Caplan, *Science* **1992**, *255*, 1098-1105.

[7] A. Linde, A. Lussi, and M. A. Crenshaw, *Calcif. Tissue Int.* ***1989*****,** *44*, 286-295.

[8] S. Weiner, L. Addadi, *Trends Biochem. Sci.* **1991***, 16,* 252-256

[9] J.L. Arias, D.J. Fink, S.Q. Xiao, A.H. Heuer, A.I. Caplan, *Int. Rev. Cytol.* **1993**, *145*, 217-250.

[10] J. Gautron, M. T. Hincke, K. Mann, M. Panhéleux, M. Bain, M. D. McKee, S. E. Solomon, and Y. Nys , *J. Biol. Chem.* **2001**, *276***,** 39243-39252.

[11] M. T. Hincke, J. Gautron, C. P. W. Tsang, M. D. McKee, and Y. Nys, *J. Biol. Chem.* **1999,** *274,* 32915-32923.

[12] M. T. Hincke, C. P. W. Tsang, M. Courtney, V. Hill, and R. Narbaitz, *Calcif. Tissue Int.* **1995**, *56*, 578-583.

[13] M. T. Hincke, *Connect. Tissue Res.* **1995**, *31***,** 227-233.

[14] J. Gautron, M. T Hincke, J. M. Garcia-Ruiz, J. M. Dominguez-Vera, and Y. Nys , *Eggs and Egg Products Quality* (Kijowski, J., and Pikul, J., eds), pp. 66-72, *Proceedings VII European Symposium, Pozhaus, Poland,* **1997**.

[15] K. Mann, and F. Siedler, *Biochem. Mol. Biol. Int.* **1999***, 47***,** 997-1007.

[16] K. Mann, *FEBS Lett.* **1999***, 463***,** 12-14.

[17] Y. Nys, J. Gautron, M. D. McKee, J. D. Garcia-Ruiz, and M. T. Hincke, *World Poult. Sci. J.* **2001***, 57***,** 401-413.

[18] J. L. Arias and M. S. Fernandez. *World Poult. Sci. J.* **2001***, 57***,** 349-357.

[19] I. Lavelin, N. Meiri and M. Pines, *Poult. Sci.* **2000***, 79***,** 1014-1017.

[20] M. Panhéleux, M. Bain, M. S. Fernandez, I. Morales, J. Gautron, J. L. Arias, S. E. Solomon, M. T. Hincke, Y. and Nys, *Br. Poult Sci.* **1999***, 40,* 240-252.

[21] M. T. Hinke, J. Gautron, M. Panhéleux, J. M. Garcia-Ruiz, M. D. McKee, and Y. Nys, *Matrix Biol.* **2000***, 19***,** 443-453.

[22] D. A. Carrino, J. P. Rodriguez, and A. I. Caplan, *Connect. Tissue Res.* **1997***, 36***,** 175-193.

[23] R. K. Heaney and D. S. Robinson, *Biochim. Biophys. Acta* **1976***, 451***,** 133-142.

[24] T. M. Wu, J. P. Rodriguez, D. J. Fink, D. A. Carrino, J. Blackwell, A. I. Caplan, A. H. Heuer, *Matrix. Biol.* **1995***, 14***,** 507-513.

[25] J. M. Dominguez-Vera, J. Gautron, J. M. Garcia-Ruiz, and Y. Nys, *Poult. Sci.* **2000***, 79***,** 901-907.

[26] E. Beniash, J. Aizenberg, L. Addadi, S. Weiner, *Proc. R. Soc. London Ser. B* **1997**, *264*, 461.

[27] S. Raz, P. C. Hamilton, F. H. Wilt, S. Weiner, L. Addadi, *Adv. Funct. Mater.* **2003**, *13*, 480.

[28] I. M. Weiss, N. Tuross, L. Addadi, S. Weiner, *J. Exp. Zool.* **2002**, *293*, 478.

[29] J. Bolze, B. Peng, N. Dingenouts, P. Panine, T. Narayanan, and M. Ballauff, *Langmuir* **2002**, *18*, 8364-8369.

[30] J.C. Holt, J.M. Creeth, *Biochem. J.*, **1972**, *129*, 665.

[31] B. Jacrot, *Rep. Prog. Phys*. **1976**, *39*, 911-953.

[32] J.S. Higgins, H.C. Benoît, *Polymers and Neutron Scattering*; Clarendon Press, Oxford **1994**.

[33] R.J. Roe, *Methods of X-Ray and Neutron Scattering in Polymer Science*, University Press, Oxford **2000**.

[34] H. Endo, D. Schwahn , H. Cölfen*, J. Chem. Phys.*, **2004**, *120*, 9410-9423.

[35] A. S. Posner, F. Betts, *Acc. Chem. Res.* **1975**, 8, 273.

[36] Onuma, A. Ito, *Chem. Mater.* **1998**, *10*, 3346.

3.2. Nucleation and Growth of $CaCO_3$ Minerals on Biomimetic Templates studied by Small-Angle Scattering

3.2.1. Introduction

The mineralization process of inorganic materials in the presence of organic template structures in nature is still poorly understood and a challenge for scientific research [1]. Scattering techniques such as small-angle scattering with X-rays and neutrons may have a chance to make important contributions to this problem as they especially allow the exploration of the early stages of mineralization. Especially, small-angle neutron scattering (SANS) allows in many cases the characterization of complex structures by applying contrast variation technique and thereby the identification of their different parts as e.g. the conformation of polymers or chains in $CaCO_3$ minerals [2]. In the present case of an aqueous solution contrast variation can be easily applied by using D_2O/H_2O mixtures of different composition and thereby changing the coherent scattering length of the solvent.

In this paper we will present first results of this very new subject. We studied the mineralization of $CaCO_3$ in "pure" water and in the presence of a template structure formed by 4-dimethylamino-pyridine (DMAP) which in most cases was attached to the surface of colloidal gold. Our studies so far were mainly performed in H_2O in order to have good contrast conditions with respect to $CaCO_3$. Although DMAP is not a realistic model of biological template molecules, it allows to obtain aqueous solutions of template covered colloidal gold in a sufficiently high concentration [3] to allow a detailed understanding of the interfacial mineralization processes, which can be useful in an analysis of more realistic models and biological systems.

3.2.2. Results and discussion

Homogeneous mineralization. Scattering patterns from homogeneously mineralized $CaCO_3$ in water at 30°C are presented in Figure 3.2.1. The macroscopic cross-section is depicted versus the scattering vector Q in double logarithmic scale. The scattering vector is determined according to

$$Q = 4\pi / \lambda \sin\left(\theta / 2\right) \tag{1}$$

from the neutron wave length λ and the scattering angle θ. The mineral nucleates into thin plates with a thickness less than 30 Å as concluded from the Q^{-2} power law behavior of the scattering patterns. After about 1h (curve with symbol: ?) a transition from a Q^{-2} to a Q^{-3} is observed indicating the growth regime of porous three-dimensional (3D) particles. The inset shows the averaged intensity over the given Q range versus time. The nucleation starts right from the beginning when the mineralization was started and leads to a stronger increase after 1 h when the growth process of the 3D-particles has started.

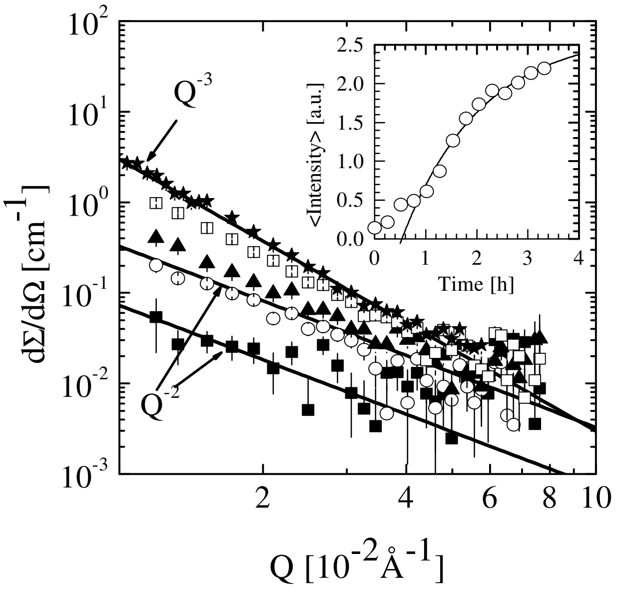

Figure 3.2.1: Time resolved scattering patterns from a homogeneous mineralization of $CaCO_3$ in H_2O at 30℃. A Q^{-2} shape of the scattering patterns was found from the beginning (¦) and after 30 min (?) of mineralization. After 1 h (?) a transition to a Q^{-3} shape is observed indicating the formation of porous 3D-particles after 1.5 (?) and 3.3 h (⋆). The measurement time was always 15 minutes and the given times represent the start of a measurement. The inset shows the intensity averaged over the given Q range versus time.

Mineralization on DMAP templates. Figure 3.2.2 shows the scattering patterns of a mineralization process at 30°C in the presence of 15 mg/cm^3 DMAP molecules. The first curve (circles) refers to the solution of DMAP, while the second refers to the sample in which the mineralization process has been active for 6 h. The DMAP molecules in water precipitate into a bimodal size distribution of large compact aggregates according to the Porod behavior at low Q and of smaller particles of roughly 20 Å. The solid lines represent a fit of the following scattering law

$$\frac{d\Sigma}{d\Omega}(Q) = P_1\, Q^{-4} + \left\{ I_0\, \exp(-u^2/3) + P_2 \left[\left(\mathrm{erf}\left(u/\sqrt{6} \right) \right)^3 /Q \right]^4 \right\} \tag{2}$$

describing the scattering from particles larger than of the order of 1000 Å due to the smallest Q of 0.002 Å^{-1} by the Porod constant P_1 and from smaller ones by the second term. The parameters have the following meaning: $u=R_g Q$ with the radius of gyration R_g; $I_0=CV^2$ representing the forward scattering of the smaller particles and being proportional to the square of the particle volume V and the constant C = N_P? ?^{2}, determined by the particle number density N_P, and the difference of the coherent scattering length density ? ? of the particle and water; the Porod constant P_2=2pCS with S the particle surface area. The scattering law for the smaller particles in (2) was formulated by Beaucage [4] for spherical shape particles from the approximate forms of the Guinier and Porod laws being valid for Q smaller and larger than the inverse radius of gyration $1/R_g$, respectively [5]. The radius R of spheres is either evaluated from the radius of gyration according to $R=(5/3)^{1/2}R_g$, or from the particle volume and surface area as derived from I_0 and P_2, respectively. A possible non-spherical shape of the particles can be derived from these parameters. Such non-spherical particles were indeed observed in the present study indicating plate shape particles. But such a detailed analysis will not be discussed here.

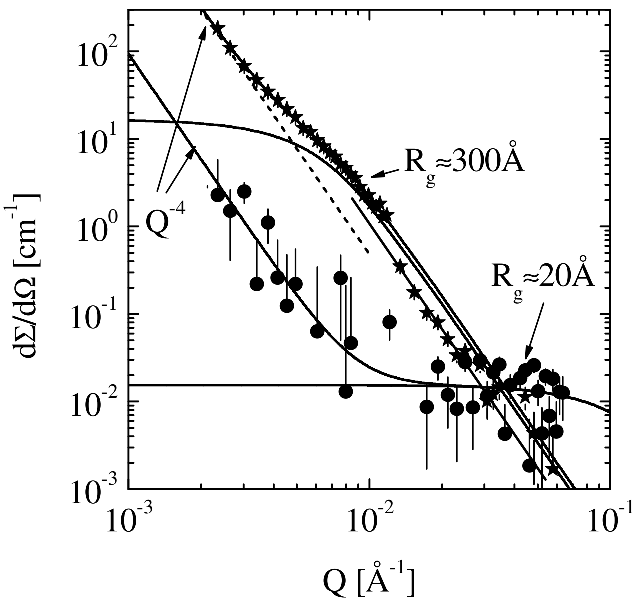

Figure 3.2.2: Small-angle scattering before (?) and after 6 h of mineralization (*) in the presence of 15 mg/cm^3 DMAP molecules at 30℃.

The SANS data in Figure 3.2.2 show that the DMAP molecules are not dissolved as discrete molecules; calculations show that under such circumstances their scattering would be too weak to be detected because of their small size and low volume fraction.

After a mineralization period of 6 h a strong increase of intensity is found; according to the bimodal structure of the template molecules large and small compact minerals have been formed during the mineralization process, the smaller ones of about 300 Å radius.

Mineralization on DMAP plus gold templates. Figure 3.2.3 shows the process of mineralization in the presence of 49 mg/cm^3 gold plus DMAP molecules at 30℃. Again we find indications of large aggregates mainly consisting of DMAP molecules as followed from contrast variation measurements [6] and smaller particles of 40 Å identified as colloidal gold with attached DMAP. Smaller DMAP aggregates are not visible as the scattering from the gold particles is dominating. After slightly more than 15 h mineralization time an order of magnitude increase of intensity is measured indicating an increased amount of larger particles. Surprisingly, the size of smaller particles does not increase due to mineralization but decreases in number density. It seems that under these experimental conditions the mineralization process leads to an aggregation of the smaller gold particles into the already existing larger DMAP aggregates.

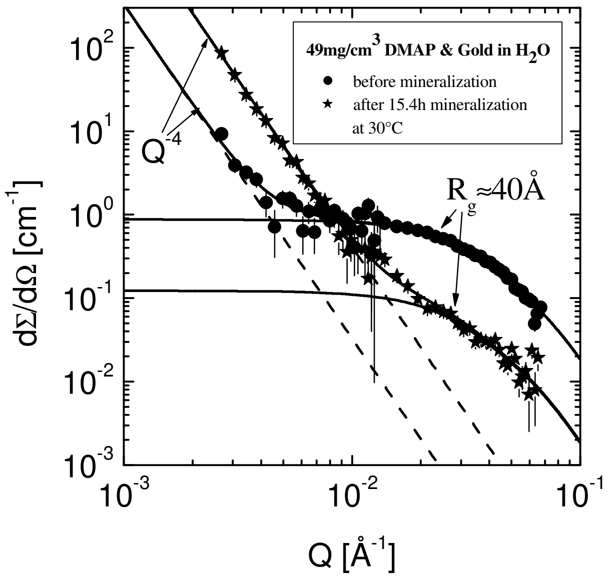

Figure 3.2.3: Before and after 15 h of mineralization at 30℃ in the presence of 49 mg/cm^3 DMAP and colloidal gold.

In Figure 3.2.4 and Figure 3.2.5 the time evolution of characteristic parameters of the large and small particles evaluated from the SANS data are presented. In Figure 3.2.4 the time evolution of the radius of gyration and Porod constant of the smaller and larger particles are shown for two samples; one sample only with DMAP as discussed in Figure 3.2.2, the other one with a low concentration of 5 mg/cm^3 gold plus DMAP. These two samples show at least qualitatively the same mineralization behavior. The smaller particles do not change for the first 2 h and then increase to a R_g of about 350 Å after 6 h. Their growth behavior is slightly different but their incubation time is the same. The same behavior is also found for the Porod constant of the larger particles. No incubation time is visible. The growth velocity is relatively low during the first hour, but then speeds up appreciably and starts to saturate after about 4 h.

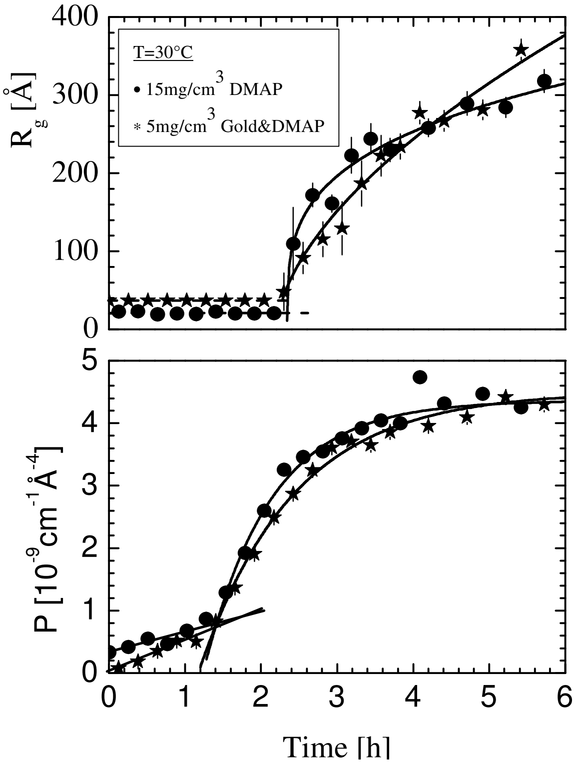

Figure 3.2.4:

Top: Evolution of the radius of gyration of the "smaller" particles by mineralization.

Bottom: Same process for the larger particles as characterized by the Porod constant being proportional to the total surface area.

A quite different result is found in Figure 3.2.5 for the sample with higher DMAP plus gold concentration of 49 mg/cm^3 which has already been discussed in context with Figure 3.2.3. The time evolution of the Porod constant of the larger particles in the lower figure is very similar to that in Figure 3.2.4. A smaller growth velocity during the first hour, then a strong increase, and saturation and slight decrease after six hours. In the discussion of the results presented in Figure 3.2.3 we have mentioned that the size of the smaller particles stays constant within a standard deviation of ±2.3 Å and with a mean R_g=37.2 Å. Actually, at the beginning of mineralization we observe a slightly larger size of 40 Å which then continuously decreases during the first 1.5 h. The upper panel of Figure 3.2.5 shows the evolution of the product of the particle number density and the square of the difference of the coherent scattering length density $\Delta\rho^2$ of particle and solvent. As the coherent scattering length density of gold and $CaCO_3$ is about the same with $\rho \approx 4.5\ 10^{10}cm^{-2}$ one evaluates a $\Delta\rho^2=2.6\ 10^{21}cm^{-4}$ considering the corresponding value for water $\rho=-0.56\ 10^{10}cm^{-2}$. The number density stays relatively constant during the first 4 hours and then strongly decreases reducing the number after eight hours by more than a factor of 5. After eight hours only a slight decrease is observed. Comparing number density and Porod constant in the upper and lower panels of Figure 3.2.5, a correlation between both processes is clearly visible. Along with the strong decrease of the amount of smaller particles the Porod constant is increasing. Saturation of the Porod constant is achieved when about 80% of the smaller particles are used up after eight hours mineralization time and only a small further decrease with time is observed. This clearly indicates that the smaller particles aggregate into the larger ones and thus drive their coarsening.

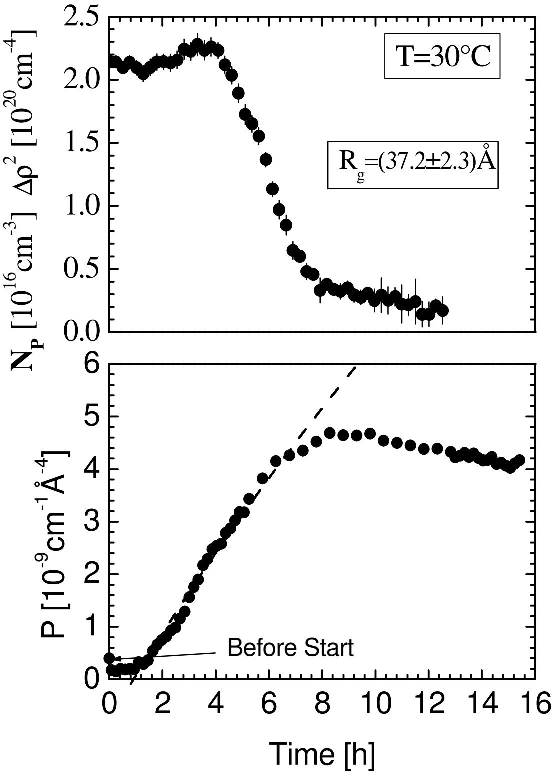

Figure 3.2.5:

Top: Particle number density times the scattering contrast versus time in a solution of 49 mg/cm^3 gold plus DMAP at 30°C (same as in Figure 3.2.3). During this process a constant size of the smaller particles of R_g=37 Å is observed. Between 4 and 8 hours a strong decrease of the number density is observed.

Bottom: Porod constant of the larger particles versus time. Saturation and decrease of P due to coarsening occur after 8 h when the strong decrease of the smaller particles stops. This result is an indication that the smaller particles aggregate into the larger ones.

The observation of two mineralization processes for the smaller particles as a function of the template concentration and temperature is a rather surprising result and not yet understood. To give a better survey we plotted in Figure 3.2.6 a diagram whose axes represent the conditions of mineralization, namely temperature and DMAP plus gold concentration. The positions of the symbols represent the experimental conditions while the symbols •,∗, and ? themselves represent the characteristics of observations, namely, coarsening by the increase of R_g , aggregation as discussed in Figure 3.2.5, and the sample without any gold as discussed in Figure 3.2.4, respectively. The dashed line roughly separates the both regions of coarsening and aggregation.

A possible interpretation of the different coarsening mechanisms might be that (1) the colloidal gold always aggregate into the larger ones while (2) the observed coarsening of the smaller particles at lower temperature and concentration occurs at the smaller DMAP clusters of 20 Å as measured in Figure 3.2.2. These smaller DMAP aggregates might always be present but not visible in the presence of colloidal gold. One could imagine that these smaller DMAP aggregates become unstable above a given temperature and concentration and decompose into discrete molecules which may not be active with respect to the mineralization of $CaCO_3$. The experimental background of this speculation are the results in Figure 3.2.4 showing for the same temperature at 30℃ similar time evolution of the smaller and larger particles.

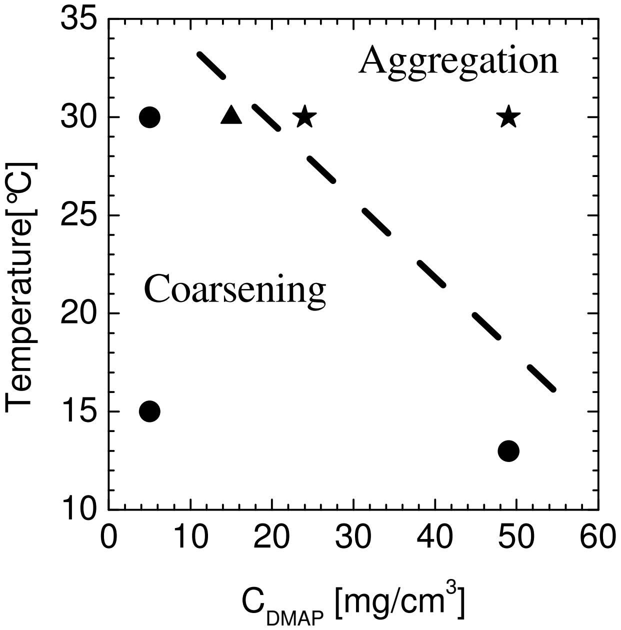

Figure 3.2.6: Diagram showing the external conditions for the two coarsening mechanisms of the "smaller" particles. Separated by the dashed line a coarsening process is observed at low temperature and DMAP concentration. Aggregation as shown in Figure 3.2.5 is found at larger temperatures and DMAP concentration.

3.2.3. Conclusion

In this article we presented first results of the process of $CaCO_3$ mineralization in an aqueous solution in the presence of a template structure build up by DMAP molecules and of 40 Å radius colloidal gold covered with DMAP, thereby offering a large surface. The process of mineralization was performed in a 0.1 M aqueous calcium dichloride solution with the gas diffusion technique using an ammonium carbonate precursor (see equation (3)). In this way, the mineralization was sufficiently slow for the neutron experiments. While $CaCO_3$ in water nucleates into thin (<30 Å) plates and subsequently grows into large porous objects the mineralization in the presence of DMAP molecule templates always leads to 3D compact $CaCO_3$ particles.

The original goal was of course to have a single template structure determined by the surface of the colloidal gold. However, the reality turned out to be more complex showing at least three different template structures of large (>1000 Å) and small (˜ 20 Å) mainly DMAP aggregates and the colloidal gold covered with DMAP. Such a template structure of course leads to a formation of minerals whose original nucleation center is not always easy to survey.

In near future we will focus on studies of the DMAP phase behavior and try to better analyze the concentrations within the different phases by applying the contrast variation technique. In addition, we will fill the diagram of external conditions in Figure 3.2.6 with more data points and try to better understand the two different mechanisms of mineralization.

3.2.4. Experimental

The process of mineralization was initiated and performed in a special stainless steel container with two sapphire windows for the neutrons and which allows a temperature control from - 20 to 100°C. This cell was mounted in the neutron beam allowing in-situ SANS experiments. The experiments usually took about 12 h and were usually performed at two fixed settings of detector-sample distances of 20 m and 4 m with accumulation times of 15 and 30 min for the first 15 and the following measurements, respectively. The so obtained spectra were analyzed in standard procedure by background subtraction of scattering from pure solvent and by absolute calibration with the secondary standard Lupolen. Changes of the transmission were measured for all spectra and could therefore be considered properly.

The process of mineralization of $CaCO_3$ was performed in a cuvette of optical glass containing a 0.1 M aqueous $CaCl_2$ solution. A CO_2 rich atmosphere was produced by thermal decomposition of $(NH_4)_2CO_3$ at ambient temperature. By combining the decomposition reaction of $(NH_4)_2CO_3$ and the reaction between CO_2 and $CaCl_2$ one obtains the $CaCO_3$ mineral according to

$$\left(\mathrm{NH}_4\right)_2\mathrm{CO}_3 + \mathrm{CaCl}_2 \rightarrow \mathrm{CaCO}_3 + 2\left(\mathrm{NH}_4\right)\mathrm{Cl} \tag{3}$$

This gas diffusion technique has the advantage of a sufficiently slow mineralization rate to be detected on the SANS time scale; furthermore, it leads to the same product distribution and morphology as the direct mixing of Ca^{2+} and CO_3^{2-} ions over a reaction time of hours [7].The DMAP ($C_7H_{10}N_2$) molecules attached to the colloidal gold have an appreciable dipole moment and a molecular diameter of about 10Å.

3.2.5. References

[1] S. Mann, *Angew. Chem*. **2000**, *112*, 3532-3548.

[2] H. Endo, H. Cölfen, D. Schwahn, *J. Appl. Cryst.* **2003**, *36*, 568-572.

[3] D.I. Gittins, F. Caruso, *Angew. Chem.* **2001**, *113*, 3089-3092.

[4] G. Beaucage, *J. Appl. Cryst*. **1995**, *28*, 717-728.

[5] R.-J. Roe, *Methods of X-Ray and Neutron Scattering in Polymer Science*. Oxford University Press, Oxford **2000.**

[6] D. Schwahn, M. Balz, W. Tremel **2003**, in preparation.

[7] Endo, H. (private communication).

4. Conclusion

For a better understanding of the process of biomineralization it is indispensable to account for the cooperation of the different types of biological macromolecules involved in the nucleation and growth of biominerals. In the present study a new model system is introduced as an approach to biological systems to study the impact of cooperative interactions between a solid surface and a soluble macromolecule in the presence of Ca^{2+} or Sr^{2+} ions on the template induced crystallization process of inorganic minerals such as calcium carbonate and strontium carbonate. The model system employed for these investigations is composed of a self-assembled monolayer with different functionalities and various dissolved macromolecules.

It was shown that the crystallization of vaterite nanowires can be attributed to the presence of polyacrylate in cooperation with a COOH-terminated self-assembled monolayer (SAM). The amount of adsorbed polyacrylate strongly depends on the functionality of the SAM and is high in the presence of a polar surface (COOH-termination), whereas nearly no adsorption takes place in the presence of a CH_3-terminated SAM. QCM (quartz crystal microbalance) measurements indicated that the adsorption of the polymer onto the COOH-terminated surface is mediated by Ca^{2+} ions. It was demonstrated that the morphologies of the crystalline products exhibit characteristic differences from those that were obtained in crystallization experiments on self-assembled monolayers without the polyelectrolyte.

The same system, i.e. COOH-terminated SAM and polyacrylate, was used for the crystallization of strontium carbonate. The morphology of the obtained crystallization products exhibit a nanowire-like morphology that is nearly the same as obtained for calcium carbonate.

The combination of a COOH-terminated SAM and polyacrylate acts as an interface for the structure-directing crystallization of nanowire-like vaterite and strontianite crystals and therefore represents for the first time an alternative to structure-directing two-phase systems such as micro-emulsions.

It could be demonstrated that the phase selection of calcium carbonate is controlled by the cooperative interaction of a self-assembled monolayer and hyperbranched polyglycerol of different molecular weights adsorbed to the SAM. The studies showed that hyperbranched polyglycerol is adsorbed to polar as well as to nonpolar SAMs. This effect can be related to its highly flexible structure and its amphiphilic character. The adsorption of hyperbranched polyglycerol to the SAMs with different surface polarities resulted in the formation of aragonite for alkyl terminated SAMs and no phase selection for carboxylate terminated SAMs.

It was shown that the functionality of a SAM in the presence of carboxymethyl cellulose has a crucial impact on the phase selection of the crystallization products. Vaterite hemispheres are obtained on a polar surface, whereas calcite crystals form in the presence of a CH_3-terminated surface. Quartz crystal microbalance measurements indicated that the adsorption of the polymer onto the surface is only achieved in case of the polar surface.

To gain a deeper insight into the process of biomineralization one has to elucidate the stadium of primary nucleation. In the present work SANS (small-angle neutron scattering) studies were performed to investigate the process of nucleation in solution without any additives, in the presence of a protein as well as on colloids acting as templates.

The mineralization process of calcium carbonate at very early stages is studied by time-resolved small-angle neutron scattering (SANS). The homogeneous crystallization of $CaCO_3$ in water was found to be a process that involves the initial formation of small thin plates which subsequently reassemble to form 3-dimensional particles first of fractal and finally of compact structure. The studies of nucleation and growth of calcium carbonate in the presence of the egg-white protein ovalbumin lead to a different progression of crystallization. Three stages of mineralization could be identified, the first one representing amorphous $CaCO_3$, while the other two were of crystalline structure. The formation and dissolution of the amorphous phase was accompanied by a Ca^{2+}-mediated unfolding and complexation of about 50 protein molecules. The protein complexes obviously act as nucleation centers for the amorphous phase because of their enrichment by

Ca^{2+}-ions. The second process appears to be a homogeneous nucleation. The amorphous calcium carbonate nanoparticles as well as the crystalline phases were identified by contrast variation technique.

The process of $CaCO_3$ mineralization in an aqueous solution in the presence of a template structure build up by DMAP (4-dimethylamino-pyridine) molecules and colloidal gold covered with DMAP was studied. It was found that the mineralization in the presence of DMAP molecule templates always results in the formation of compact $CaCO_3$ particles. The SANS data indicated that there are present at least three different template structures of large (>1000 Å) and small (˜ 20 Å) mainly DMAP aggregates and the colloidal gold covered with DMAP.

5. Appendix

5.1. Methods and Instrumentation

5.1.1. Quartz Crystal Microbalance [1-5]

A quartz crystal microbalance (QCM) can be described as an ultra-sensitive mass sensor (about 5 ng/cm^2 in liquid). The QCM is composed of a piezoelectric AT-cut quartz crystal sandwiched between two electrodes (Figure 5.1.1). Connecting these electrodes to an AC voltage leads to an oscillation of the quartz crystal at its resonance frequency due to the piezoelectric effect.

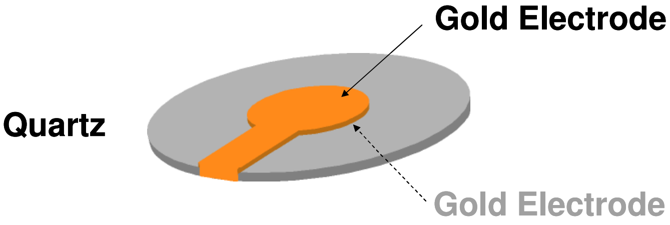

Figure 5.1.1: Illustration of a QCM sensor.

By the adsorption of a material onto the surface, i.e. electrode, the resonant frequency decreases. The frequency shift is proportional to the adsorbed mass if a rigid layer is evenly deposited onto the surface and the so-called Sauerbrey equation can be used to calculate the adsorbed mass:

$?m = -C \times ?f$

with $C = 17.7\ ng \cdot Hz^{-1} \cdot cm^{-2}$ (5 MHz)

$?f$ = measured frequency shift

$?m$ = mass change per unit area

As the application of the Sauerbrey equation is limited to evenly deposited and rigid films it can not be used for films with viscoelastic properties that cause a damping of the resonance frequency.

If the AC voltage is switched off, the oscillation will decay exponentially. In QCM-D (D = dissipation) this decay is recorded and the resonance frequency f and the dissipation factor D are extracted. The faster the oscillation decays the higher the dissipation.

QCM allows to determine the mass of a substance or layer adsorbed to a surface in real-time monitoring. With the QCM-D (D=dissipation) technique it is possible to obtain –additionally to the mass change– information about structural (viscoelastic) properties of the surface bound material by the simultaneous measurement of the damping of the resonance frequency that is caused by non-rigid adsorbed films. This technique delivers the possibility to study interactions of molecules on different types of surfaces or with each other. Furthermore it is possible to get information about the orientation of molecules onto the surface and the structure of the adsorbed film. For example, generally compact globular proteins form rigid films, i. e. the dissipation is low, because the damping of the oscillation of the quartz is small. In contrast, molecules such as DNA-strands bind a lot of water and cause a high damping of the oscillation.

All QCM measurements performed for the studies of this thesis were done on a Q-SENSE D300 system (Q-sense, Sweden), as shown in Figure 5.1.2.

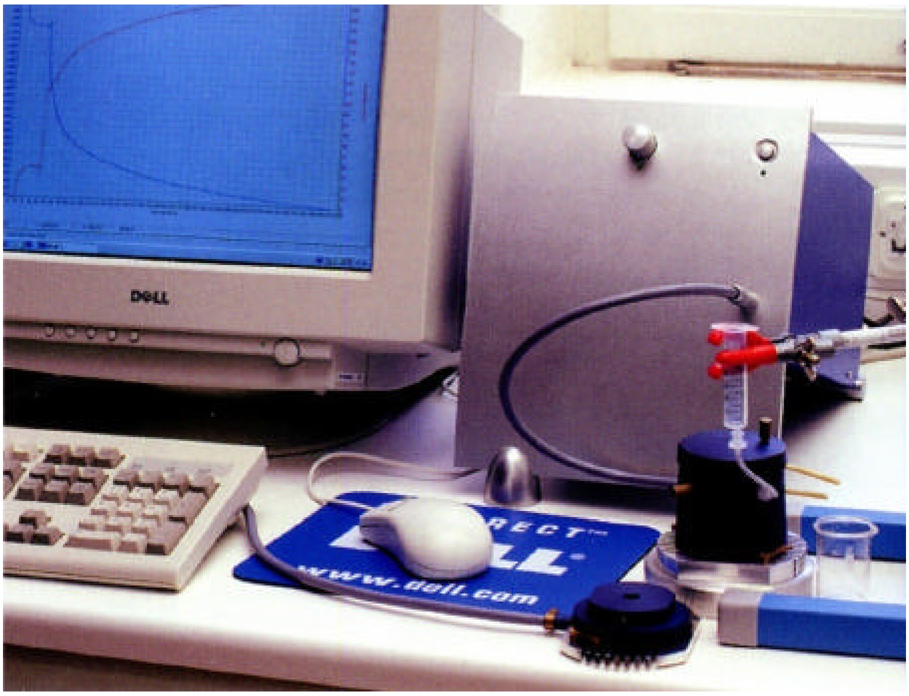

Figure 5.1.2: Q-SENSE D300 system.

5.1.2. Small-Angle Neutron Scattering [6]

The theory of Small-Angle Neutron Scattering (SANS) is described in detail in chapter 3.1.2. of this thesis.

All SANS measurements performed for the chapters 3.1 and 3.2 of this work were performed at the KWS-1 diffractometer (Figure 5.2.1) at the research centre Jülich.

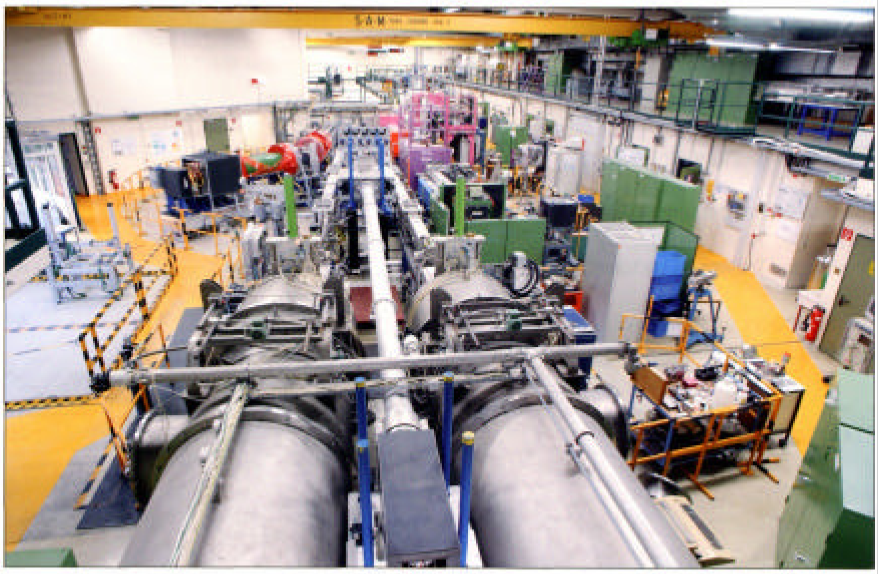

Figure 5.2.1: View on SANS instruments KWS-2, KWS-3 and KWS-1 (from left to right).

The measurement chamber of the KWS-1 instrument is depicted in Figure 5.2.2.

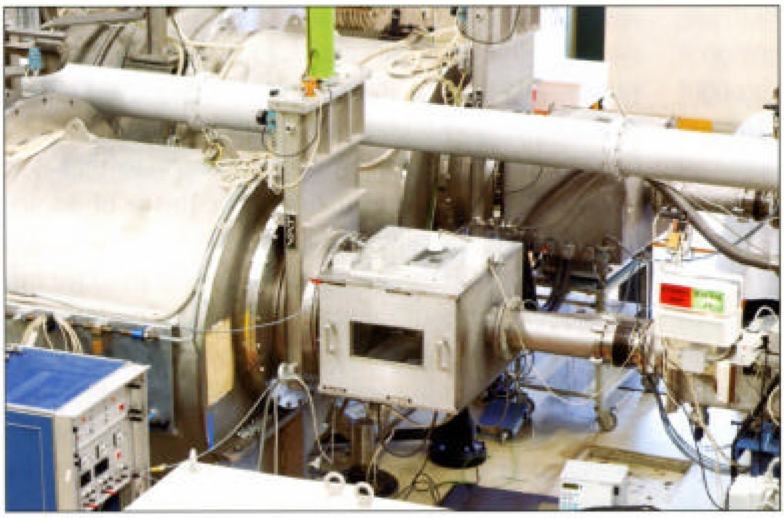

Figure 5.2.2: Measurement chamber of SANS instrument KWS-1.

5.1.3. Surface Plasmon Resonance Spectroscopy [7-11]

The surface plasmon resonance spectroscopy (SPR) is a powerful tool to characterize interfaces and surfaces. The surface plasmons are collective oscillations of free electrons of a metal that propagate along an interface of a thin metallic film and a dielectric. Provided that the resonance condition is fulfilled, the surface plasmons can resonate with light which results in the absorption of light. The resonance condition of the surface plasmons is strongly dependent on the dielectric properties (i.e. refractive index) of the material adjacent to the metal film. This dependency allows to detect the adsorption of molecules onto the metallic film, i.e. changes of the thickness of the layer in the range of Angstrom.

To excite a surface plasmon the incident light has to be coupled with the wave vector of the surface plasmon. For that purpose the Kretschmann configuration is chosen as depicted in Figure 5.3.1.

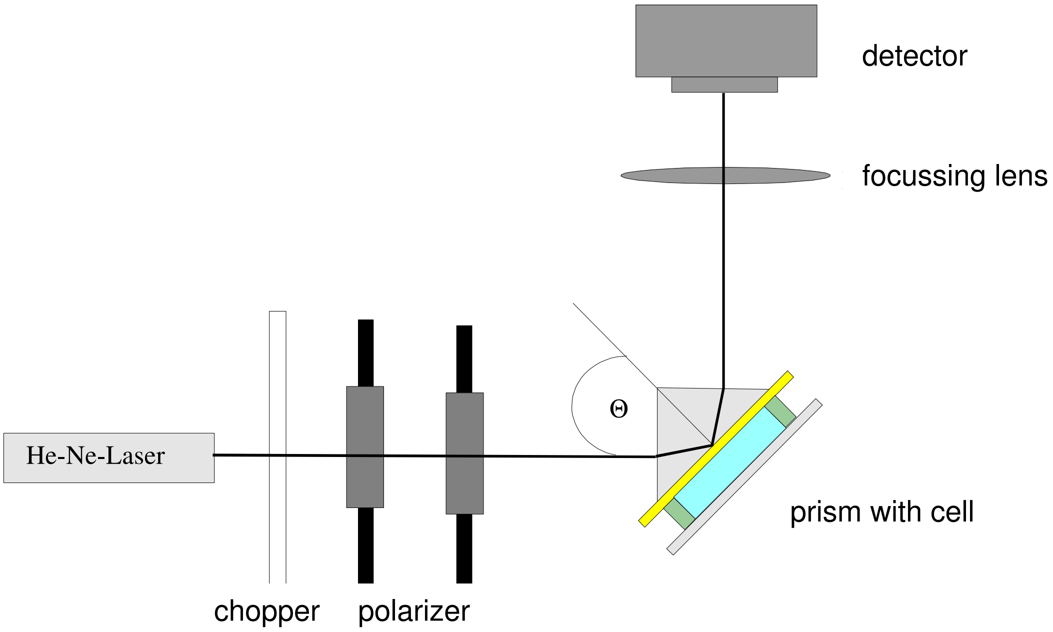

Figure 5.3.1: Kretschmann set-up of a surface plasmon spectrometer.

By changing the angle of incidence of monochromatic light at a certain angle the projection of the light wave vector onto the metal film becomes equal to the wave vector of surface plasmons resulting in an effective transfer of light energy to the surface plasmon. By scanning the angle of incident of the light T, at a certain angle the reflected light intensity converges to nearly zero. This strong decrease indicates that the resonance condition is fulfilled for a fixed frequency.

By applying an additional dielectric layer onto the surface the resonance condition will be shifted to higher values of T. The reflectivity is increased (?R) due to the additional layer. By specific calculations it is possible to determine the thickness of the additional dielectric layer provided that the refractive index of the material is known.

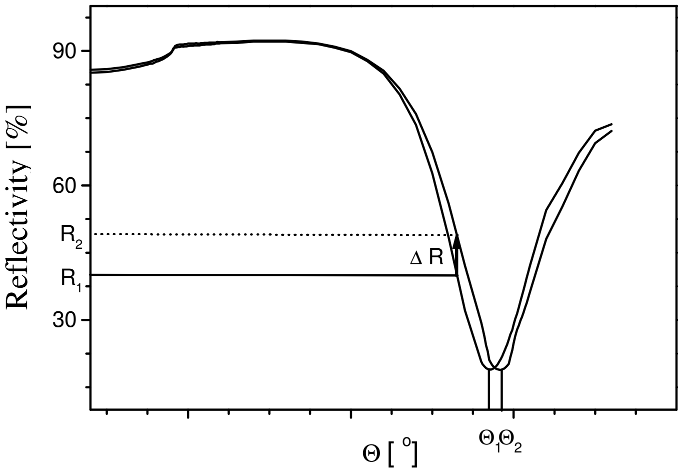

Figure 5.3.2: By applying an additional dielectric layer the resonance minimum is shifted from T_1 to T_2.

[1] www.q-sense.com.

[2] www.lot-oriel.de.

[3] R. Schumacher, *Chemie in unserer Zeit* **1999**, *5*, 268-278.

[4] F. L. Dickert, O. Schuster, *Chem. unserer Zeit* **1994**, *3*, 147-152.

[5] C. K. O`Sullivan, G. G. Guilbault, *Biosensors Bioelectron.* **1999**, 663-670.

[6] www.fz-juelich.de.

[7] A. Janshoff, H.-J. Galla, C. Steinem, *Angew. Chem.* **2000**, *112*, 4164-4195.

[8] H. Raether, *“Surface Plasmons on Smooth and Rough Surfaces and on Gratings“*, Tracts in Modern Physics, Springer Verlag, Berlin, **1988**.

[9] E. Burstein, W. P. Chen, Y. J. Chen, A. Hartstein, *J. Vac. Sci. Technol.*, **1974**, *11*, 1004-1019.

[10] B. Rothenhäusler, C. Duschl, W. Knoll, *Thin Solid Films*, **1988**, *159*, 323-330.

[11] E. Kretschmann, *Z. Physik*, **1971**, *241*, 313-324.